POLITECNICO DI TORINO

Master's Degree
in Mathematical Engineering

Master's Degree Thesis

Mathematical modeling of cellular response to mechanical and geometrical cues on curved substrates

Supervisor
prof. Luigi Preziosi
prof. Chiara Giverso
PhD Giulio Lucci

Candidate
Gabriele Fioretto

Academic Year 2023-2024

Summary

The active response of cells to mechanical cues has been extensively studied over the past two decades. Initially, research focused on the mechanical behavior of cells cultured on flat substrates and subjected to periodic stretching. Several theoretical models were proposed to account for various physical factors influencing cellular response. However, only in the last decade there has been a growing interest in how geometrical cues, such as substrate curvature, affect cell behavior. This increased interest stems from experimental findings highlighting the importance of curvature in cell mechanical response due to the interplay between cellular contractility and substrate geometry. This Master's Thesis investigates the mechanical response of cells on curved substrates using a theoretical framework. It analyzes the effect of substrate curvature on the active reorganization of a cell's internal structure, which is critical for understanding processes such as tissue engineering.

The study begins with a comprehensive biological introduction, outlining the significance of mechanical factors in cellular behavior. Historical context is provided, tracing back to the late 1980s when studies first demonstrated that cells respond to mechanical as well as chemical signals. Numerous experiments have shown that cells reorganize their internal structure when subjected to external periodic deformation, as observed in blood vessels and airways. Academic research has predominantly focused on phenomenological observations of cells on two-dimensional flat substrates. Advances in imaging techniques and measuring tools have enhanced our understanding of how cells respond to mechanical stimuli in these settings. Key findings include the alignment and reorientation of cells in response to cyclic stretching, with reorientation angles depending on factors such as cell type, substrate stiffness, and the amplitude and frequency of applied deformation. Experimental results indicate that cells exhibit markedly different responses on curved surfaces compared to flat ones. Specifically, cells tend to align their stress fibers (SFs) in distinct patterns depending on the substrate curvature. For example, on cylindrical substrates, muscle cells, with long SFs, align with the direction of least curvature, while epithelial cells orient their SFs toward the maximal curvature direction. This counterintuitive result is explained by the interplay between cellular contractility and substrate curvature, causing the SFs to bend.

Firstly, the theoretical setup adopted in this work builds on the mathematical model by Biton and Safran, which explains some experimental results on curved substrates. This model hypothesizes a competition between cellular contractility and the bending of the internal structure due to substrate curvature. Expanding on Biton and Safran's work, a more structured mathematical model is developed to explain the reorientation

process while considering recent findings in cell modeling. The combination of bending and contractility forces creates a complex energy landscape governing cell stability and configuration. Stability analysis, conducted through bifurcation analysis, reveals critical configurations where cells undergo significant morphological changes. These configurations result from the competition between bending energies and contractile forces, leading to stable and unstable equilibrium states. It is shown that the stable configuration depends on a parameter containing both contractility and curvature information. Comparisons with Biton and Safran's results demonstrate that a limiting case of the general model aligns with their findings.

Further, inspired by biological contexts, the Thesis examines cell reorientation on inflated cylindrical substrates, considering both isotropic and anisotropic mechanical responses. This study explores the kinematics of cylinder inflation and the resulting cellular behavior, highlighting how the deformed radius influences cell orientation. It is shown that in a controlled deformation setup, only a few experimental results are accurately predicted by this model, suggesting the need for expansion by considering cellular-level interactions. Hence, in the final sections, the analysis is extended to materials with initial stress, using hyperelastic theory to describe residual stresses in orthotropic materials. The impact of residual stress on cylinder inflation and subsequent cellular reorientation is investigated, providing a more comprehensive understanding of the mechanical environment that cells experience in vivo. This analysis includes a detailed theoretical discussion of the strain energy function and the role of residual stress in modulating cellular responses.

This work combines experimental observations with rigorous mathematical modeling to elucidate the mechanical principles governing cell behavior on curved substrates. The findings have broad implications for biomedical applications, emphasizing the importance of understanding the mechanical environment of cells to design effective therapies and biomaterials.

In detail, the thesis is organized as follows.

Chapter 1 provides an overview of how cell behavior is influenced by mechanical factors and geometrical cues, in addition to chemical signals. It starts with historical studies that demonstrated cell alignment along stretched substrates. The Chapter discusses the role of the cytoskeleton, particularly actin stress fibers (SFs), in cellular responses to mechanical stimuli. It also highlights the importance of geometrical cues such as curvature, which significantly affect cellular behavior. Experimental findings on cellular reorientation on curved substrates are reviewed, demonstrating the role of active contractility and the delicate balance between SF bending and contractility in cellular organization.

Chapter 2 delves into the mechanical modeling of cells on curved substrates, particularly focusing on the linear theory of elastic plates bent over a cylinder. It covers kinematic assumptions, the linear solution of a plate bending over a cylinder, and the stored elastic energy after bending. The Chapter explores the contribution of active contractility to cell behavior and the stability of different cellular configurations on curved surfaces. Bifurcation analysis is used to understand critical configurations and their stability, considering the competition between bending and active contractility.

Chapter 3 focuses on how cells reorient in response to the inflation of cylindrical substrates. The Chapter begins by defining the kinematics of cylinder inflation. Then, an overview of the main theoretical models is presented, with particular attention to the

impact of the chosen strain energy function. Finally, the Chapter investigates the mechanical response of a material with orthogonal families of fibers within the cylindrical structure, in accordance with the mathematical models for cell reorientation available in the literature. Particular attention is paid to the remodeling in response to controlled inflation, aiming to identify optimal configurations that minimize system energy states.

Chapter 4 examines how pre-existing residual stresses in materials affect cellular reorientation. It begins with the hyperelastic theory of residual stress, covering preliminary considerations and the strain energy function for residually stressed orthotropic materials. The Chapter then discusses residual stress effects in cylinder inflation, including bifurcation analysis and the impact of curvature and active contractility due to prestrain. It also explores different scenarios, such as specific cases where residual stress configurations significantly influence cellular behavior.

Chapter 5 concludes the Thesis by summarizing the key findings from the previous Chapters. It discusses the broader implications of these findings for biomedical applications, such as tissue engineering and the design of biomaterials. The chapter also suggests directions for future research, emphasizing the importance of understanding the mechanical environment of cells to develop effective therapies and innovative biomaterials.

Contents

Chapter 1

Biological introduction

During the late 1980s, groundbreaking studies in cardiovascular pathophysiology demonstrated for the first time that cell behavior is influenced not only by chemical signals but also by mechanical factors. Buck was the first to observe this phenomenon, prompted by the alignment of cells along the aortic wall [3]. He then performed an experiment where cells were planted on a cyclically stretched substrate [4], noting that almost all cells aligned themselves at roughly 45/90 degrees relative to the primary direction of stretch. Captivated by these observations, various researchers explored the reactions of different cell types to cyclic stretching [5–7]. Most of these investigations indicated an orientation angle, implying an active cellular response to the applied stretch. The sole study to report contrary findings was by Matsumoto et al. [8], who experimented with macrophages. This indicated that the cytoskeleton plays a crucial role in cell behavior. In particular, the cytoskeleton includes a network of filaments, with actin stress fibers (SFs) being crucial for contractility. These fibers are composed of actin filament bundles that are interconnected by myosin or other proteins, arranged either parallel or at certain angles, as shown in Figure 1.1.

At the ends of SFs, a complex called focal adhesion (FAs) connects the cytoskeleton to the external environment, enabling cells to detect changes, such as mechanical or chemical ones, and react accordingly. Indeed, SF reorientation is strongly associated with cell reorientation. This relationship was demonstrated by White et al. [10] and Wong et al. [11], who studied the correlation between periodic stretches and cytoskeletal deformation.

Furthermore, cellular behavior under in vivo conditions is significantly influenced by geometrical cues, such as curvature, which are ubiquitous throughout the human body. Indeed, the response of cells to curved substrates has attracted a significant amount of interest in the past decade. Several studies [12–14] have investigated cell reorientation when cultivated on curved, often cylindrical, substrates. These investigations have demonstrated that cytoskeletal reorientation varies widely depending on the curvature of the substrate. Experimental findings have revealed that long stress fibers (SFs) align themselves with the direction of lesser curvature (in the case of a cylinder, the direction of the generator), while short, thick basal SFs align with the maximal curvature direction, which is a counterintuitive result. Indeed, these studies have substantiated how active contractility plays a pivotal role in the reorientation of SFs, as suggested by Biton and

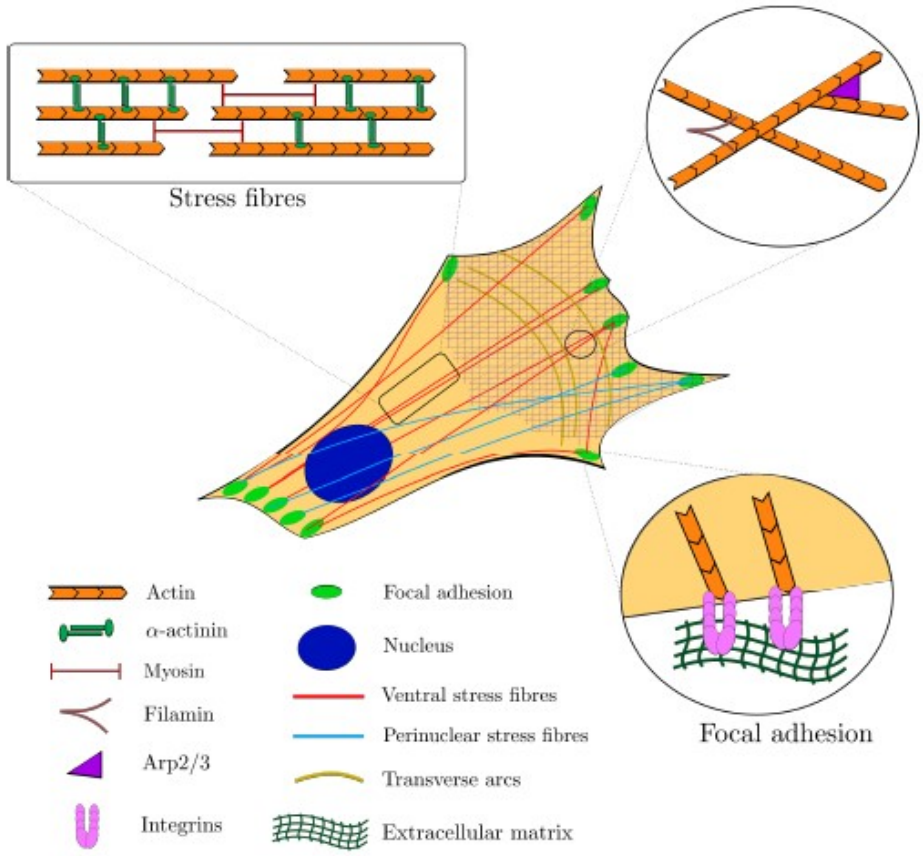

Figure 1.1. Sketch of the inner structure of a typical cell and of its adhesion to the substrate [9]

Safran [15]. According to this hypothesis, the organization of the cytoskeletal cells subject to curvature is determined by a delicate balance between the active contractility exerted by the SFs and the bending of the SFs. However, recent work [16] has demonstrated that within the same cell, the behavior of SFs splits into two subpopulations, suggesting a more nuanced understanding is required.

The subsequent sections of this study focus on cellular responses to mechanical cues on flat substrates and under curvature. Section 1 outlines the main findings regarding cellular reorientation under stretch on planar substrates. In contrast, Section 2 investigates the impact of curvature on cell behavior, focusing primarily on cytoskeletal organization. Section 3 briefly explains the statistical methods used to compute the experimental results.

1.1 Phenomenological Observation of Cells on Two-Dimensional Flat Substrates

Numerous attempts have been made to elucidate the mechanisms underlying cell alignment and reorientation. Advances in technology, including imaging techniques and sophisticated measuring tools, have provided a more precise understanding of cellular responses to mechanical stimuli. These advances have revealed additional features of cellular behavior in response to mechanical cues. The following summarizes the main aspects achieved over the years, with a more detailed review available in Giverso et al. [9].

Typically, two-dimensional settings are adopted to investigate cell behavior under stretch. These settings often involve a silicone and/or polydimethylsiloxane (PDMS) substrate [5–7], coated with collagen or other substances to promote cell attachment. Cells are then seeded onto the substrate and, upon attachment, the substrate is stretched along one or two perpendicular directions. In most experiments, a unidirectional cyclic stretch is applied, as it mimics many in vivo biological situations.

An important quantity introduced in the literature, both from experimental and mathematical perspectives, is the *biaxiality ratio*:

$$r = -\frac{\max_{t\in\mathscr{T}} \epsilon_{yy}(t)}{\max_{t\in\mathscr{T}} \epsilon_{xx}(t)},$$

where ϵ_{xx} is the strain in the main stretching direction, and ϵ_{yy} is the strain in the perpendicular direction. If the deformation is uniaxial without constraints on the edges, then r corresponds to the Poisson ratio of the elastic material that makes up the substrate. However, uniaxial settings do not provide complete control over deformation along the vertical axis. Therefore, biaxial tests, which control both vertical and horizontal strains, are adopted for broader and more controlled experiments.

As mentioned above, most experiments focus on periodic deformation applied to the substrate to simulate biomechanical stimuli. Sinusoidal [17], triangular, or trapezoidal waveforms are commonly used to describe the strain. Generally, the mechanical properties of the substrate dictate the response to such a periodic deformation. Subcellular contact guidance introduced by anisotropic substrates, such as microgrooved surfaces, introduces a mechanical cue that alters reorientation behavior, as demonstrated by Tamiello et al. [18].

The cell cytoskeleton plays a fundamental role in sensing external stimuli and reorganizing its structure. One of the first works to highlight the relevance of the cytoskeleton in the realignment process is by Hayakawa et al. [19], who studied the relationship between cytoskeletal rearrangement and cytoplasm reorientation. They showed a significant time difference between the reorientation of stress fibers (SFs) and the reorientation of the cell body. Subsequent experiments focused on the role of SF subtypes. Roshanzadeh et al. [20] demonstrated that the cytoplasm, whose reorientation is driven by peripheral SFs, oriented at 76°, while the nucleus, guided by the perinuclear cap fibers, exhibited different dynamics.

However, immune cells do not appear to respond to the stretch-avoidance mechanism, as shown by Matsumoto et al. [8]. This behavior is likely due to the lack of a robust cytoskeleton in immune cells, preventing them from generating sufficient traction force

necessary for cell reorientation.

Some experiments have been conducted with a frequency set to $1Hz$ [21], corresponding to the physiological value of a normal heartbeat. Jungbauer et al. conducted one of the most detailed studies concerning the effects of amplitude and frequency [22]. They found that a cell type-dependent *minimal threshold frequency* is required to induce significant cellular reorientation. Moreover, there exists an *upper threshold frequency* beyond which the reorientation time saturates. This cell-type-dependent frequency threshold is crucial and is supported by several experimental reports. There is a similar dependence with respect to amplitude, where a minimum amplitude threshold is necessary to trigger reorientation, while an upper threshold is naturally imposed to prevent cell damage [17]. Mathematically, this behavior cannot be described by an elastic medium alone. The dependence on frequency and waveform selection affects cell behavior, necessitating the introduction of characteristic times or viscous dynamic processes, as demonstrated in [23].

Lastly, the dependence of this process on the stiffness of the substrate is worth analyzing. In most experiments, the elastic modulus of the substrate material is close to $1MPa$, making them quite stiff and nearly impossible to deform by cellular traction forces. However, some experiments have highlighted the effect of soft substrates on cell reorientation. It is suggested that, due to the low substrate stiffness, externally applied strain is not fully transferred to the cells attached to its surface. Faust et al. [24] demonstrated that cells seeded on very soft substrates ($1-3kPa$) did not show a statistically significant response to periodic stretching. Other studies, such as [25], showed that cells tend to orient parallel to the principal stretching direction on softer, thick collagen gels.

1.2 The Influence of Curvature on Cellular Behavior

The intricate morphologies observed in biological systems, such as the undulating contours of leaf surfaces or the convoluted arrangements of circulatory networks, frequently manifest as curved geometries. This phenomenon incites inquiries into the mechanobiological significance of curvature. Recent advancements in imaging and analytical methodologies have illuminated these effects across diverse scales, ranging from molecular interactions at lipid membranes to the developmental processes shaping epithelial tissues and the emergence of cortical features on mammalian brain surfaces.

Nevertheless, elucidating the singular influence of curvature on cellular behavior poses a formidable challenge, primarily due to the technical limitations associated with in vivo three-dimensional imaging within living organisms. To avoid this constraint, experiments are conducted within controlled artificial environments, facilitating the manipulation of curvature parameters in isolation. Figure 1.2 visually encapsulates some of the effects observed across varying magnitudes of scale.

For instance, the deliberate imposition of controlled curvature on cellular and tissue substrates has yielded insights into the underlying mechanisms governing curvature-dependent guidance and sensory responses. For a comprehensive examination of these phenomena, the interested reader is directed to recent reviews [26, 27]. While the exploration of curvature effects across various scales presents an intriguing material of study, our focus herein centers specifically on experiments and discoveries about the reorganization

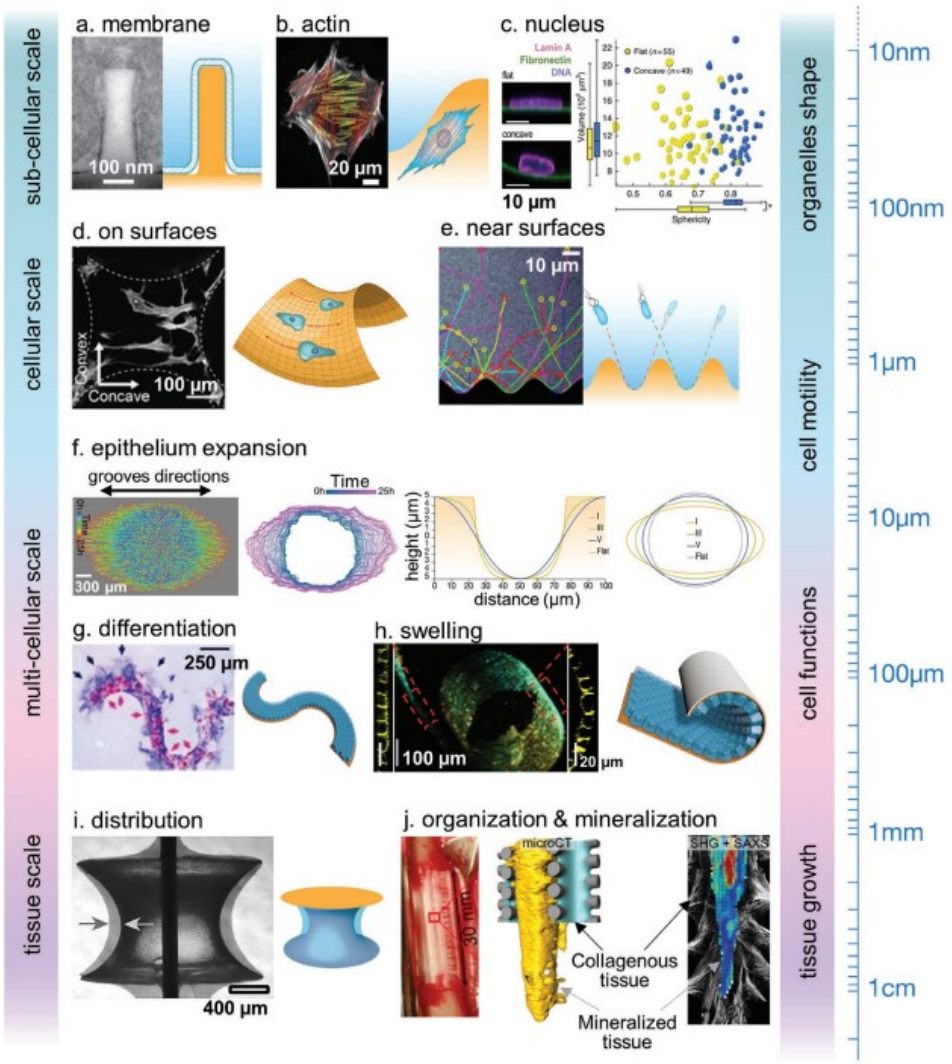

Figure 1.2. Illustration depicting curvature effects across scales [26]

of the cytoskeletal's stucture in cells in reaction to curved substrates.

1.2.1 Experimental Results

Although geometrical cues, such as nano- and microtopographical features of substrates, are well-documented to influence cytoskeletal organization, much remains unknown about how larger geometrical cues, on the order of the cell scale, impact cellular behaviors. Nevertheless, significant efforts have been made in the last decade to shed light on this subject. Below, we present a detailed overview of key experiments and findings. To capture curvature effects, these experiments are carried out on artificially built substrates

with controlled curvature, such as cylindrical channels of convex and concave curvature [13, 14, 28], or wires [12, 16] with varying radii.

A study by Nathan D. Bade et al. [16] focused on the impact of macroscale curvature on the cytoskeletal organization of various cell types. Specifically, the researchers examined the responses of human vascular smooth muscle cells (hVSMCs) and mouse embryonic fibroblasts (MEFs) cultured on wires of varying radii.

For wires with large radii, no discernible preferential configuration was evident for either cell type. However, as the radii decreased, a striking axial alignment emerged. In particular, around a critical radius ($R_c = 40\mu m$), isolated hVSMCs exhibited a weaker alignment compared to MEFs (see Figure 1.3), possibly attributable to lower levels of F-actin in the former. Consequently, hVSMCs might incur a lower energy penalty for orienting in alternate directions.

Furthermore, employing novel imaging techniques, the study unveiled two different subpopulations of stress fibers (SFs), apical and basal, each exhibiting distinct alignment patterns directly influenced by curvature. Both cell types demonstrated a tendency for basal SFs to align circumferentially, particularly pronounced in smaller cylinders where basal SFs approached orthogonality to the apical ones. Further investigation revealed an increase in the average angle between basal and apical SFs with cylinder curvature.

Interestingly, activation of the Rho protein in both MEFs and hVSMC resulted in the formation of thicker, densely packed stress fibers predominantly aligned in the circumferential direction for $R_c = 125\mu m$, mimicking the patterns observed in vivo vessels. The thickness of SFs typically correlates with the measure of contractile strength, suggesting that the activation of the Rho protein may induce a transition from a bending-dominant regime to a contractility-dominant one. This transition underscores the dynamic interaction between biochemical signaling and mechanical cues in cellular responses to curvature.

However, the reorientation behavior is cell-type dependent. Indeed, Hannah G. et al. [12] cultured a monolayer of epithelial cells on artificially manufactured wires, which were subsequently fixed and imaged after 48 hours of growth. Alongside uncovering intriguing migratory behaviors on these wires, we focus only on the alterations in cytoskeletal organization in response to variations in the wire's radius (R).

Specifically, the researchers observed that cells exhibited a random orientation of fibers on relatively large radii, whereas actin fibers became highly oriented perpendicular to the longitudinal axis of the wire at radii below approximately $40\mu m$, even in cases where a single cell wrapped around the wire. This behavior is starkly in contrast to observations of fibroblast cells, which tend to align with the direction of the wires. Additionally, an increase in focal adhesion (FA) density was observed, with multiple FAs found along a single fiber, in contrast to the typically flat distribution, where only two FAs are present at the extremities. These studies underscore the significance of curvature effects even at the cellular level, while also affirming a cell-type-dependent response.

Moreover, it is essential to understand how the sign of curvature, i.e., the convexity or concavity, of the substratum impacts the behavior of cells. A recent study by Yang Jin et al. [28] focused on analyzing the effects of curvature on airway smooth muscle cells (ASMCs). These effects are particularly noteworthy because these cells wrap around tissues with significant curvature in vivo. The researchers cultured cells on a 3D-printed substrate featuring cylindrical channels, both concave and convex.

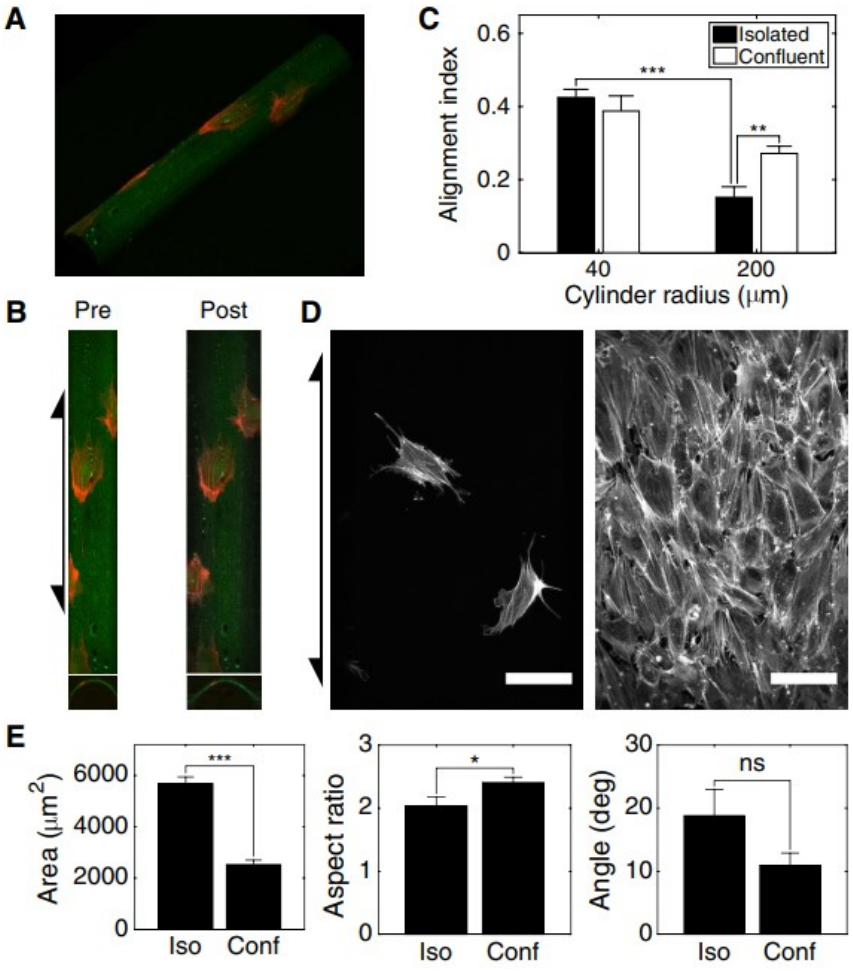

Figure 1.3. Mouse embryonic fibroblasts (MEFs) cultured on a cylinder with a radius of $R_c = 40\mu m$. The comparison is drawn between an isolated cell and a confluent monolayer. [16]

It is important to note that the computed angles are considered biased because they are compared with results from a flat substrate. For a radius of $R = 100\mu m$, the experiments revealed a perpendicular alignment of ASMCs on concave surfaces, with a biased angle of 95°, while the angle was close to 30° for convex surfaces, as illustrated in Figure 1.4. Decreasing the radius, thus increasing the curvature of the surface from $100\mu m$ to $50\mu m$, resulted in an increase from 95° to 115° for concave surfaces, and a decrease from 30° to 15° for convex surfaces. This trend aligns with the hypothesis that muscle cells tend to reorient towards the cylinder axis for higher curvature values.

As depicted in Figure 1.4 (B, D), the orientation of stress fibers forms a helical structure in a three-dimensional space, mirroring observations in vivo. Additionally, Figure 1.4 (C) illustrates that for concave surfaces, SFs are suspended between two anchor points, whereas

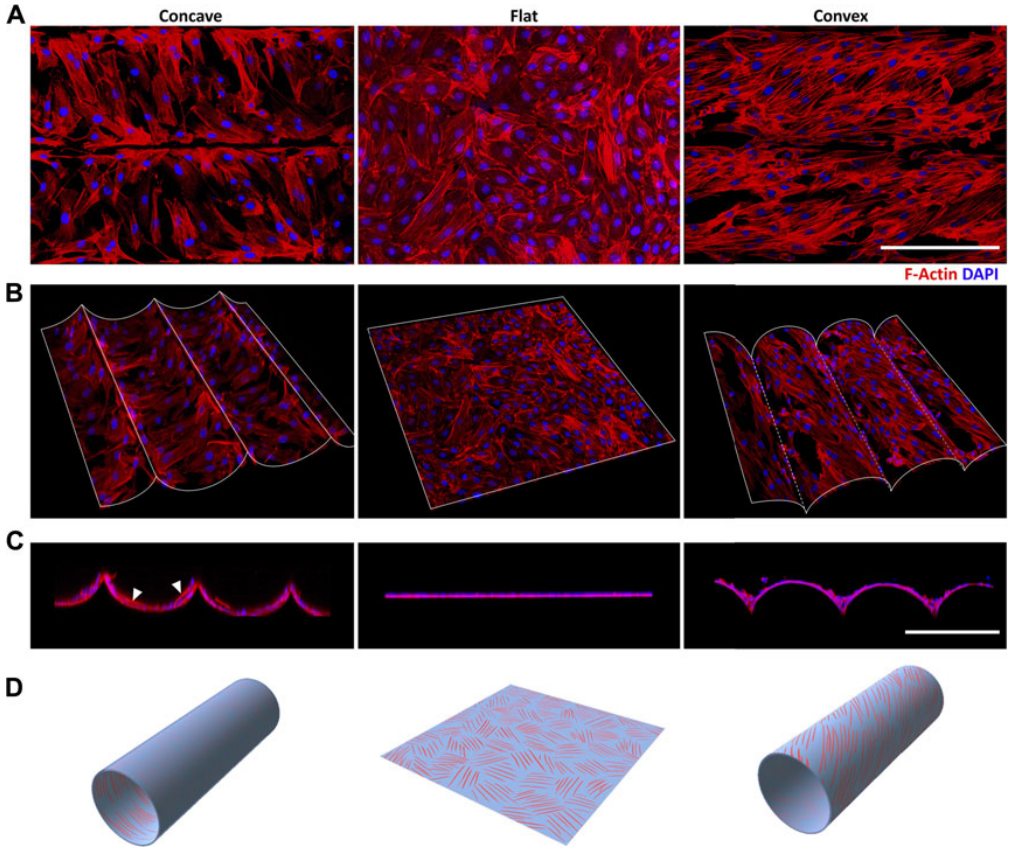

Figure 1.4. Curvature induced stress fibers (SFs) helical arrangement of ASMCs [28]

they are closely attached to the substrate for convex surfaces. The behavior exhibited on concave surfaces was also observed for different surfaces when the substrate exhibited concave curvature [29].

Finally, the researchers analyzed the differences in gene expression of ASMCs between flat and curved substrates. The results revealed that cells on concave surfaces exhibited lower levels of the contractile phenotype α-SMA and displayed a diffusion-like state on convex surfaces, while the proliferation phenotype was higher. These findings underscore the significant role of substrate curvature in regulating gene expression in cells.

Another study [13] explored experiments involving human tubular cells (HK-2) and canine distal tubule cells (MDCK), representing two types of renal epithelial cells. The investigation focused on a curved stiff substrate with both convex and concave curvature, mimicking canal shapes within a multiparametric analysis. The range of analysis radii extended from $R = 44\mu m$, akin to in vivo human proximal tubules, to $R = 908\mu m$.

Consistent with previous findings, on substrates with larger curvatures, stress fiber alignment was observed perpendicular to the axis of the channel. In contrast, on concave substrates, the F-actin structure was oriented parallel to that direction, suggesting that

the sign of curvature also influences the reorientation phenomenon in epithelium-type cells. In particular, both types of cells exhibited a similar alignment tendency, albeit with minor differences in magnitude. Interestingly, neither HK-2 nor MDCK cells demonstrated a significant alignment difference between the basal and apical subpopulations.

Furthermore, the relationship with the myosin contractility intensity of the fibers was investigated. Specifically, MDCK cells were treated with a Rho kinase inhibitor, reducing cell stiffness, leading to a greater orientation towards the perpendicular direction. This finding adds another dimension to the importance of myosin-activated cell contractility factors in the reorientation process.

Regarding the differences in cell families, these experiments showed that for both concave or convex curvature, muscle-type cells and epithelium-type cells exhibit an opposite response to curvature: while the former align along the axis of the cylinder when exposed to convex curvature and perpendicular to it for concave ones, the latter spontaneously orient toward the transverse one for convex curvature and longitudinally when exposed to concave. Nevertheless, although [16] showed the existence of two subpopulations of SFs, the apical and the basal, with different behavior for both hVSMC and MEF, Yu and his collaborators [13] proved that MDCK and HK-2 do not exhibit such behavior.

A notable study is the one conducted by Rougerie et al. [14] that involved MDCK cells. Unlike previous experiments, this study explored a broader range of curvature, ranging from a maximum curvature radius of $R = 44.4\mu m$ to a minimum radius of $R = 2\mu m$. Further validation of previous findings was achieved, with a specific focus on understanding how curvature influences epithelial growth and elongation. The researchers experimented with five distinct substrates featuring varying degrees of grooves and ridges, each characterized by a progressive smoothing of the junctions between the ridges and grooves.

The findings of this study highlighted the significant impact of the most convex regions on the distribution of stress fibers. Specifically, upon imaging of the SFs in proximity to the regions adjacent to the most convex points, the researchers observed the presence of thick F-actin bundles aligned parallel to the axis of the groove without intersecting the convexity. Notably, despite the typical orientation of SFs towards the direction of maximum curvature expected in epithelial cells like MDCK, the cells exhibited a longitudinal reorientation response when subjected to extreme curvature values. Moreover, they proved a linear relationship between the cells monolayer and the maximum curvature of the topography.

As a final cue, another paper by Werner et al. [30] carried out a study investigating the impact of cell-scale curvature and nanogeometric cues on the migratory behavior of human bone marrow stromal cells (hBMSCs). They revealed the presence of a transition point where meso-scale curvature supersedes nano-scale contact guidance. Interestingly, for this cell type, the transition point was pinpointed at a cylinder diameter of approximately $1000\mu m$, which exceeds the size of hBMSCs approximately tenfold. In particular, previous experiments used radii smaller than this critical value. While this behavior is unquestionably contingent on cell type, it is conceivable that prior experiments were unaffected by nanoscale substrate imperfections, thus underscoring the pivotal role of curvature alone.

These experiments provide valuable insight into the cellular response to curvature. Besides the clear cell-type dependency seen in most experiments, even within the same cell-type family, the existence of two different SFs subpopulations with differing behavior is

highlighted. This behavior alone supports the hypothesis of Biton and Safran [15], where the cell cytoskeletal orientation is determined by a competition between the contractility of the stress fibers and their bending. Moreover, this hypothesis is also supported by the experiments of enhancing or inhibiting Rho protein [13, 16], confirming the relationship between curvature and the myosin-activated contractility of the cells. Finally, it seems that curvature also affects gene expression of cells and the contribution of contact guidance in cellular development.

These collective findings underscore the intricate interplay between curvature and cellular responses, revealing nuanced mechanisms underlying cytoskeletal organization and gene expression modulation in various cell types.

1.3 Statistical Description of the Results

In most experiments, the orientation angle θ plays a crucial role, necessitating a brief discussion of the main techniques employed to compute these angles. For experiments involving cell alignment under stretch, a common approach is to measure the angle θ between the stress fibers of the cell and the primary stretching direction. However, it has been demonstrated that cell reorientation exhibits symmetries regarding angle alignments. Specifically, there is no inherent preference for a configuration with an angle θ over a configuration with an angle $\pi - \theta$. Furthermore, the context of reorientation remains unaffected by cell polarity, implying that angles θ and $\pi + \theta$, as well as $-\theta$ and $\pi - \theta$, represent equivalent configurations.

Similar considerations apply to cells subjected to curvature. In the case of experiments conducted in artificially constructed environments, where one direction typically exhibits zero curvature, this direction is often referred to as the axial direction because of the prevalent wire or cylindrical channel shapes. Consequently, the angle of reorientation θ is related to the angle between the stress fibers and the axial direction.

Data are typically presented using a histogram depicting the distribution of angles within the interval $[0, \frac{\pi}{2}]$, or by directly computing the average angle $\bar{\theta}$ over that interval. In particular, when cells are analyzed on curved substrates, the cell cytoskeleton is examined slice by slice along the cell thickness, forming a stack of layers. Consequently, the mean orientation angle θ is calculated by initially averaging the orientation within a stack of a single cell, followed by calculating the mean throughout the population [14, 28]. These imaging techniques also facilitate the study of different behaviors exhibited by SFs subpopulations, as highlighted previously [16].

However, due to potential limitations associated with the mean reorientation angle, alternative parameters have been employed. One such parameter, commonly used for both flat and curved substrates [12, 13], is the *order parameter* defined as:

$$S := \int_0^\pi g(\theta)\cos(2\theta)d\theta = \langle \cos(2\theta) \rangle$$

Here, $g(\theta)$ represents the empirical distribution function of cell angles. Consequently, a random orientation corresponds to $S = 0$, a fully parallel orientation to $S = 1$, and a perpendicular orientation to $S = -1$. However, it is important to note that this parameter

does not precisely quantify the orientation angle unless it corresponds to either a parallel or perpendicular orientation.

Chapter 2

Cell over curved substrata

Numerous studies have demonstrated that cells can detect and react to both mechanical and chemical signals. A variety of mathematical frameworks have been developed to explain the reorganization of the cell's cytoskeleton, from models focusing on strain avoidance to those emphasizing minimal energy configurations [9]. Yet, there have been limited efforts to simulate how cells respond to mechanical stimuli related to curvature.

An early theoretical approach to model the reorientation in cylindrical bending was proposed by YY Biton and S A Safran [15]. Specifically, they posited that the reorientation angle θ, which is the angle between the stress fibers and the cylinder's axis, is influenced by a balance between the shear stress due to the active contractility of the fibers and their own bending. This theory effectively accounts for the differing behaviors observed in elongated cells, such as fibroblasts, compared to discoid cells like epithelial cells.

Another model was introduced by Sanz-Herrera et al. [31]. This model, based on a multiscale analysis of the stress fibers, assumes that curvature diminishes cell contractility and also induces a pre-deformed state. Although the former assumption is supported by experimental evidence [26], the model's predictions do not align with experimental results. Contrary to the model's predictions, cell behavior on flat surfaces should differ from that on cylindrical substrates, contradicting experimental observations.

Despite its restrictive assumptions, the model by Biton and Safran is highly regarded within the scientific community, particularly for its hypothesis that cell cytoskeletal behavior involves a compromise. This Chapter will analyze these results within a more structured context than that presented in the original article.

The Chapter is structured as follows. Section 1 introduces the theoretical framework for the bending of a transversely isotropic plate bent over a cylinder. Section 2 discusses the active contractility effects due to myosin-activated SFs. Section 3 analyzes the optimal configurations and the bifurcation diagram, starting from the elastic energy stored after the superposition of bending and contractility effects. Conclusions are then drawn.

2.1 Linear theory of elastic plates: bending over a cylinder

In an article by Biton and Safran, the authors presume that a cell can be approximated as a thin plate, with the thickness h being significantly smaller than the other dimensions L. Although this hypothesis might seem excessive, it has been validated by numerous experiments, which show that cells exhibit a relatively small h after adhering to a substrate.

2.1.1 Kinematic assumptions

To derive the governing equations of a plate, one can use an expansion of the leading order equations with respect to a small parameter $\epsilon = \frac{h}{L} \ll 1$ and then take the leading order. This approach is supported by extensive literature on asymptotic methods and Gamma convergence theory [32].

Our goal here is to employ plate theory to explain some of the observed cell behavior in experiments. To achieve this, we utilize a linear plate theory that provides analytically tractable results and can still capture the main features observed in cells [33]. By "linear," we mean that strains and displacements are considered to be small quantities. Additionally, we employ a linear constitutive equation to describe the material's elastic response, which is characterized by a Hookean response function.

The assumptions underlying our analysis are as follows:

- The thickness h is much smaller than the other dimensions of the plate L.
- The strains $\frac{\partial u_i}{\partial x_j} \ll 1$, and thus a good approximation of the strain tensor is $e_{ij} = \frac{1}{2}(\frac{\partial u_i}{\partial x_j} + \frac{\partial u_j}{\partial x_i})$.
- The displacements are small, and the vertical displacement ξ is much smaller than the thickness h.
- The material is described by a Hooke constitutive equation.

Let the plate be described in the form $\Omega = S^n \times [0, h]$, where S^n is a closed subset of $\mathbb{R}^2$, hence we are assuming that the reference configuration is flat. Let the coordinate $z \in [0, h]$ be the *transverse coordinate*.

The theory of plates dictates that the strain and stress fields are determined by the displacements of a particular cross section of the plate. To elucidate this concept, let's consider an isotropic plate that undergoes bending deformation. One portion of the plate experiences compression, while the other portion experiences stretching. On the convex side, the points undergo extension, which decreases as we move through the plate's thickness, becomes zero, and then experiences compression. Consequently, there exists a surface, referred to as the *neutral surface*, that is free of both compression and stretching - which is why we defined the domain as S^n. This surface clearly lies in the middle of the plate. The governing equations of the system depend on the unknowns, such as the vertical displacement of the neutral surface (known as "transverse displacement") and the in-plane displacement of the surface, which are completely decoupled from each other.

However, this is a relatively straightforward scenario. In more complex cases involving higher order theories and anisotropic materials, the neutral surface may not be present, while still accurately describing the fields based on the plate's displacements. Specifically, while the in-plane displacements were previously decoupled from the transverse ones, this is no longer the case. These quantities are now coupled within the governing equations of the body. Nonetheless, we will assume that the material anisotropy is symmetric respects the neutral surface, meaning that the anisotropy is confined within the in-plane domain. Consequently, we can decouple the two terms once again, resulting in a system that is structurally identical to the isotropic case [34].

The energy in a bent plate arises from two sources: the stretching energy, which results from the in-plane deformation of the neutral surface, and the bending energy, which is due to the displacement in the transverse direction of the neutral surface. Primarily, the stretching energy significantly outweighs the bending energy, which can be disregarded. Nonetheless, if the neutral surface is deformed without any in-plane stretching, the stretching energy becomes negligible, leaving bending as the sole contributor to the total energy. This illustrates the interplay between geometry and elastic deformation; the plate tends to minimize stretching as much as possible [35]. Typically, if possible, the neutral surface shifts into a developable surface, which maintains an isomorphic relationship with the plane. According to the Gauss egregium theorem, such surfaces exhibit zero curvature, indicating an absence of stretching deformation.

2.1.2 Linear solution of a plate bent over a cylinder

In this chapter, we model the cell as a flat plate deformed into a cylinder with radius R, as shown in Figure 2.1. The reference frame used is the Cartesian system, where x and y represent the coordinates on the domain S^n, hereafter referred to as the *in-plane* coordinates, and $z \in [0, h]$ represents the *transverse direction* coordinate. Additionally, given the slight bending of the plate within this linear model, it is assumed that the surface normal does not change during deformation, leading to the specific boundary conditions:

$$\sigma_{xz}(x, y, z) = \sigma_{yz}(x, y, z) = \sigma_{zz}(x, y, z) = 0 \quad \text{for} \quad z \in \{0, h\}$$

where σ_{ij} are the components of Cauchy stress tensor. Moreover, since the thickness h is very small, this quantities must be small through the plate and, since they are zero at the boundary, we can assume that

$$\sigma_{xz}(x, y, z) = \sigma_{yz}(x, y, z) = \sigma_{zz}(x, y, z) = 0 \quad \forall (x, y, z) \in \Omega. \tag{2.1}$$

To proceed, it is necessary to choose a constitutive law that describes the material. In order to account for the bending of stress fibers and the aforementioned considerations, we assume a Hooke's response function for a transversely isotropic material. In Voigt notation, the strain-stress relationship is given by:

$$[\epsilon] = \begin{bmatrix} \frac{1}{E_p} & -\frac{\nu_{zp}}{E_z} & -\frac{\nu_{vp}}{E_p} & 0 & 0 & 0 \\ -\frac{\nu_{pz}}{E_p} & \frac{1}{E_z} & -\frac{\nu_{pz}}{E_p} & 0 & 0 & 0 \\ -\frac{\nu_p}{E_p} & -\frac{\nu_{zp}}{E_z} & \frac{1}{E_p} & 0 & 0 & 0 \\ 0 & 0 & 0 & \frac{1}{2G_{zp}} & 0 & 0 \\ 0 & 0 & 0 & 0 & \frac{(1+\nu_p)}{E_p} & 0 \\ 0 & 0 & 0 & 0 & 0 & \frac{1}{2G_{zp}} \end{bmatrix} [\sigma] \tag{2.2}$$

where $\frac{\nu_{pz}}{E_p} = \frac{\nu_{zp}}{E_z}$ is maintained to ensure tensor symmetry. This response function accounts for anisotropic behavior in the y direction, with there are no preferred directions in every plane orthogonal to it. Additionally, this elasticity tensor does not depend on the coordinate of a point, which implicitly implies that the symmetry group of the material is the same at every point in the body. This constitutive law comprises five independent coefficients: $E_p, \nu_p, E_z, \nu_{zp}, G_{zp}$.

The stress-strain relationship is computed directly by inverting the elasticity tensor in (2.2), thus implying

$$[\sigma] = \begin{bmatrix} \frac{1-\nu_{pz}\nu_{zp}}{E_pE_z\Delta} & \frac{\nu_{zp}+\nu_p\nu_{zp}}{E_pE_z\Delta} & \frac{\nu_p+\nu_{zp}\nu_{pz}}{E_pE_z\Delta} & 0 & 0 & 0 \\ \frac{\nu_{pz}+\nu_p\nu_{pz}}{E_p^2\Delta} & \frac{1-\nu_p^2}{E_p^2\Delta} & \frac{\nu_{pz}+\nu_p\nu_{pz}}{E_p^2\Delta} & 0 & 0 & 0 \\ \frac{\nu_p+\nu_{zp}\nu_{pz}}{E_pE_z\Delta} & \frac{\nu_{zp}+\nu_p\nu_{zp}}{E_pE_z\Delta} & \frac{1-\nu_{pz}\nu_{zp}}{E_pE_z\Delta} & 0 & 0 & 0 \\ 0 & 0 & 0 & 2G_{zp} & 0 & 0 \\ 0 & 0 & 0 & 0 & \frac{E_p}{1+\nu_p} & 0 \\ 0 & 0 & 0 & 0 & 0 & 2G_{zp} \end{bmatrix} [\epsilon] \tag{2.3}$$

where

$$\Delta = \frac{(1+\nu_p)(1-\nu_p-2\nu_{pz}\nu_{zp})}{E_p^2E_z}. \tag{2.4}$$

Hence, we can describe (2.1) in terms of strains

$$\begin{aligned} 0 = \sigma_{xz} &= \frac{E_p}{1+\nu_p}\epsilon_{xz} = \frac{E_p}{1+\nu_p}\epsilon_{yz} = \sigma_{yz} = 0, \\ 0 = \sigma_{zz} &= \frac{1}{E_pE_z\Delta}\big((1-\nu_{pz}\nu_{zp})\epsilon_{zz} + (\nu_p+\nu_{zp}\nu_{pz})\epsilon_{xx} + (\nu_{zp}+\nu_p\nu_{zp})\epsilon_{yy}\big). \end{aligned}$$

The first set of equations has a straightforward interpretation. Given the geometric meaning of ϵ_{xz} and ϵ_{yz}, the condition $\epsilon_{xz} = \epsilon_{yz} = 0$ implies that every material curve perpendicular to the neutral surface remains perpendicular to the deformed neutral surface after deformation. This condition, as previously mentioned, is known as the Kirchhoff hypothesis.

Therefore, by using the linear strain approximation and then integrating, we conclude

that

$$\begin{aligned} u_x(x,y,z) &= u_x^{\frac{h}{2}}(x,y) - \int_{\frac{h}{2}}^{z} \frac{\partial u_z}{\partial x}(x,y,t)dt, \\ u_y(x,y,z) &= u_y^{\frac{h}{2}}(x,y) - \int_{\frac{h}{2}}^{z} \frac{\partial u_z}{\partial y}(x,y,t)dt, \\ \epsilon_{zz} &= -\frac{1}{1-\nu_{pz}\nu_{zp}}\big((\nu_p + \nu_{zp}\nu_{pz})\epsilon_{xx} + (\nu_{zp} + \nu_p\nu_{zp})\epsilon_{yy}\big). \end{aligned} \tag{2.5}$$

where $u_i^{\frac{h}{2}}$ are the displacements of the neutral surface. In a linear framework, a good approximation of the transverse displacement u_z is the one of the neutral surface. In particular, the bending over a cylinder is described by the function

$$u_x^{\frac{h}{2}} = 0 \quad u_y^{\frac{h}{2}} = 0 \quad u_z^{\frac{h}{2}} = \xi(x,y) \tag{2.6}$$

and

$$\begin{aligned} \xi(x,y) = \xi(x) &= -(R + \frac{h}{2}) + (R + \frac{h}{2})\cos\left(\frac{x}{R + \frac{h}{2}}\right) = \\ &= \frac{1}{k_1} - \frac{1}{k_1}\cos(-k_1 x) \end{aligned} \tag{2.7}$$

where $k_1 = -\frac{1}{R+\frac{h}{2}}$ is the principal curvature of the cylinder in the angular direction. Note that we assume that the y axis is parallel to the cylinder's axis, where no deformation occurs.

However, the form can be easily adjusted by introducing a component dependent on a different curvature, specifically the one of the curve formed by the intersection of the cylinder with a plane orthogonal to the cylinder and parallel to z (or x). In fact, such curvature is given by $k_\theta = k_1 \sin^2(\theta)$.

Therefore, by substitution of u_z with ξ above in (2.5) and the application of the condition in (2.6), we get

$$\begin{cases} u_x(x,y,z) = -(z - \frac{h}{2})\frac{\partial \xi}{\partial x} = (z - \frac{h}{2})\sin(-k_1 x) \\ u_y(x,y,z) = -(z - \frac{h}{2})\frac{\partial \xi}{\partial y} = 0 \end{cases} \tag{2.8}$$

thus the displacements in the whole domain are a linear function of the transverse coordinate. Therefore, in the case that the direction of the fibers - here y - is parallel to the axis of the cylinder, the strain tensor field of the pure bending deformation ϵ_{ij}^b is computed directly as

$$[\epsilon_{ij}^b] = \left(z - \frac{h}{2}\right)\begin{bmatrix} -k_1\cos(-k_1 x) & 0 & 0 \\ 0 & 0 & 0 \\ 0 & 0 & k_1\frac{\nu_p + \nu_{pz}\nu_{zp}}{1-\nu_{zp}\nu_{pz}}\cos(-k_1 x) \end{bmatrix}. \tag{2.9}$$

Note that, since the displacement ξ is much smaller than the thickness h, we can make

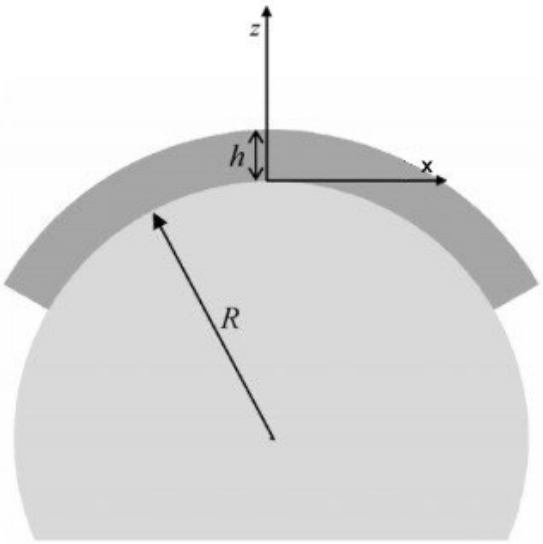

Figure 2.1. A two dimensional schematic of a cell of thickness h bent over a cylinder of radius R.

the approximation $\cos(-k_1 x) \approx 1$, which will be used from now on.

However, in order to study the optimal configuration of the stress fibers hence describing the remodelling, it is useful to choose as reference the configuration where the y axis is fixed on the stress fibers and forms an angle θ with the cylinder's axis direction. Thus, we introduce a change of reference frame

$$\begin{cases} x' = \cos(\theta)x - \sin(\theta)y \\ y' = \sin(\theta)x + \cos(\theta)y \end{cases} . \tag{2.10}$$

Thus, the strain in the reference system $(x', y', z' = z)$ is given by:

$$\epsilon'_{ij} = \frac{\partial x'_i}{\partial x_l}\frac{\partial x'_j}{\partial x_m}\epsilon_{lm}.$$

In matrix notation:

$$[\epsilon'_{ij}] = (z - \frac{h}{2}) \begin{bmatrix} -k_1\cos^2(\theta) & k_1\frac{\sin(2\theta)}{2} & 0 \\ k_1\frac{\sin(2\theta)}{2} & -k_1\sin^2(\theta) & 0 \\ 0 & 0 & \frac{k_1}{1-\nu_{zp}\nu_{pz}}[(\nu_p + \nu_{pz}\nu_{zp})\cos^2(\theta) + \nu_{zp}(1+\nu_p)\sin^2(\theta)] \end{bmatrix}. \tag{2.11}$$

The interpretation of the physical result is simple: for values greater than the neutral surface ($z > \frac{h}{2}$), the points are stretched, while for values below the neutral surface, the points are compressed. It's important to note that the strain in the transverse direction

does not contribute to the elastic energy since we assumed that the transverse strain σ_{zz} is zero in equation (2.1).

2.1.3 Stored elastic energy after bending

The knowledge of the strains and the choice of the constitutive response functions allow us to compute the stress field of the bent plate. By plugging (2.11) in (2.3), we get

$$\begin{aligned}
\sigma_{xx}(x,y,z) &= (z-\frac{h}{2})\frac{E_p}{1-\nu_{zp}\nu_{pz}}(-k_1)(\cos^2(\theta)+\nu_{zp}\sin^2\theta),\\
\sigma_{yy}(x,y,z) &= (z-\frac{h}{2})\frac{E_z}{1-\nu_{zp}\nu_{pz}}(-k_1)(\nu_{pz}\cos^2(\theta)+\sin^2(\theta)),\\
\sigma_{xy}(x,y,z) &= (z-\frac{h}{2})k_1 G_{zp}\sin(2\theta),
\end{aligned} \tag{2.12}$$

where, the last three equation of (2.12) refers as the *effective* constitutive relations for a plate computed on the strain above.

Finally, we are able to compute the bending energy density of the plate as

$$\begin{aligned}
F^b(x,y,z) &= \frac{1}{2}\sigma_{ij}\epsilon_{ij} = \\
&= \frac{1}{2}(z-\frac{h}{2})^2\Big[G_{zp}k_1^2\sin^2(2\theta)+\\
&+ k_1^2\cos^2(\theta)\frac{E_p}{1-\nu_{zp}\nu_{pz}}\big(\cos^2(\theta)+\nu_{zp}\sin^2\theta\big)\\
&+ k_1^2\sin^2(\theta)\frac{E_z}{1-\nu_{zp}\nu_{pz}}\big(\nu_{pz}\cos^2(\theta)+\sin^2(\theta)\big)\Big]
\end{aligned}$$

Thus, considering the symmetry condition $\nu_{pz}=\frac{E_p}{E_z}\nu_{zp}$, the expression becomes:

$$\begin{aligned}
F^b(x,y,z) &= (z-\frac{h}{2})^2\frac{k_1^2}{2(1-\nu_{pz}\nu_{zp})}\big[(1-\nu_{pz}\nu_{zp})G_{zp}\sin^2(2\theta)+E_p\cos^4(\theta)+E_z\sin^4(\theta)+\\
&\qquad + E_p\nu_{zp}\frac{sin^2(2\theta)}{4}+E_z\nu_{pz}\frac{\sin^2(2\theta)}{4}\big]\\
&= (z-\frac{h}{2})^2\frac{k_1^2}{2(1-\nu_{pz}\nu_{zp})}\big[(1-\nu_{pz}\nu_{zp})G_{zp}\sin^2(2\theta)+E_p\cos^4(\theta)+E_z\sin^4(\theta)+\\
&\qquad + E_p\nu_{zp}\frac{\sin^2(2\theta)}{2}\big]\\
&= (z-\frac{h}{2})^2\frac{k_1^2}{2(1-\nu_{pz}\nu_{zp})}\big[E_p\cos^4(\theta)+\big((1-\nu_{zp}\nu_{pz})G_{zp}+\frac{1}{2}E_p\nu_{zp}\big)\sin^2(2\theta)+E_z\sin^4(\theta)\big]
\end{aligned}$$

concluding that

$$F^b = (z-\frac{h}{2})^2 \frac{k_1^2}{2(1-\nu_{pz}\nu_{zp})}\left[E_p \cos^4(\theta) + \left((1-\nu_{zp}\nu_{pz})G_{zp} + \frac{1}{2}E_p\nu_{zp}\right)\sin^2(2\theta) + E_z \sin^4(\theta)\right]. \tag{2.13}$$

The bending energy (2.13) is a quadratic form evaluated in the variables $(\cos(\theta), \sin(\theta))$. The angle θ^* that minimizes the bending energy depends on the ratios of the material anisotropy coefficients. If the elastic coefficient E_z is much larger than E_p, which describes a scenario where the stress fibers are difficult to bend compared to the rest of the body, the optimal angle θ^* tends to be as close to $\theta^* = 0$ as possible, i.e., the case where the fibers are parallel to the cylinder's axis.

Moreover, it can be show that this result is a generalization of the one achieved by Biton and Safran. In fact, if we assume

$$\begin{aligned} (1-\nu_{zp}\nu_{pz})G_{zp} + \frac{1}{2}E_p\nu_{zp} &= \frac{1}{2}E_p \\ E_z = E_p + \tilde{E}_z \quad \text{where} \quad \tilde{E}_z &> 0 \end{aligned} \tag{2.14}$$

it follows that

$$\begin{aligned} F^b(x,y,z) = (z-\frac{h}{2})^2 \frac{k_1^2}{2(1-\nu_{pz}\nu_{zp})}\left[E_p(cos^2+sin^2)^2 + \tilde{E}_z sin^4(\theta)\right] = \\ = (z-\frac{h}{2})^2 \frac{k_1^2}{2(1-\nu_{pz}\nu_{zp})}\left[E_p + \tilde{E}_z sin^4(\theta)\right], \end{aligned}$$

thus the energy is described by an isotropic part, namely proportional to E_p, and the anisotropic part proportional to E_z. It is clear that the energy is minimized for $\theta^* = 0$ given that E_z is positive. Moreover, it is noted that the energy penalty due to fiber bending is proportional to $\sin^4(\theta)$. Biton and Safran account for this term separately, postulating that fibers behave as elastic rods:

$$F^{sf} \propto K k_1^2 \sin^4(\theta)$$

where K represents the bending modulus of the rod.

2.1.4 Relationship between I_4 and F^b

In earlier sections, we developed a model by selecting a response function for the stress. Typically, within the context of anisotropy, an alternative approach is to define an elastic energy function. For the transversely isotropic case, this function is denoted by $\mathscr{U}(\mathbb{E}) = \mathscr{U}(I_1, I_2, I_3, I_4, I_5)$ [23], incorporating the isotropic invariants I_1, I_2, and I_3, as well as the anisotropic invariants I_4 and I_5, which account for the anisotropic behavior. Specifically, given a fiber direction $\mathbf{N}$, the tensor $\mathbb{A} = \mathbf{N} \times \mathbf{N}$ represents the material's structure tensor. In this constitutive framework, stress is computed directly from the elastic energy through its derivative with respect to the deformation tensor $\mathbb{F}$. Elastic materials for which properties are characterized by a strain-energy function W are referred as hyperelastic.

In our scenario, the fibers are oriented at an angle θ with the y-axis, hence $\mathbf{N} = (\cos(\theta), \sin(\theta), 0)$. Therefore, the material's structure tensor $\mathbb{A}$ is given by:

$$\mathbb{A} = (\cos(\theta), \sin(\theta), 0) \otimes (\cos(\theta), \sin(\theta), 0) = \begin{bmatrix} \cos^2(\theta) & \sin(2\theta)/2 & 0 \\ \sin(2\theta)/2 & \sin^2(\theta) & 0 \\ 0 & 0 & 0 \end{bmatrix}. \tag{2.15}$$

Using the bending strain (2.12), we can calculate I_4 as:

$$I_4 = \mathbb{E} : \mathbb{A} = -(z - \frac{h}{2}) k_1 \cos^2(\theta).$$

The bending energy (2.13) can be expressed as:

$$\begin{aligned} \mathscr{U}^b =& (z - \frac{h}{2})^2 \frac{k_1^2}{2(1 - \nu_{pz}\nu_{zp})} \left[E_p \cos^4(\theta) + \tilde{G} \sin^2(2\theta) + E_z \sin^4(\theta) \right] = \\ =& (z - \frac{h}{2})^2 \frac{k_1^2}{2(1 - \nu_{pz}\nu_{zp})} \left[(E_p - 4\tilde{G} + E_z) \cos^4(\theta) + (4\tilde{G} - 2E_z) \cos^2(\theta) + E_z \right] \end{aligned} \tag{2.16}$$

where $\tilde{G} = (1 - \nu_{zp}\nu_{pz}) G_{zp} + \frac{1}{2} E_p \nu_{zp}$.
The following observations regarding this term are relevant:

- It depends on $(z - \frac{h}{2})^2$ (i.e., it's proportional to h^3 upon integration).
- It depends on k_1^2.
- It has a linear dependence on $\cos^2(\theta)$, hence there should be a linear dependence on I_4.

It is evident that the only combination of invariants that satisfies these observations is given by I_4 and $I_1 = \mathrm{tr}(\mathbb{E})$. Indeed, the other isotropic invariants are proportional to higher powers of k_1 and h. Therefore, we can express the elastic energy as follows, referring to [23]:

$$\begin{aligned} \mathscr{U}^b = U_{\mathrm{an}}(I_4) + U_{\mathrm{mix}}(I_1 I_4) + U_{\mathrm{iso}}(I_1) = K_{44} I_4^2 + 2K_{14} I_1 I_4 + K_{11} I_1^2 = \\ = (z - \frac{h}{2})^2 k_1^2 \left(K_{44} \cos^4(\theta) + 2K_{14} \tilde{I}_1 \cos^2(\theta) + K_{11} \tilde{I}_1{}^2 \right) \end{aligned} \tag{2.17}$$

Finally, by substituting the value

$$\tilde{I}_1 = -\mathrm{tr}(\mathbb{E}) = \frac{1 - \nu_p - 2\nu_{pz}\nu_{zp}}{1 - \nu_{pz}\nu_{zp}} \tag{2.18}$$

and comparing it with equation (2.16), the equality holds by choosing

$$\begin{aligned} K_{44} &= \frac{E_p - 4\tilde{G} + E_z}{1 - \nu_{zp}\nu_{pz}}, \\ K_{14} &= \frac{2\tilde{G} - E_z}{1 - \nu_p - 2\nu_{zp}\nu_{pz}}, \\ K_{11} &= \frac{1 - \nu_{pz}\nu_{zp}}{(1 - \nu_{pz}\nu_{zp})^2}. \end{aligned} \tag{2.19}$$

We suggest that to describe the system in the hyperelastic neo-Hookean constitutive framework, it is necessary to introduce a mixed term coupling the first invariant I_1 with the anisotropic invariant I_4. Moreover, since we are working within linear elasticity, the contribution from I_4 cannot be distinguished from that of I_5, hence it is unnecessary to add I_5 as a parameter in the model.

We conclude that the linear model adopted in the preceding section can be described in the hyperelastic context with the introduction of the mixed term mentioned above.

2.2 Contribution of Active Contractility

Stress fibers play a pivotal role in cellular contractility. These fibers consist of a bipolar array of actin filaments and display a periodic pattern of α-actinin and myosin localization, akin to muscle myofibrils [36, 37]. This similarity suggests that contractility is significant in the total energy stored within the cell.

To describe the energy from contractility, we assume that cell adhesion to the substrate is stronger than the forces generated by active contractility. This is supported by observations of cells on rubber substrates, which show wrinkles without detaching, indicating that shear stress from fibers is insufficient to disrupt adhesion sites. Furthermore, experiments show that active contractility can enhance cellular adhesion [38, 39].

This assumption allows us to consider that there are no displacements at the cell-substrate interface due to contractility alone, expressed as:

$$u_x^c(x, y,0) = u_y^c(x, y,0) = u_z^c(x, y,0) = 0. \tag{2.20}$$

Thus, we permit cell deformation on the basal surface due to bending, but not due to stress fiber contractility.

Biton and Safran [15] introduced a model where the active contractility of the fibers yields a compressive strain. Hence, since the attached surface cannot deform, it results in significant displacements of the upper surface relative to the lower one, indeed resulting in a shear stress. Therefore, the displacement of a material point is proportional to both the distance from the plate's center and the height.

This suggests a shear stress of the form:

$$\sigma_{yz} = \tau\frac{y}{r}, \quad \sigma_{xz} = 0 \tag{2.21}$$

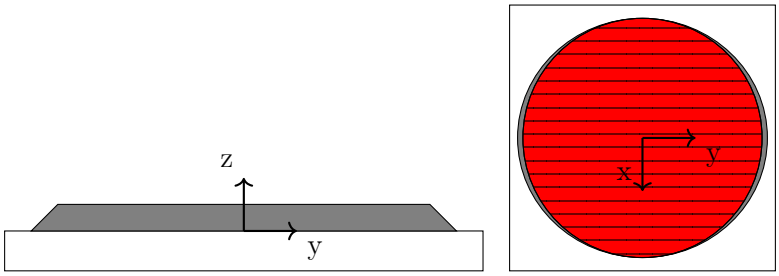

Figure 2.2. Schematic of the deformation induced by the active contractility of the stress fibers. Notice that the y direction is parallel to the stress fibers direction

where τ represents the contractile force, and r is the (immaterial) radius of the cell. Using the anisotropic constitutive relations (2.3), the shear strains are given by:

$$\epsilon_{yz} = \frac{1}{2G_{zp}}\tau\frac{y}{r}, \quad \epsilon_{xz} = 0. \tag{2.22}$$

Here, τ is negative, representing the compression induced by the SFs. The shear strain field is negative throughout the body, starting from zero at the basal surface and linearly decreasing to its minimum at the upper surface, as shown in Figure 2.2. Since y is the direction of the cell fibers, the lack of shear stress in the other direction is due to assumed transverse anisotropy. However, this assumption can be modified to include an orthotropic description of the cell, adding a contractility term in the other direction.

In the absence of external forces, the transverse equilibrium equation implies:

$$\frac{\partial\sigma_{zz}}{\partial z} = -\frac{\partial\sigma_{yz}}{\partial y} = -\frac{\tau}{r}.$$

Integrating over the thickness and using the stress-free condition at the apical surface gives:

$$\sigma_{zz}(z) = (1 - \frac{z}{h})\frac{h}{r}\tau. \tag{2.23}$$

Thus, σ_{zz} is a linear function of z. The other normal stresses σ_{xx} and σ_{yy} are also functions of z only:

$$\sigma_{xx} = \sigma_{xx}(z), \quad \sigma_{yy} = \sigma_{yy}(z), \quad \sigma_{zz}(z) = (1 - \frac{z}{h})\frac{h}{r}\tau. \tag{2.24}$$

This shows that the trace of the stress tensor is an affine function of z only. Therefore, the trace of the strain is also a function of z only:

$$\epsilon_{xx} = \epsilon_{xx}(z), \quad \epsilon_{yy} = \epsilon_{yy}(z), \quad \epsilon_{zz} = \epsilon_{zz}(z).$$

This implies that u_z is only a function of z, i.e., $u_z = u_z(z)$. Using this, we can solve

for the displacement due to active contractility. The in-plane displacement follows:

$$\begin{aligned} \frac{\partial u_y}{\partial z} = \frac{1}{G_{zp}}\tau\frac{y}{r} - \frac{\partial u_z}{\partial y} = \frac{1}{G_{zp}}\tau\frac{y}{r}, \\ \frac{\partial u_x}{\partial z} = 0 \end{aligned} \tag{2.25}$$

which, upon integration and using the boundary condition, gives:

$$\begin{aligned} u_y(y,z) = \frac{1}{G_{zp}}\tau\frac{yz}{r}, \\ u_x(x,z) = 0. \end{aligned} \tag{2.26}$$

Finally, the expression for u_z can be computed from the constitutive law (2.3):

$$\frac{\partial u_z}{\partial z} = \epsilon_{zz} = -\frac{\nu_p}{E_p}\sigma_{xx} - \frac{\nu_{zp}}{E_z}\sigma_{yy} + \frac{1}{E_p}\sigma_{zz}. \tag{2.27}$$

To solve the system, the in-plane stresses are expressed in terms of ϵ_{zz} using the constitutive equations (2.3):

$$\begin{aligned} \sigma_{xx} &= \frac{1}{E_p E_z \Delta}\left[(1-\nu_{pz}\nu_{zp})\epsilon_{xx} + (\nu_{zp}+\nu_p\nu_{zp})\epsilon_{yy} + (\nu_p+\nu_{zp}\nu_{pz})\epsilon_{zz}\right] = \\ &= \frac{1}{E_p E_z \Delta}\left[(\nu_p+\nu_{zp}\nu_{pz})\epsilon_{zz} + \frac{\nu_{zp}(1+\nu_p)}{G_{zp}}\tau\frac{z}{r}\right] \end{aligned} \tag{2.28}$$

and

$$\begin{aligned} \sigma_{yy} &= \frac{1}{E_p^2 \Delta}\left[\nu_{pz}(1+\nu_p)\epsilon_{xx} + (1-\nu_p^2)\epsilon_{yy} + \nu_{pz}(1+\nu_p)\epsilon_{zz}\right] = \\ &= \frac{1}{E_p^2 \Delta}\left[\nu_{pz}(1+\nu_p)\epsilon_{zz} + \frac{(1-\nu_p^2)}{G_{zp}}\tau\frac{z}{r}\right]. \end{aligned} \tag{2.29}$$

By substituting (2.28) and (2.29) into (2.27), we isolate the transverse strain ϵ_{zz}:

$$\begin{aligned} \epsilon_{zz} =& -\frac{\nu_p}{E_p}\sigma_{xx} - \frac{\nu_{zp}}{E_z}\sigma_{yy} + \frac{1}{E_p}\sigma_{zz} = \\ =& -\frac{\nu_p}{E_p^2 E_z \Delta}\left[(\nu_p+\nu_{zp}\nu_{pz})\epsilon_{zz} + \frac{\nu_{zp}(1+\nu_p)}{G_{zp}}\tau\frac{z}{r}\right] + \\ & -\frac{\nu_{zp}}{E_p^2 E_z \Delta}\left[\nu_{pz}(1+\nu_p)\epsilon_{zz} + \frac{(1-\nu_p^2)}{G_{zp}}\tau\frac{z}{r}\right] \\ & + \frac{1}{E_p}(1-\frac{z}{h})\frac{h}{r}\tau. \end{aligned}$$

Thus,

$$\left[1+\frac{1}{E_p^2E_z\Delta}(\nu_p^2+2\nu_p\nu_{zp}\nu_{pz}+\nu_{zp}\nu_{pz})\right]\epsilon_{zz}=\frac{1}{E_p}(1-\frac{z}{h})\frac{h}{r}\tau- \\ -\frac{1}{G_{zp}E_p^2E_z\Delta}\left[\nu_p\nu_{zp}(1+\nu_p)+\nu_{zp}(1-\nu_p^2)\right]\tau\frac{z}{r}. \tag{2.30}$$

Simplifying with the definition of Δ in (2.4) yields:

$$\frac{1-\nu_{pz}\nu_{zp}}{(1+\nu_p)(1-\nu_p-2\nu_{pz}\nu_{zp})}\epsilon_{zz}=\frac{1}{E_p}(1-\frac{z}{h})\frac{h}{r}\tau-\frac{\nu_{zp}}{G_{zp}(1-\nu_p-2\nu_{pz}\nu_{zp})}\tau\frac{z}{r}.$$

Thus,

$$\frac{\partial u_z}{\partial z}=\epsilon_{zz}=\frac{(1+\nu_p)(1-\nu_p-2\nu_{pz}\nu_{zp})}{E_p(1-\nu_{pz}\nu_{zp})}(1-\frac{z}{h})\tau\frac{h}{r}-\frac{\nu_{zp}(1+\nu_p)}{G_{zp}(1-\nu_{pz}\nu_{zp})}\tau\frac{z}{r}. \tag{2.31}$$

Finally, integrating over z and applying the boundary condition (2.20), we obtain:

$$u_z(z)=\frac{(1+\nu_p)}{E_pG_{zp}(1-\nu_{pz}\nu_{zp})}\frac{\tau}{r}\left[G_{zp}(1-\nu_p-2\nu_{zp}\nu_{pz})h-[G_{zp}(1-\nu_p-2\nu_{zp}\nu_{pz})+E_p\nu_{zp}]\frac{z}{2}\right]z \tag{2.32}$$

In summary, we computed the strains and the stresses induced by the contractility of the stress fibers. We shall highlight some properties of the computed quantities. First of all, note that, since the contractility is generated by the fibers, in a reference frame that rotates accordingly to the fibers (i.e., solidal to the cell), there is no role played by the angle θ. Therefore, on a flat substrate, the energy contribution of the contractility will be the same independent of the orientation angle θ. Nonetheless, whenever the plate is bent, the cell energy exhibits a mixed term that arises from both contractility and deformation; this term will play a crucial role in the remodeling process, as we will discuss later.

Moreover, it is worth noting that both the contractile strains and the bending strains are affine functions of the transverse coordinate z. Thus, the expression of the shear stress introduced in [15] was not random; indeed, it ensures that the energy contribution of the contractility has the same order of magnitude (in terms of the parameter h) as the pure bending energy, hence ensuring the competition between these terms.

2.3 Stability of θ-Configurations

The elastic energy of a cell subjected to bending and active contractility forces of stress fibers depends on the total gradient of deformation $\mathbb{F}=\mathbb{F}^b\mathbb{F}^c$, where $\mathbb{F}^b$ describes the bending deformation and $\mathbb{F}^c$ accounts for contractility. In the small strains regime, the following approximation holds:

$$\mathbb{F}=\mathbb{F}^b\mathbb{F}^c\approx(\mathbb{I}+\nabla u^b)(\mathbb{I}+\nabla u^c)\approx\mathbb{I}+\nabla u^b+\nabla u^c.$$

This allows the effects of bending and active contractility to be separated, leading to the following additive decomposition:

$$\begin{aligned}[\epsilon_{ij}] &= [\epsilon^b_{ij}] + [\epsilon^c_{ij}],\\ [\sigma_{ij}] &= [\sigma^b_{ij}] + [\sigma^c_{ij}].\end{aligned} \tag{2.33}$$

Thus, the total elastic energy of the system is split into three terms:

$$F = \frac{1}{2}(\sigma^b_{ij}\epsilon^b_{ij} + \sigma^b_{ij}\epsilon^c_{ij} + \sigma^c_{ij}\epsilon^b_{ij} + \sigma^c_{ij}\epsilon^c_{ij}) = F^b + F^m + F^c, \tag{2.34}$$

where F^b represents the energy due to the bending of the plate, $F^m = \frac{1}{2}(\sigma^b_{ij}\epsilon^c_{ij} + \sigma^c_{ij}\epsilon^b_{ij})$ is the energy due to the interaction of active contractility with the bending deformation, and F^c is the energy due to pure active contractility. Notably, F^c does not depend on the angle θ and is thus neglected in the stability computation of θ-configurations.

Due to the linear constitutive equations and the symmetry of the elasticity tensor, it can be shown that $\sigma^b_{ij}\epsilon^c_{ij} = \sigma^c_{ij}\epsilon^b_{ij}$, thus the mixed energy term can be written as $F^m = \sigma^b_{ij}\epsilon^c_{ij}$. We can compute it directly using the stresses and contractility strains:

$$F^m = \sigma^b_{ij}\epsilon^c_{ij} = \sigma^b_{xx}\epsilon^c_{xx} + \sigma^b_{yy}\epsilon^c_{yy} + \sigma^b_{zz}\epsilon^c_{zz} + \sigma^b_{xy}\epsilon^c_{xy} + 2\sigma^b_{xz}\epsilon^c_{xz} + 2\sigma^b_{yz}\epsilon^c_{yz} = \sigma^b_{yy}\epsilon^c_{yy}.$$

Therefore, the total energy can be explicitly written by substituting (2.13) and (2.3):

$$\begin{aligned}F = (z-\frac{h}{2})^2\frac{k_1^2}{2(1-\nu_{pz}\nu_{zp})}\left[E_p\cos^4(\theta) + \left((1-\nu_{zp}\nu_{pz})G_{zp} + \frac{1}{2}E_p\nu_{zp}\right)\sin^2(2\theta) + E_z\sin^4(\theta)\right]\\ -(z-\frac{h}{2})\frac{z}{r}\tau\frac{E_z}{G_{zp}(1-\nu_{zp}\nu_{pz})}k_1(\nu_{pz}\cos^2(\theta)+\sin^2(\theta)) + F^c.\end{aligned} \tag{2.35}$$

The different components of the total energy reveal some interesting features:

- Each term is proportional to y^2, indicating the same order in the thickness h.
- The mixed energy F^m scales as k_1, while the bending energy scales as k_1^2, reflecting a balance between bending energy and contractility.
- The power of trigonometric functions in F^m is lower than that in F^b, implying a linear relation with the anisotropic invariant I_4.

The bending of the cell over the cylinder results in extension above the neutral surface and compression below it. Conversely, active contractility induces a compression strain field increasing towards the upper surface of the cell, partially relieving the extension due to bending and thereby reducing stored internal energy. This interplay explains the superposition of these deformations, as illustrated in Figure 2.3.

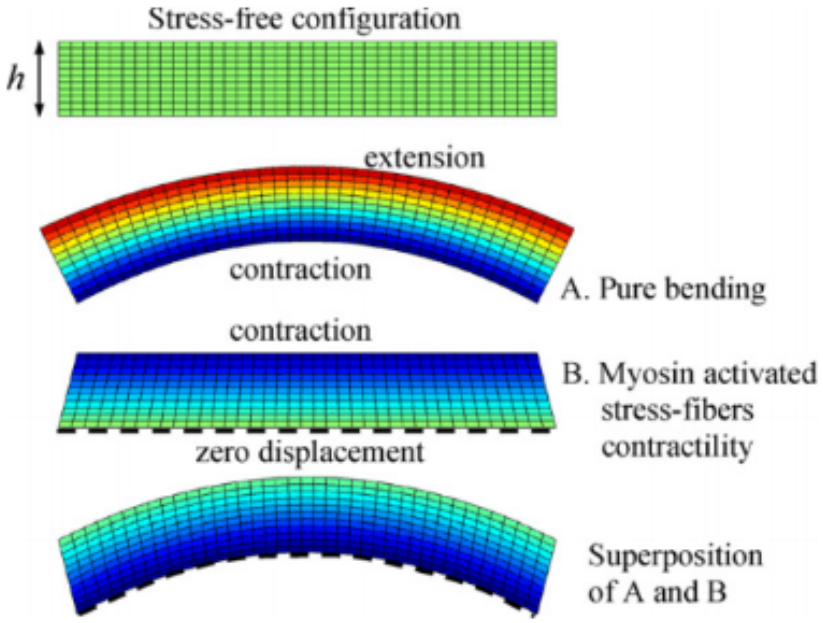

Figure 2.3. A schematic description of the deformation due to bending and active contractility of SFs. Notice that contractility deformation reduces the extension due to bending. The color code indicates the strains in the x direction.

The goal is to analyze the optimal orientation angle minimizing the stored energy of the cell. Assuming smooth functions in the variable θ, we determine stationary angles and their stability by computing the first and second derivatives of the energy with respect to θ.

The total elastic energy, after integrating across the cell volume, is expressed as:

$$\begin{aligned}\mathscr{U} &= \frac{Ah^3}{24(1-\nu_{pz}\nu_{zp})}k_1^2\left[E_p\cos^4(\theta)+\tilde{G}\sin^2(2\theta)+E_z\sin^4(\theta)\right] \\ &\quad -\frac{Ah^3E_z}{12G_{zp}(1-\nu_{pz}\nu_{zp})}\frac{\tau}{r}k_1\left(\nu_{pz}\cos^2(\theta)+\sin^2(\theta)\right) \\ &= \frac{Ah^3}{24(1-\nu_{pz}\nu_{zp})}[k_1^2\left(E_p\cos^4(\theta)+\tilde{G}\sin^2(2\theta)+E_z\sin^4(\theta)\right) \\ &\quad -2k_1E_z\alpha\left(\nu_{pz}\cos^2(\theta)+\sin^2(\theta)\right)]\end{aligned} \tag{2.36}$$

where $\alpha=\frac{1}{G_{zp}}\frac{\tau}{r}<0$ and A is the area of the neutral surface.

2.3.1 Critical Configuration and Stability: Active Contractility Contribution

First, we examine the contribution from active contractility alone. The stationary configurations of this term are solutions to:

$$0 = \frac{\partial \mathscr{U}^c}{\partial \theta} = -\frac{h^3 E_z}{12(1-\nu_{pz}\nu_{zp})} k_1 \alpha (1-\nu_{pz}) \sin(2\theta). \tag{2.37}$$

Thus, the only stationary configurations are $\theta_0 = 0$ and $\theta_1 = \frac{\pi}{2}$. The stability is determined by the convexity:

$$\frac{\partial^2 \mathscr{U}^c}{\partial \theta^2} = -\frac{h^3 E_z}{6(1-\nu_{pz}\nu_{zp})} k_1 \alpha (1-\nu_{pz}) \cos(2\theta). \tag{2.38}$$

Since $(1-\nu_{pz})\alpha < 0$, we have:

- $\frac{\partial^2 \mathscr{U}^c}{\partial \theta^2}(\theta_0) < 0$, hence $\theta_0 = 0$ is unstable.
- $\frac{\partial^2 \mathscr{U}^c}{\partial \theta^2}(\theta_1) > 0$, hence $\theta_1 = \frac{\pi}{2}$ is a stable configuration.

This result aligns with findings by Biton and Safran [15], where active contractility also aligns SFs along the maximal curvature direction. For large values of E_z, the bending of the plate aligns the fibers towards the axis of the cylinder, creating a trade-off between bending and contractility effects, as demonstrated next.

2.3.2 Critical Configuration and Stability: Competition Between Bending and Active Contractility

Now, we study the stationary configurations of the total energy $\mathscr{U}$, which includes all the energy terms mentioned above, except for the pure contractility energy term. After derivation, we have that

$$0 = \frac{\partial \mathscr{U}}{\partial \theta} = \frac{h^3}{12(1-\nu_{zp}\nu_{pz})} \Big[k_1^2 \big(2\tilde{G}\cos(2\theta) + E_z \sin^2(\theta) - E_p \cos^2(\theta)\big) - k_1 E_z \alpha (1-\nu_{pz}) \Big] \sin(2\theta). \tag{2.39}$$

Therefore, besides the trivial ones given by $\theta_0 = 0$ and $\theta_1 = \frac{\pi}{2}$, there may exist an oblique angle configuration θ^* given by:

$$k_1^2 \big(2\tilde{G}\cos(2\theta^*) + E_z \sin^2(\theta^*) - E_p \cos^2(\theta^*)\big) - k_1 E_z \alpha (1-\nu_{pz}) = 0. \tag{2.40}$$

This is satisfied if and only if

$$\cos^2(\theta^*) = \frac{k_1(2\tilde{G} - E_z) + \alpha(E_z - E_p\nu_{zp})}{k_1(4\tilde{G} - E_z - E_p)}. \tag{2.41}$$

Therefore, there exists a third stationary configuration θ^* if and only if

$$\begin{aligned}\frac{k_1(2\tilde{G}-E_z)+\alpha(E_z-E_p\nu_{zp})}{k_1(4\tilde{G}-E_z-E_p)}>0,\\ \frac{k_1(2\tilde{G}-E_p)-\alpha(E_z-E_p\nu_{zp})}{k_1(4\tilde{G}-E_z-E_p)}>0.\end{aligned} \tag{2.42}$$

The stability of these configurations is given by the signs of the second derivative computed in the configurations. In particular, the second derivative is given by

$$\begin{aligned}\frac{\partial^2\mathscr{U}}{\partial\theta^2} &= B(\nu_{zp},\nu_{pz})\Big[k_1^2\big(-4\tilde{G}\sin(2\theta)+E_z 2\sin(\theta)\cos(\theta)+E_p 2\sin(\theta)\cos(\theta)\big)\sin(2\theta)+\\ &\qquad +\big(k_1^2(2\tilde{G}\cos(2\theta)+E_z\sin^2(\theta)-E_p\cos^2(\theta))-k_1\alpha(E_z-E_p\nu_{zp})\big)2\cos(2\theta)\Big]\\ &= B(\nu_{zp},\nu_{pz})\Big[4k_1^2\tilde{G}(\cos^2(2\theta)-\sin^2(2\theta))+k_1^2(E_z+E_p)\sin^2(2\theta)\\ &\qquad +2k_1^2(E_z\sin^2(\theta)-E_p\cos^2(\theta))\cos(2\theta)-2k_1\alpha(E_z-E_p\nu_{zp})\cos(2\theta)\Big].\end{aligned} \tag{2.43}$$

where $B(\nu_{zp},\nu_{pz})=\frac{h^3}{12(1-\nu_{zp}\nu_{pz})}$. The stability of the trivial configuration follows:

$$\begin{aligned}\theta_0=0 \quad \text{stable} \quad &\iff k_1(2\tilde{G}-E_p)-\alpha(E_z-E_p\nu_{zp})<0,\\ \theta_1=\frac{\pi}{2} \quad \text{stable} \quad &\iff k_1(2\tilde{G}-E_z)+\alpha(E_z-E_p\nu_{zp})<0.\end{aligned} \tag{2.44}$$

Moreover, if it exists, θ^* is a stable configuration if

$$\frac{\partial^2\mathscr{U}}{\partial\theta^2}(\theta^*)=B(\nu_{zp},\nu_{pz})k_1^2(E_z+E_p-4\tilde{G})\sin^2(2\theta^*)>0 \tag{2.45}$$

which holds if and only if $(4\tilde{G}-E_p-E_z)<0$.

In conclusion, there are multiple cases to consider, depending on the constitutive coefficients of (2.3) and on the ratio of α and k_1. In particular, suppose that θ^* does not exist. The existence above implies that one between θ_0 and θ_1 is necessarily unstable. This may be seen directly, for example, in the case that $\theta_1=\frac{\pi}{2}$ is stable and $\theta_0=0$ is unstable it must hold

$$\begin{aligned}k_1(2\tilde{G}-E_p)-\alpha(E_z-E_p\nu_{zp})>0\\ k_1(2\tilde{G}-E_z)+\alpha(E_z-E_p\nu_{zp})<0\end{aligned} \tag{2.46}$$

hence surely one of the existence conditions (2.41) is not satisfied. The same argument can be made if we assume that θ_1 is unstable and θ_2 is stable.

On the other hand, let's assume that θ^* exists. Thus, if we also suppose that it is stable, i.e. $(4\tilde{G} - E_p - E_z) < 0$, then from (2.44) the trivial configurations are automatically unstable and vice versa. Indeed, this may be concluded from the fact that, if we assume that θ^* exists, then it holds either:

$$\begin{aligned} k_1(2\tilde{G} - E_p) - \alpha(E_z - E_p\nu_{zp}) > 0 \\ k_1(2\tilde{G} - E_z) + \alpha(E_z - E_p\nu_{zp}) > 0 \end{aligned} \tag{2.47}$$

or

$$\begin{aligned} k_1(2\tilde{G} - E_p) - \alpha(E_z - E_p\nu_{zp}) < 0 \\ k_1(2\tilde{G} - E_z) + \alpha(E_z - E_p\nu_{zp}) < 0 \end{aligned} \tag{2.48}$$

depending on the sign of the denominator. In summary, the following cases are admissible:

- θ^* does not exist
  - $\theta_0 = 0$ stable and $\theta_1 = 0$ unstable.
  - $\theta_1 = \frac{\pi}{2}$ stable and $\theta_0 = 0$ unstable.
- θ^* exists
  - θ^* stable $\iff (4\tilde{G} - E_z - E_p) < 0$ ($\iff \theta_0, \theta_1$ unstable)
  - θ^* unstable $\iff (4\tilde{G} - E_z - E_p) > 0$ ($\iff \theta_0, \theta_1$ stable)

Notice that these results hold only if the curvature k_1 is negative, hence they cannot explain the case of the cell bending over a concave surface.

2.3.3 Bifurcation analysis

In the following, we discuss the bifurcation analysis of the optimal configuration. For clarity, we will use the ratio $\Lambda = \frac{\alpha}{k_1} = \frac{1}{G_{zp}}\frac{\tau}{k_1 r}$ as the bifurcation parameter, which describes the competition between contractility effects and bending ones. This parameter choice is directly suggested by (2.41). Indeed, we observe that

$$\begin{aligned} \cos^2(\theta^*) &= \frac{k_1(2\tilde{G} - E_z) + \alpha(E_z - E_p\nu_{zp})}{k_1(4\tilde{G} - E_z - E_p)} \\ &= \frac{2\tilde{G} - E_z}{4\tilde{G} - E_z - E_p} + \frac{(E_z - E_p\nu_{zp})}{4\tilde{G} - E_z - E_p}\frac{\alpha}{k_1} \\ &= \frac{2\tilde{G} - E_z}{K} + \frac{(E_z - E_p\nu_{zp})}{K}\Lambda \end{aligned} \tag{2.49}$$

where in the last step we defined $K := 4\tilde{G} - E_z - E_p$. Hence, $\cos^2(\theta^*)$ is an affine function of the ratio Λ with a slope given by $\frac{E_z - E_p\nu_{zp}}{K}$. Moreover, note that there exist

two distinct critical values of the parameter Λ that depend on the material parameters only and describe the bifurcation points. These values are computed directly by equating to zero the inequalities in (2.44):

$$\begin{aligned}(2\tilde{G} - E_p) - \frac{\alpha}{k_1}(E_z - E_p\nu_{zp}) = 0\\ (2\tilde{G} - E_z) + \frac{\alpha}{k_1}(E_z - E_p\nu_{zp}) = 0\end{aligned} \tag{2.50}$$

which implies the two bifurcation points:

$$\Lambda_\parallel = \frac{(2\tilde{G} - E_p)}{(E_z - E_p\nu_{zp})}, \quad \Lambda_\perp = -\frac{(2\tilde{G} - E_z)}{(E_z - E_p\nu_{zp})}. \tag{2.51}$$

These two points can be used to visualize (2.49) more effectively. Indeed, it can be shown directly that:

$$\cos^2(\theta^*) = -\frac{\Lambda_\perp}{\Lambda_\perp - \Lambda_\parallel} + \frac{1}{\Lambda_\perp - \Lambda_\parallel}\Lambda. \tag{2.52}$$

Notice that the bifurcation points in (2.51) are related to each other depending on the sign of $K = 4\tilde{G} - E_z - E_p$, which, as stated above, describes the stability of the oblique configuration θ^*. In particular, it is straightforward to show that

$$\begin{aligned}K < 0 \implies \Lambda_\parallel < \Lambda_\perp\\ K > 0 \implies \Lambda_\perp < \Lambda_\parallel\end{aligned} \tag{2.53}$$

hence we will discuss these cases separately.

Firstly, assume that $K = 4\tilde{G} - E_z - E_p < 0$. From the previous consideration, we know that, if it exists, θ^* is stable. The stability of the stationary configurations is then summarized as follows:

$$\begin{aligned}\theta = 0 \quad &\text{stable} \iff \Lambda < \Lambda_\parallel = \frac{(2\tilde{G} - E_p)}{(E_z - E_p\nu_{zp})}\\ \theta = \frac{\pi}{2} \quad &\text{stable} \iff \Lambda > \Lambda_\perp = -\frac{(2\tilde{G} - E_z)}{(E_z - E_p\nu_{zp})}\\ \theta = \theta^* \quad &\text{stable} \iff \Lambda_\perp > \Lambda > \Lambda_\parallel.\end{aligned} \tag{2.54}$$

Nonetheless, there are two relevant cases to discuss, depending on whether $\Lambda_\parallel < 0$ or $\Lambda_\parallel > 0$. This distinction is necessary since the ratio $\Lambda = \frac{\alpha}{k_1}$ assumes only positive values as both arguments are negative. Therefore, if the critical point $\Lambda_\parallel < 0$, the parallel configuration is always unstable, implying that there exist only two stable configurations, whose stability depends on the value of Λ. This behavior is the one observed in Biton and Safran [15], where the parallel configuration $\theta_0 = 0$ is never stable. We will address this later. On the other hand, if $\Lambda_\parallel > 0$, there are three possible stable configurations, depending, for a fixed value of the parameter α, on the value of the curvature k_1. In

particular, as shown in Figure 2.4, if the curvature is low enough compared to the contractility parameter α, i.e., Λ is large, the orthogonal configuration $\theta = \frac{\pi}{2}$ is preferred. Nonetheless, when the curvature is sufficiently high, the bending effect causes the angle to reorient to an oblique configuration θ^*.

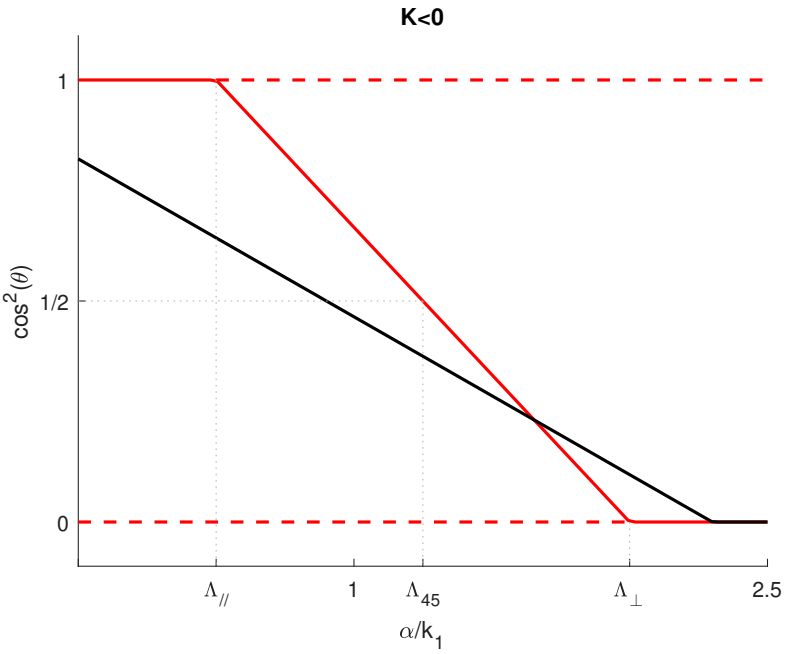

Figure 2.4. The $\cos^2(\theta)$ function depending on the ratio $\Lambda = \frac{\alpha}{k_1}$ for values $K < 0$. The solid line (red) describes a stable configuration, while the dashed red line describes an unstable one. The solid black line depicts the case with a bifurcation parameter $\Lambda_{\|} \leq 0$, as in [15].

Similar considerations follow for the case $K > 0$. It holds that

$$\begin{aligned} \theta = 0 \quad &\text{stable} \iff \Lambda < \Lambda_{\|} = \frac{(2\tilde{G} - E_p)}{(E_z - E_p\nu_{zp})} \\ \theta = \frac{\pi}{2} \quad &\text{stable} \iff \Lambda > \Lambda_{\perp} = -\frac{(2\tilde{G} - E_z)}{(E_z - E_p\nu_{zp})} \\ \theta = \theta^* \quad &\text{stable} \iff \Lambda_{\|} > \Lambda > \Lambda_{\perp}. \end{aligned} \tag{2.55}$$

The condition $K > 0$ implies that the oblique configuration is always unstable. Therefore, the only possible configurations are the trivial ones. This result is shown in Figure 2.5.

It is interesting to compare these results with those obtained by Biton and Safran. In

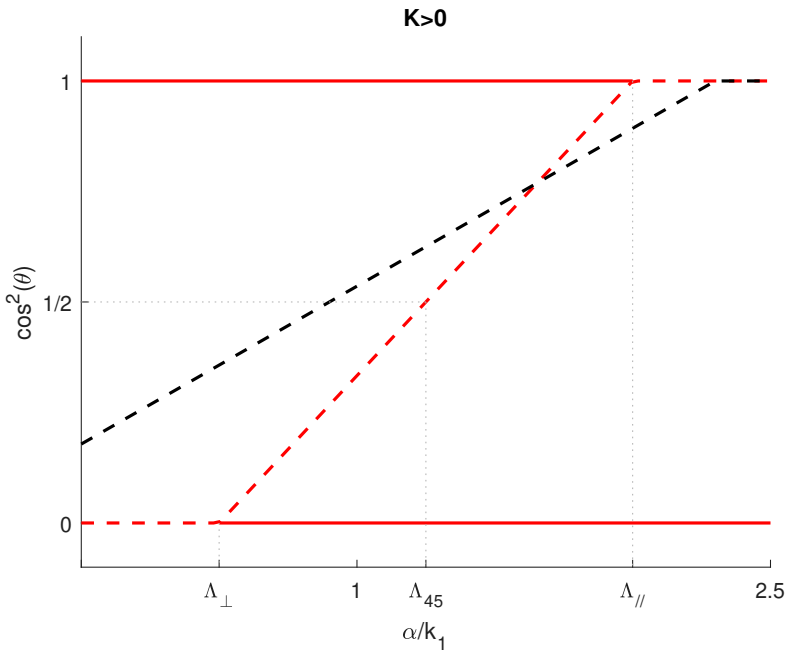

Figure 2.5. The $\cos^2(\theta)$ function depending on the ratio $\Lambda = \frac{\alpha}{k_1}$ for $K > 0$. The solid line (red) describes a stable configuration, while the dashed red line describes an unstable one. The black line depicts the case when $\Lambda_\perp < 0$. Notice that this behavior is the opposite of the one observed for $K < 0$ in Figure 2.4.

order to do so, we assume again that (2.14) holds, i.e.,

$$(1 - \nu_{zp}\nu_{pz})G_{zp} + \frac{1}{2}E_p\nu_{zp} = \frac{1}{2}E_p,$$
$$E_z = E_p + \tilde{E}_z \quad \text{where} \quad \tilde{E}_z > 0.$$

Notice that the first condition implies that the bifurcation configuration $\Lambda_\parallel = 0$. Moreover, the second hypothesis is a more general one and states that the material is reinforced in the fibers' directions.

$$\begin{aligned} 4\tilde{G} - E_p - E_z &= 2E_p - 2E_p - \tilde{E}_z = -\tilde{E}_z < 0, \\ k_1(2\tilde{G} - E_p) - \alpha E_Z(1 - \nu_{pz}) &= -\alpha E_z(1 - \nu_{pz}) > 0, \\ k_1(2\tilde{G} - E_z) + \alpha E_z(1 - \nu_{pz}) &= -k_1\tilde{E}_z + \alpha(\tilde{E}_z + E_p(1 - \nu_{zp})). \end{aligned} \tag{2.56}$$

Therefore, from the second inequality, we show that $\theta_0 = 0$ is always unstable. This is indeed the case described by the black line in figure 2.4 since it holds that $\Lambda_\parallel < 0$. Moreover, there are two other admissible cases to analyze, which depend on the sign of $-k_1\tilde{E}_z + \alpha(1 - \nu_{pz})$. Thus,

- $-k_1\tilde{E}_z + \alpha(1 - \nu_{pz}) > 0 \implies \theta^*$ exists and is stable, while θ_1 is unstable.

- $-k_1\tilde{E}_z + \alpha(1-\nu_{pz}) < 0 \implies \theta^*$ does not exist, while $\theta_1 = \frac{\pi}{2}$ is stable.

We conclude that there is a change of configuration when

$$-k_1\tilde{E}_z + \alpha(\tilde{E}_z + E_p(1-\nu_{zp})) = 0, \tag{2.57}$$

i.e., there exists a set of material parameters combined with values of k_1 and α that satisfy this equality, which can be classified as a set of critical values. A similar result is achieved in the Biton and Safran article, where it also appears that θ_0 is always unstable. Indeed, as concluded in their article, this configuration is reached only in the limit of large curvature. Moreover, the remaining possible configurations, i.e., the oblique one θ^* and the perpendicular one θ_1, and their stability depend on a similar set of parameters. This proves that the above framework is a generalization of the results achieved in [15].

2.3.4 Discussion

The model developed above, despite its limitations due to the kinematic hypotheses, intuitively describes some of the results discussed in Chapter 1. This model clearly indicates that there exists a competition between the contractility forces developed by the myosin-activated fibers of the cell and the mechanical stresses due to the bending over a curved substrate.

As highlighted previously in Chapter 1, the reorientation angle is cell-type dependent. This is accounted for in this model by the fact that the bifurcation points depend directly on the material coefficients. Indeed, we may state that fibroblasts show a much thicker network of stress fibers, hence resulting in a larger penalty to bending, which intuitively shifts the angle towards the direction of the axis of the cylinder. Our model predicts this behavior, as depicted in Figure 2.6. Indeed, for a fixed value of the ratio $\Lambda = \frac{\alpha}{k_1}$, the angle shifts towards the configuration $\theta = 0$ with the increasing elastic modulus E_z, hence explaining the orientation angles observed in [16]. As pointed out before with the comparison with results in [15], this parameter is correlated with the bending of the fibers.

On the other hand, epithelial cells might show a thinner network of fibers, hence lowering the penalty energy due to bending. This results in an orientation towards the orthogonal configuration, as experimentally observed in [12]. In fact, the bending of the cell cytoskeleton and fibers lowers the compression of the cell due to contractility.

However, this model works only for negative values of the curvature k_1. Besides the mathematical reasons for why this is true, it makes no physical sense that the same competition holds for positive values of k_1. In fact, this implies that the upper surface of the cell is compressed, while the lower one is stretched. Thus, the contractility of the cell will worsen the compression of the upper part of the cell, resulting in an increase in the stored elastic energy. This suggests that the optimal configuration is always the one oriented in the axial direction, but this is not true. Indeed, the study conducted by [28] showed that airway smooth muscle cells reorient along the maximum curvature direction on surfaces with positive k_1 values. Therefore, there are other contributions to cell mechanics to consider in order to explain these results, hence we will not even try to use this model in the latter case.

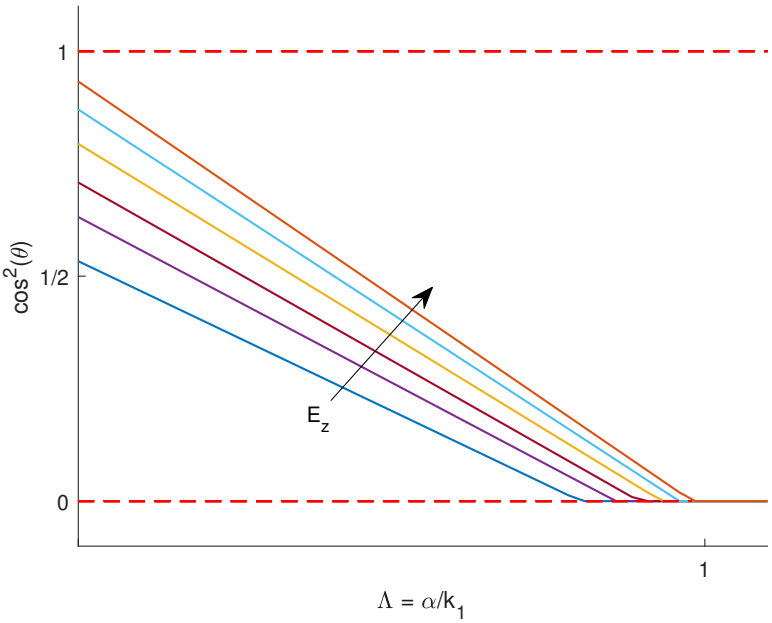

Figure 2.6. The $\cos^2(\theta)$ function depending on the ratio $\Lambda = \frac{\alpha}{k_1}$ for $K < 0$ and $\Lambda_{\parallel} < 0$. The figure shows that both the slope and the bifurcation point $\Lambda_{\perp}$ increase as E_z increases.

Chapter 3

Reorientation on an inflated cylinder

In this chapter, we examine the phenomenon of cellular reorientation in response to mechanical deformation, focusing specifically on the inflation of a cylindrical substrate. Understanding this behavior is crucial for applications in biomedical engineering, such as designing vascular grafts and other tubular constructs where cells encounter curved geometries. The first section defines the kinematics of cylinder inflation, which involves understanding how cylindrical substrates deform under various internal pressures. This section covers the fundamental principles of cylinder inflation, including the assumptions of material incompressibility and the derivation of the principal stretches in radial, azimuthal, and axial directions. These equations form the backbone of our theoretical framework, allowing us to predict how substrate deformation influences cellular orientation. Following the foundational kinematics, Sections 2 and 3 explore the cellular response to isotropic and anisotropic mechanical environments, respectively. Building on the theoretical framework and the findings of Ogden and Holzapfel [1,2], these sections investigate how different mechanical setups and the choice of the strain-energy function influence the mechanical response of the inflated tube, examining both theoretical models and experimental observations [40]. Additionally, beyond existing literature results, the orthotropic model is investigated in accordance with research on cell structure [23]. Finally, Section 4 is dedicated to analyzing orthogonal families of fibers within the cylindrical structure and their remodeling in response to varying internal pressures. This analysis provides insights into the optimal configurations that minimize the energy states of the system. By understanding these configurations, we can better predict and control how cells adapt their orientation in response to mechanical cues.

3.1 Kynematics of cylinder inflation

Consider a thick-walled circular cylindrical tube. In a reference configuration $\mathscr{B}_0$, in cylindrical coordinates a point (R, Θ, Z) of this geometry is described by

$$A \leq R \leq B, \quad 0 \leq \Theta \leq 2\pi, \quad 0 \leq Z \leq L$$

where A, B, and L are positive constants describing the inner radius, the outer radius, and the length of the tube, respectively.

In the following, we will assume that the shape of the tube is maintained and that the material composing the tube is incompressible. Therefore, we are allowed to write

$$r = r(R), \quad \theta = \Theta, \quad z = \lambda_l Z$$

where (r, θ, z) are the deformed coordinates in the actual configuration $\mathscr{C}$. In particular, the assumption that the shape of the tube is maintained implies that r depends only on the coordinate R, θ remains unchanged, and z is stretched along its direction by a factor of λ_l.

The principal stretches λ_1, λ_2, λ_3 along the radial, azimuthal, and the axial direction are written as:

$$\lambda_1(R) = \frac{dr}{dR}(R), \quad \lambda_2(R) = \frac{r(R)}{R}, \quad \lambda_3 = \lambda_l.$$

The incompressibility constraint reads as

$$\det \mathbb{F} = \lambda_1 \lambda_2 \lambda_3 = \frac{dr}{dR}(R) \frac{r(R)}{R} \lambda_l = 1 \tag{3.1}$$

Therefore, let $a = r(A)$ and $b = r(B)$ be respectively the inner and outer radius of the tube after the deformation. An integration of the incompressibility constraint leads to

$$r(R)^2 - a^2 = \lambda_3^{-1}(R^2 - A^2), \quad \theta = \Theta, \quad z = \lambda_l Z. \tag{3.2}$$

Notice that Equation (3.2) may be seen as a relationship between the deformed outer radius $b = r(B)$ and the deformation a and λ_l. In a more fascinating way, if we define $\lambda_b = \frac{b}{B}$ and $\lambda_a = \frac{a}{A}$ as the stretch of the inner and outer radius, an evaluation of the earlier equation for $R = B$ leads to

$$b^2 = r(B)^2 = a^2 + \lambda_l^{-1}(B^2 - A^2) \implies \lambda_l \lambda_b^2 - 1 = \frac{A^2}{B^2}(\lambda_l \lambda_a^2 - 1). \tag{3.3}$$

Thus, for given λ_l and a given ratio $\frac{A}{B}$, it follows that λ_b depends on λ_a. Moreover, introducing $\lambda = \lambda_2 = \frac{r}{R}$, the same argument leads to

$$\lambda_l \lambda_b^2 - 1 = \frac{A^2}{R^2}(\lambda_l \lambda^2 - 1) = \frac{A^2}{B^2}(\lambda_l \lambda_a^2 - 1) \tag{3.4}$$

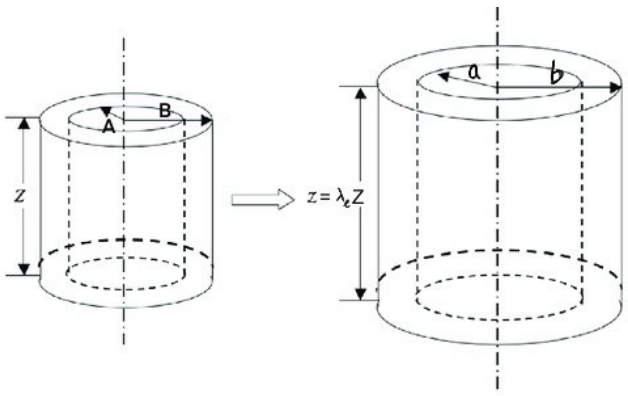

Figure 3.1. Schematic representation of the case of inflation of a cylinder.

Therefore, for a fixed value of λ_l, during the inflation of the tube it holds

$$\lambda^2 \lambda_l \geq 1, \quad \lambda_a \geq \lambda \geq \lambda_b$$

with equality if and only if the deformation is isochoric, i.e. $\lambda = \lambda_l^{-\frac{1}{2}}$ for $A \leq R \leq B$.

The strain energy density may be described as a function of the independent stretches $\lambda_2 = \lambda$ and $\lambda_3 = \lambda_l$ so that

$$\hat{W}(\lambda, \lambda_l) = W(\lambda^{-1}\lambda_l^{-1}, \lambda, \lambda_l)$$

where the radial stretch depends on λ_l and λ due to the incompressibility constraint. Therefore, the response functions associated with the strain energy W are given by

$$\sigma_i = \lambda_i \frac{\partial W}{\partial \lambda_i} - p$$

where σ_i are the principal Cauchy stresses and p is an unknown pressure introduced as the Lagrange multiplier relative to the incompressibility of the material. By means of the chain rule of differentiation, it follows directly from the strain energy equation that

$$\frac{\partial \hat{W}}{\partial \lambda} = -\frac{\partial W}{\partial \lambda_1}\lambda_1 \lambda^{-1} + \frac{\partial W}{\partial \lambda},$$
$$\frac{\partial \hat{W}}{\partial \lambda_l} = -\frac{\partial W}{\partial \lambda_1}\lambda_1 \lambda_l^{-1} + \frac{\partial W}{\partial \lambda_l}.$$

Therefore, the pressure p can be eliminated from the principal Cauchy stress equations, leading to the pair of equations:

$$\sigma_2 - \sigma_1 = \lambda \frac{\partial \hat{W}}{\partial \lambda}, \quad \sigma_3 - \sigma_1 = \lambda_l \frac{\partial \hat{W}}{\partial \lambda_l}. \tag{3.5}$$

In order to close the system, we need to introduce the equilibrium equations of the body. When there is no time dependence and no external forces, the equilibrium equations reduce to

$$\operatorname{div} \sigma = 0$$

which, for our particular geometrical choice and the dependence only on the independent coordinate R, reduces the equilibrium in the longitudinal direction to the single scalar equation in cylindrical coordinates:

$$\frac{d\sigma_{rr}}{dr} + \frac{1}{r}(\sigma_{rr} - \sigma_{\theta\theta}) = 0$$

where $\sigma_{rr} = \sigma_1$ and $\sigma_{\theta\theta} = \sigma_2$. This is solved in conjunction with the boundary conditions:

$$\sigma_{rr} = \begin{cases} -P & \text{for} \quad R = A \\ 0 & \text{for} \quad R = B \end{cases}$$

This boundary condition corresponds to the application of an internal pressure $P \geq 0$ and zero traction outside.

The relationship between the stretch of the inner radius λ_a and the internal pressure P can be computed directly by an integration of the equilibrium equation over the thickness of the deformed tube. This process may be carried out by a change of the independent variable from r to λ by means of the earlier relationships. Indeed, it holds that

$$R(r) = \sqrt{\lambda_l(r^2 - a^2) + A^2}, \quad \lambda(r) = \frac{r}{R(r)}, \quad \frac{\partial \lambda}{\partial r}(r) = \frac{R(r)^2 - \lambda_l r^2}{R(r)^3}.$$

Therefore, the integration of the equilibrium equation upon a change of variable leads to

$$P = \int_{\lambda_b}^{\lambda_a} (\lambda^2 \lambda_l - 1)^{-1} \frac{\partial \hat{W}}{\partial \lambda}(\lambda, \lambda_l)\, d\lambda. \tag{3.6}$$

This equation provides the pressure P as a function of the inner stretch λ_a for given values of the ratio $\frac{B}{A}$ and axial stretch λ_l, given that λ_b depends on λ_a. Notice that, to maintain a fixed stretch, an axial load N must be applied, its expression can be computed analytically from the axial equilibrium and is given by

$$\frac{N}{\pi A^2} = (\lambda_a^2 \lambda_z - 1) \int_{\lambda_b}^{\lambda_a} (\lambda^2 \lambda_l - 1)^{-2} \left(2\lambda_l \frac{\partial \hat{W}}{\partial \lambda_l} - \lambda \frac{\partial \hat{W}}{\partial \lambda} \right) \lambda\, d\lambda + P\lambda_a^2 \tag{3.7}$$

where we assumed that the tube ends are closed so that the pressure contributes to the axial load. In order to separate the contribution of the pressure, we are able to define the *reduced force* F applied at the end of the tube as

$$\frac{F}{\pi A^2} = \frac{N}{\pi A^2} - P\lambda^2 = (\lambda_a^2 \lambda_z - 1) \int_{\lambda_b}^{\lambda_a} (\lambda^2 \lambda_l - 1)^{-2} \left(2\lambda_l \frac{\partial \hat{W}}{\partial \lambda_l} - \lambda \frac{\partial \hat{W}}{\partial \lambda} \right) \lambda\, d\lambda. \tag{3.8}$$

The expressions of the reduced force F (3.8) and of the pressure P (3.6) allow us to reproduce the experimental setup in [40] for different given initial axial stretch λ_l

3.2 Isotropic response

In the following, we will assume that the material is isotropic. In particular, we will use the classical Neo-Hookean constitutive law for the strain-energy function in the case of incompressible material:

$$W(\mathbb{F}) = \frac{\mu}{2}\left(\mathrm{tr}(\mathbb{F}^T\mathbb{F}) - 3\right)$$

which, in our case, is simplified to

$$\hat{W}(\lambda, \lambda_l) = \frac{\mu}{2}\left(\lambda^2 + \lambda_l^2 + \lambda^{-2}\lambda_l^{-2} - 3\right) \tag{3.9}$$

Notice that this is a special case of the class of energy functions used in Ogden [1]:

$$\hat{W}(\lambda, \lambda_l) = \frac{2\mu}{n^2}\left(\lambda^n + \lambda_l^n + \lambda^{-n}\lambda_l^{-n}\right) \tag{3.10}$$

where the Neo-Hookean strain-energy function is recovered for $n = 2$.

The pressure P thus follows

$$P^* = \frac{P}{\mu} = \int_{\lambda_b}^{\lambda_a} (\lambda^2\lambda_l - 1)^{-1}\left(\lambda - \lambda_l^{-2}\lambda^{-3}\right) d\lambda.$$

The nondimensional relationship between $P^* = P/\mu$ and λ_a is shown in Figure 3.2. The function P^* is depicted for a set of values of the wall thickness, specifically choosing $\frac{A^2}{B^2} \in \{0.4, 0.63, 0.77, 0.85\}$. The axial stretch is fixed to $\lambda_z = 1.2$. The main feature to highlight is the increasing stiffness of the material associated with increasing wall thickness. This result is in contrast with typical rubber-like materials, where there exists a non-unique relation between P^* and λ_a because the function is non-monotonic. Moreover, notice that the classical Neo-Hookean relation leads to a concave pressure function, as shown in Figure 3.2 (a), in contrast with the one chosen in [1] for $n = 24$ shown in Figure 3.2(b). In particular, the latter fits better the in-vitro experimental results, where the internal pressure P behaves as if it approaches infinity for $\lambda_a = 1.2$ rather than the result in Figure 3.2(a). Nonetheless, the model presented here qualitatively explains the stiffening with the wall thickness and axial load, some of the relevant features of soft tissues.

3.3 Anisotropic Response

3.3.1 Mechanical Setup [1]

The deformation analyzed in Section 3.1 is *locally* a purely homogeneous strain. Therefore, the results can be extended to the anisotropic case by introducing the anisotropic material

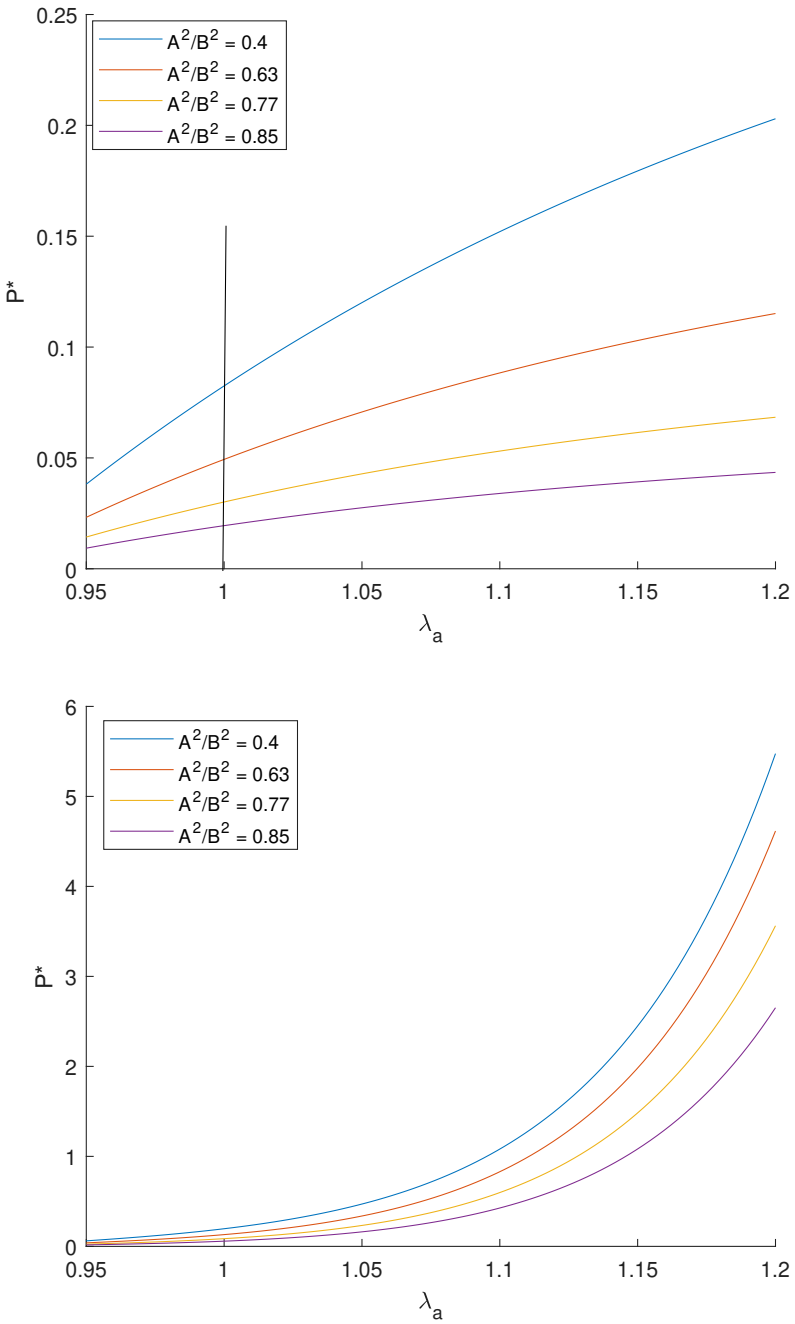

Figure 3.2. Plot of the dimensionless pressure P^* as a function of λ_a for different values of wall thickness and constant axial stretch $\lambda_l = 1.2$. (a) classical Neo-Hookean material (b) Incompressible strain energy function for $n = 24$ (3.10).

properties characterized by the fiber directions $\mathbf{N}$ and $\mathbf{N}^{\perp}$ *locally* in the tangent plane (Θ, Z), where $\mathbf{N}^{\perp}$ is locally orthogonal to $\mathbf{N}$. Consequently, the principal directions of strain align with the axes of the cylindrical coordinate system. The energy-strain function $\hat{W}$ will directly depend on the angle φ describing both fiber directions.

To simulate some results, we use the general Neo-Hookean strain-energy function for orthotropic materials:

$$W(\mathbb{F}) = \frac{\mu}{2}(\mathrm{tr}(\mathbb{C}) - 3) + \frac{\alpha_1}{4}(\mathbb{C} : \mathbb{A} - 1)^2 + \frac{\alpha_2}{4}(\mathbb{C} : \mathbb{A}^{\perp} - 1)^2 \tag{3.11}$$

where $\mathbb{A} = \mathbf{N} \otimes \mathbf{N}$ and $\mathbb{A}^{\perp} = \mathbf{N}^{\perp} \otimes \mathbf{N}^{\perp}$ are the structural tensors describing the material anisotropy. Notice that this particular choice of the strain-energy function is an approximation of the one used in Holzapfel et al. [2], which is written in exponential form resembling a Fung-type strain energy:

$$\begin{aligned} W(I_1, I_2, I_4, I_6) = \frac{c_1}{2}(I_1 - 3) + \frac{c_2}{2}(I_2 - 3) \\ + \frac{k_1}{2k_2}\left(\exp[k_2(I_4 - 1)^2] - 1\right) + \frac{k_1}{2k_2}\left(\exp[k_2(I_6 - 1)^2] - 1\right) \end{aligned} \tag{3.12}$$

where $I_4 = \mathbb{C} : \mathbb{A}$ and $I_6 = \mathbb{C} : \mathbb{A}^{\perp}$ are the anisotropic invariants related to the directions $\mathbf{N}$ and $\mathbf{N}^{\perp}$. Observe that the second-order approximation of this strain energy coincides, apart from some adjustment of the notation, with the strain-energy used here.

The equation of the internal pressure P is *formally* the same, with the exception that the strain-energy function now depends on the angle φ:

$$P = \int_{\lambda_a}^{\lambda_b} (\lambda^2 \lambda_l - 1)^{-1} \frac{\partial \hat{W}}{\partial \lambda}(\lambda, \lambda_l, \varphi)\, d\lambda.$$

To illustrate some results, Ogden [1] employs a generalization of the isotropic Neo-Hookean strain-energy function and energy-strain function:

$$\begin{aligned} \hat{W}(\lambda, \lambda_l, \varphi) = \frac{1}{n}\left[\mu_1(\varphi)(\lambda^n - 1 - n\ln(\lambda)) + \mu_2(\varphi)(\lambda_l^n - 1 - n\ln(\lambda_l))\right. \\ \left. + \mu_3(\lambda^{-n}\lambda_l^{-2} - 1 + n\ln(\lambda\lambda_l))\right] \end{aligned} \tag{3.13}$$

where μ_3 is a material constant and $\mu_1(\varphi)$ and $\mu_2(\varphi)$ are material parameters depending on the angle φ. This strain-energy function accounts for anisotropy only through the material coefficients μ_1 and μ_2, while the one employed in [2] and adopted in this work explicitly depends on the relation between the deformation and the structure tensors of the material $\mathbb{A}$ and $\mathbb{A}^{\perp}$.

The analysis of the isotropic response in Section 3.2 showed that the *qualitative* behavior of the material does not depend on the wall thickness. Therefore, the analysis can be reduced to the membrane approximation. This can be achieved by using $\epsilon = \frac{H}{A} = \frac{B-A}{A}$ as an expansion parameter, where the thickness in the reference configuration is $H = B - A$.

Indeed, it can be shown that

$$\lambda_a - \lambda_b = [\lambda_a - \lambda_l^{-1}\lambda_a^{-1}]\epsilon + o(\epsilon) \quad \text{for} \quad \epsilon \to 0$$

which implies, by means of the mean value theorem for integrals, that:

$$P = \epsilon\lambda^{-1}\lambda_l^{-1}\frac{\partial \hat{W}}{\partial \lambda}(\lambda, \lambda_l, \varphi) \tag{3.14}$$

where λ is any value of the azimuthal stretch through the wall. This simplified expression for P allows us to derive the analytical form given the energy strain function $\hat{W}$. Figure 3.3 shows the dimensionless pressure P^* against the azimuthal stretch λ for different material parameters for (a) the energy function of type (3.11) and (b) the energy function of type (3.13). Notice that the graph intersects the pressure axis $P^* = 0$ at different values of the stretch λ depending on the material coefficients. As observed in the isotropic case, the only difference between the two types of response is observed in the sign of the second derivative of the function. Moreover, here we again assumed that the axial stretch λ_l is maintained constant during inflation, i.e., there should be an axial load to achieve that. In particular, the membrane counterpart of the axial load equation (3.7) is given by:

$$\frac{F}{\pi A^2} = \frac{N}{\pi A^2} - P\lambda^2 = \epsilon\left[2\frac{\partial \hat{W}}{\partial \lambda_l}(\lambda, \lambda_l, \varphi) - \lambda\lambda_l^{-1}\frac{\partial \hat{W}}{\partial \lambda}(\lambda, \lambda_l, \varphi)\right] \tag{3.15}$$

where F can be interpreted as a *reduced force* applied to the end of the tube. This mechanical framework, however, does not account for some other interesting features due to the fact that λ_z is fixed to a value. Another approach is the one adopted in Holzapfel et al. [2], which we discuss next.

3.3.2 Mechanical Setup in [2]

To highlight other interesting features characterizing the inflation of a cylindrical tube, it is useful to consider a slightly different experimental setup. Specifically, we assume that the *reduced force* F (3.15) at the end of the tube is zero [2], implying that

$$N = \pi a^2 P, \quad \left[2\frac{\partial \hat{W}}{\partial \lambda_l}(\lambda, \lambda_l, \varphi) - \lambda\lambda_l^{-1}\frac{\partial \hat{W}}{\partial \lambda}(\lambda, \lambda_l, \varphi)\right] = 0. \tag{3.16}$$

Thus, $N = \pi a^2 P$ is the sole contribution to the axial load. Notice that the axial load N does not directly depend on the axial stretch λ_l as in (3.7), so λ_l is not fixed. The 2D approximation is described by two geometrical features of the problem: the middle radius $R = (A + B)/2$ and the thickness of the tube $H = B - A$. The equilibrium equations in the axial and circumferential directions are formulated as:

$$\begin{aligned} \sigma_3 - \frac{N}{2\pi r h} &= \sigma_3 - \frac{a^2}{2hr}P = 0 \\ \sigma_2 - \frac{N}{\pi a h} &= \sigma_2 - \frac{a}{h}P = 0 \end{aligned} \tag{3.17}$$

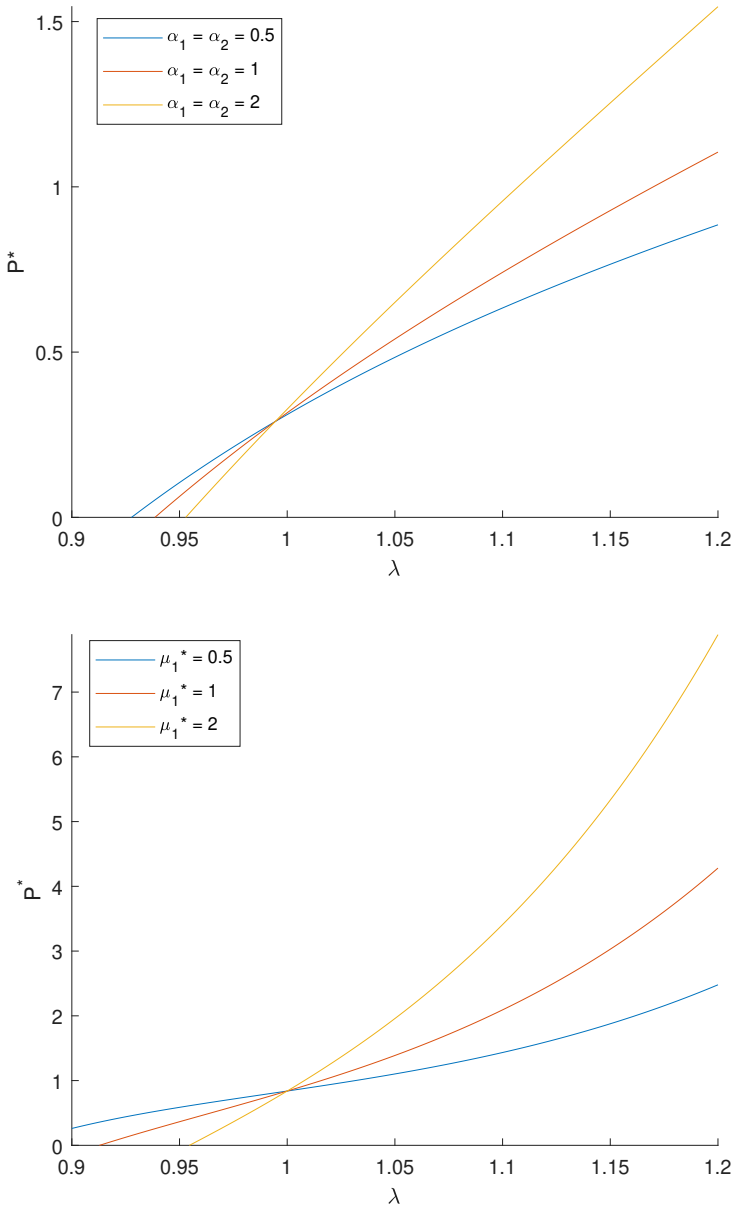

Figure 3.3. Plot of the dimensionless pressure P^* as a function of the azimuthal stretch λ in the membrane limit. (a) Neo-Hookian anisotropic material described by the energy function for different values of the material coefficients α_1 and α_2. (b) Incompressible strain energy function for $n = 10$ and $\mu_1^* = \frac{\mu_1}{\mu_3} = 0.5, 1, 2$.

where r, a, h are the deformed middle radius, inner radius, and thickness, respectively. These are computed as

$$h = \lambda_1 H = \lambda^{-1}\lambda_l^{-1} H, \quad r = \lambda R, \quad a = r - \frac{h}{2} = \lambda R - \frac{H}{2\lambda\lambda_l}. \tag{3.18}$$

Finally, these identities and equations (3.5) allow us to explicitly write the equilibrium equations (3.17) as

$$\begin{aligned} \lambda \frac{\partial \hat{W}}{\partial \lambda}(\lambda, \lambda_l, \varphi) - \left(\frac{\lambda^2 \lambda_l R}{H} - \frac{1}{2} \right) P = 0 \\ \lambda_l \frac{\partial \hat{W}}{\partial \lambda_l}(\lambda, \lambda_l, \varphi) - \frac{\lambda_l (\lambda R - \lambda^{-1}\lambda_l^{-1} H/2)^2}{2HR} P = 0 \end{aligned} \tag{3.19}$$

where $\hat{W}$ depends on the strain energy function used. Notice that this system of equations is equivalent to the solution derived from the pair of equations (3.14) and (3.15). Indeed, the equilibrium in the circumferential direction (3.5) may also be formulated as, for $\epsilon = H/R$,

$$\begin{aligned} P &= \epsilon \left(\lambda^2 \lambda_l - \frac{\epsilon}{2} \right)^2 \lambda \frac{\partial \hat{W}}{\partial \lambda} \\ &= \epsilon \lambda^{-1} \lambda_l^{-1} \left(1 + \lambda^{-2} \lambda_l^{-1} \frac{\epsilon}{2} + o(\epsilon^2) \right) \frac{\partial \hat{W}}{\partial \lambda} \\ &= \epsilon \lambda^{-1} \lambda_l^{-1} \frac{\partial \hat{W}}{\partial \lambda} + o(\epsilon) \quad \text{for} \quad \epsilon \to 0 \end{aligned} \tag{3.20}$$

which is equivalent to the membrane approximation used by Ogden [1]. Moreover, the axial equilibrium (3.5) may also be formulated as

$$\begin{aligned} \frac{\lambda_l}{2} \left[2 \frac{\partial \hat{W}}{\partial \lambda_l} - \frac{1}{\epsilon} (\lambda - \frac{1}{2} \lambda_l^{-1} \lambda^{-1} \epsilon)^2 P \right] = 0 \\ 2 \frac{\partial \hat{W}}{\partial \lambda_l} - \frac{1}{\epsilon} (\lambda^2 + O(\epsilon)) P = 0 \\ 2 \frac{\partial \hat{W}}{\partial \lambda_l} - \lambda \lambda_l^{-1} \frac{\partial \hat{W}}{\partial \lambda} = 0 \end{aligned} \tag{3.21}$$

which coincides with the condition of zero reduced force (3.16). This underlines that the only difference between these setups lies in the choice of the constitutive relations and the absence of reduced load.

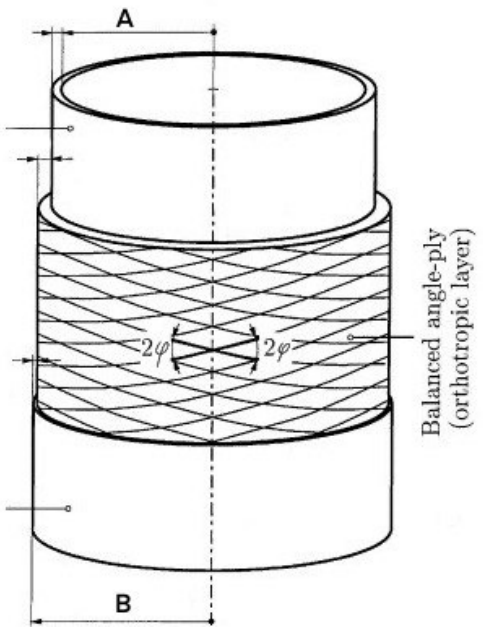

Figure 3.4. Fiber-reinforced orthotropic tube with double-helically arranged fibers [2].

The authors describe the anisotropy of the tube using two families of fibers $\mathbf{N}$ and $\mathbf{N}^{\perp}$ such that both families form an angle φ with the longitudinal direction (angle-ply type, see Figure 3.4). This setup is modeled by using the two families of fibers

$$\mathbf{N} = \begin{bmatrix} 0 \\ \cos(\varphi) \\ \sin(\varphi) \end{bmatrix}, \quad \mathbf{N}^{\perp} = \begin{bmatrix} 0 \\ -\cos(\varphi) \\ \sin(\varphi) \end{bmatrix} \tag{3.22}$$

where θ is the angle between the fibers and the azimuthal direction e_θ. Thus, the stretches along both families' directions are the same, hence

$$I_4 = \mathbb{C} : \mathbb{A} = \mathbb{C} : \mathbb{A}^{\perp} = I_6. \tag{3.23}$$

For our purposes, the expression of $\hat{W}$ may be computed directly from the strain-energy function (3.11):

$$\begin{aligned} \hat{W}(\lambda, \lambda_l, \varphi) = W(\mathbb{F}) = \frac{\mu}{2}(\lambda^2 + \lambda_l^2 + \lambda^{-2}\lambda_l^{-2}) + \\ + \frac{\alpha_1 + \alpha_2}{4}(\lambda^2 \cos(\varphi)^2 + \lambda_l^2 \sin(\varphi)^2 - 1)^2. \end{aligned} \tag{3.24}$$

The membrane solution of the system (3.19) is depicted in Figures 3.5 and 3.6 for different values of the pressure P. These results are computed by choosing the geometrical parameters $R = 109$ mm and $H = 1.8$ mm, and the material parameters $\mu = 260.4$ kPa,

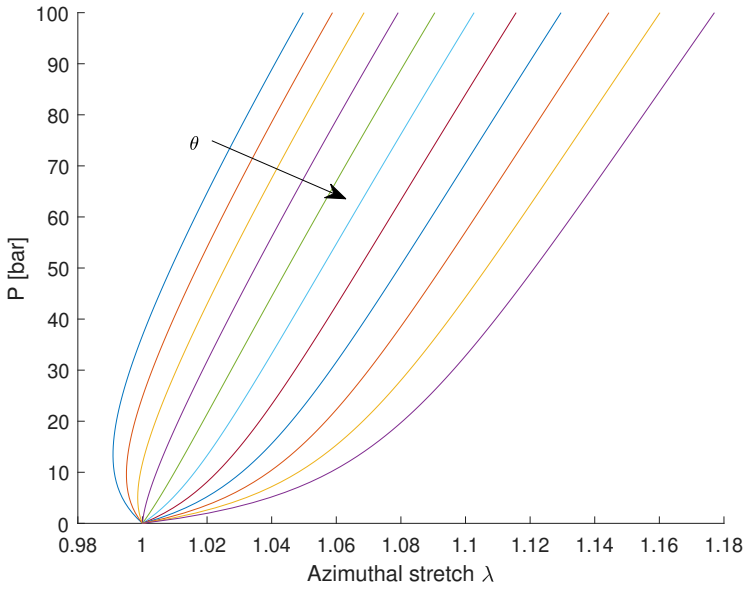

Figure 3.5. Inflation of a cylinder tube with fiber angles θ between 30° and 40∘. Membrane solution of λ for different values of the internal pressure P.

$\alpha_1 = \alpha_2 = 23.1 \times 10^3$ kPa, mechanically equivalent to the parameters used in [2], and angle θ between 30° and 40°. The results are formally equivalent to those achieved using the exponential energy-function type (3.12). It is evident that the response strongly depends on the orientation angle θ of the fiber families. Even though the variation of the fiber angle is only 10°, the mechanical behavior is remarkably different. Fiber angles higher than $\theta \approx 34°$ show a decrease in the axial stretch λ_l in the lower pressure domain, leading to a shortening of the tube since $\lambda_l < 1$. Then, there exists a turning point where the stretch becomes monotonically increasing with the pressure P. This effect, called the *inversion effect*, reflects the actual inversion seen in experiments for the pressure-axial stretch function, as in [41]. This inversion effect may also appear for the pressure-λ relation, whereas for angles lower than $\theta \approx 32°$, confirming the results in [2]. However, this effect is not validated by experimental results on arteries, where the azimuthal stretch λ behaves as a monotonic function of the internal pressure P.

3.3.3 Orthogonal Families of Fibers

The symmetrical arrangement of fibers, known as angle-ply, is commonly used to describe the response of the collagen structure in inflated arteries during experiments in academic research. Nonetheless, here we want to analyze also the case where the two families of fibers are related by orthogonality. A confluent monolayer of cells on a convex cylindrical surface tends to align the fibers in a preferred direction, forming an angle φ with the circumferential direction of the cylinder. Therefore, if we follow the common model of cell

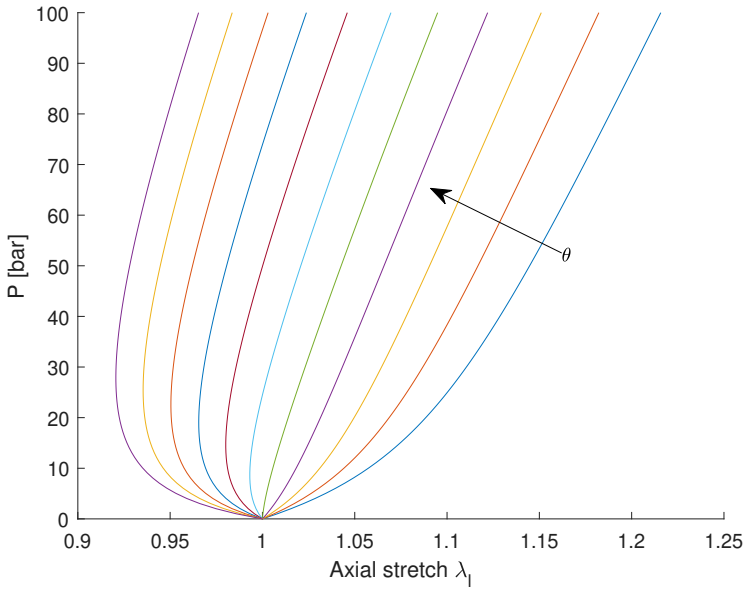

Figure 3.6. Inflation of a cylinder tube with fiber angles θ between 30° and 40°. Membrane solution of λ_l for different values of the internal pressure P.

as an orthotropic material with two mutually orthogonal families of fibers, the response of the monolayer can be assumed orthotropic locally, hence with the fibers arranged as follows:

$$\mathbf{N} = \begin{bmatrix} 0 \\ \cos(\varphi) \\ \sin(\varphi) \end{bmatrix}, \quad \mathbf{N}^{\perp} = \begin{bmatrix} 0 \\ -\sin(\varphi) \\ \cos(\varphi) \end{bmatrix}$$

In this setup, different fibers experience different stretches depending on the angle φ, unlike in the balanced angle-ply setup where the deformation was the same for both fiber families. Assuming a strain-energy function of the type given in (3.11), we have:

$$\begin{aligned} \hat{W}(\lambda, \lambda_l, \varphi) = W(\mathbb{F}) = \frac{\mu}{2}(\lambda^2 + \lambda_l^2 + \lambda^{-2}\lambda_l^{-2}) + \\ + \frac{\alpha_1}{4}(\lambda^2 \cos(\varphi)^2 + \lambda_l^2 \sin(\varphi)^2 - 1)^2 + \\ + \frac{\alpha_2}{4}(\lambda^2 \sin(\varphi)^2 + \lambda_l^2 \cos(\varphi)^2 - 1)^2 \end{aligned} \tag{3.25}$$

The solution of the system (3.5) is depicted in Figure 3.7 for λ and Figure 3.8 for λ_l, for angles φ between 0° and 40°, using the same set of material parameters μ, α_1, α_2. As before, the mechanical response varies significantly for different angles φ. The range of values reached by the principal stretch is slightly different from the previous case using

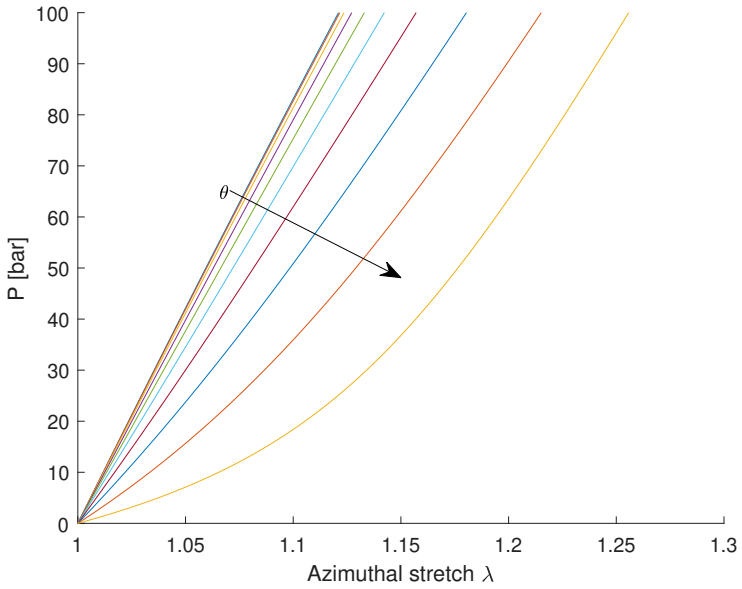

Figure 3.7. Inflation of a cylindrical tube with fiber angles φ between 0° and 40°. Membrane solution for λ at different internal pressures P.

(3.12). However, the main difference lies in the *inversion effect*. Figure 3.7 shows that λ does not exhibit this property for any values of φ, unlike in the balanced angle-ply setup. Instead, a limiting function is achieved for small angles φ. On the other hand, the pressure-axial stretch relation still exhibits the inversion effect for angles φ greater than a certain value. This difference in behavior may be significant because experimental data on arteries exhibit the inversion effect only in the axial stretch-pressure relation, while the circumferential stretch λ only stiffens.

In conclusion, these results validate the strain-energy function (3.11) as a candidate for describing the inflation of a tube made of biological tissue. Both the isotropic and anisotropic responses exhibit similar behaviors to those proposed in [1] and [2], showing qualitatively the same main features. Both the stiffening with the axial stretch, as depicted in Figure 3.2, and the inversion effect in Figure 3.6 are predicted by the membrane approximation of the problem. Moreover, in the context of remodeling, the stability analysis of an exponential energy-strain function (3.12) is formally identical to the polynomial form (3.11) chosen here. Thus, in the following, we will analyze the optimal arrangement of fibers that minimize the stored elastic energy in both the case of incremental pressure and the case of controlled deformation.

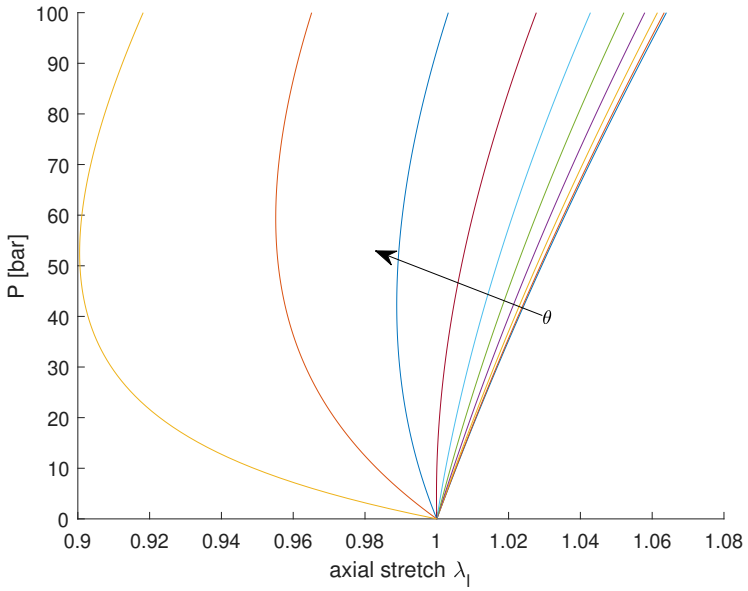

Figure 3.8. Inflation of a cylindrical tube with fiber angles φ between 0° and 40°. Membrane solution for λ_l at different internal pressures P.

3.4 Remodeling on an Inflated Cylinder

Several studies have shown that cells reorganize their cytoskeletal structure under stretching along two directions. This phenomenon was first observed by Buck in his studies on blood vessels [3,4], where cells are periodically stretched due to internal variations in blood pressure. This has been extensively studied in the literature, with several theoretical explanations proposed in recent years [9]. The most successful approach is based on elastic energy, where cells reorient their stress fibers to minimize the strain-energy function. A theoretical model that successfully explains the main features of SF reorganization under large strains was proposed by Lucci and Preziosi [23]. They used a strain-energy function of the general polynomial form:

$$\mathscr{U}(\mathbf{I}) = \frac{1}{2}\mathbf{I}\cdot\mathbb{K}\mathbf{I} + \mathscr{V}, \tag{3.26}$$

where $\mathbf{I} := (\hat{I}_4, \hat{I}_5, \hat{I}_6, \hat{I}_7, I_8)$, $\mathbb{K}$ is the symmetric matrix of coefficients, and $\mathscr{V}$ is the purely isotropic part of the elastic energy. The anisotropic invariants $\mathbf{I}$ are:

$$\begin{aligned} &\hat{I}_4 = \mathbb{C} : \mathbb{A} - 1, \quad \hat{I}_5 = \mathbb{C}^2 : \mathbb{A} - 1, \\ &\hat{I}_6 = \mathbb{C} : \mathbb{A}' - 1, \quad \hat{I}_7 = \mathbb{C}^2 : \mathbb{A}' - 1, \\ &I_8 = \mathbf{N}' \cdot (\mathbb{C}\mathbf{N}), \end{aligned} \tag{3.27}$$

where $\mathbf{N}$ and $\mathbf{N}'$ are the directions of the two families of fibers, while $\mathbb{A} = \mathbf{N} \times \mathbf{N}$ and $\mathbb{A}' = \mathbf{N}' \times \mathbf{N}'$ are the structural tensors associated with the fiber directions.

In a controlled deformation framework, where the principal stretches λ and λ_l are controlled externally, the analysis by Lucci and Preziosi [23] holds locally. Therefore, we can analyze the optimal configuration of the SFs for different values of the deformed radius r (i.e., for different values of λ) and draw conclusions. Additionally, it might be interesting to analyze the minimal energy configuration for different values of internal pressure P in the cases studied before, as the mechanical setup is quite different.

3.4.1 Optimal Configurations in Controlled Deformation Setup

The mechanical framework used previously, although qualitatively explaining some main features of the inflation of biological tissue, does not allow for an analytical study of the optimal configurations of the stress fibers. Therefore, we will assume complete control over the principal stretches λ and λ_l. Notice that, even though we are working in a cylindrical coordinate system, the analysis by Lucci and Preziosi [23] continues to hold *locally*.

In the following, we assume that the two families of fibers are locally orthogonal on the tube, as done in Section 3.3.3, where φ is the angle between $\mathbf{N}$ and the principal stretching direction. This constraint on the fiber families is chosen for two main reasons. Firstly, the possible scenarios regarding the stability of a configuration are broader than in the balanced angle-ply setup. The angle-ply setup allows us to factorize the anisotropy coefficient α_i into one coefficient, reducing the different scenarios in the bifurcation analysis. Secondly, the fiber families model the SFs cytoskeletal structure of the cell, which is usually modeled in this framework.

The analysis by Lucci and Preziosi [23] also holds for this setup, where the principal stretches are $\lambda^2 = \frac{r^2}{R^2}$ and λ_l^2 in the circumferential and axial directions, respectively. We will assume there is no contribution from $\mathbb{C}^2$ terms, neglecting the contributions from the invariants $\hat{I}_5$ and $\hat{I}_7$ by setting their associated parameters in the coefficient matrix $\mathbb{K}$ to zero. As noted by Lucci and Preziosi [23] and thoroughly examined by Merodio and Ogden [42], these terms are not necessary to characterize the behavior of an orthotropic material. Indeed, they can be expressed as a linear combination of the other invariants [42], so their contribution can be disregarded.

The analysis depends not only on the usual material parameters in W (3.26), but also on the direction of the main stretching direction. Therefore, we will separately analyze the case where $\lambda_l > \lambda$ and the symmetrical case $\lambda > \lambda_l$, drawing some conclusions.

Maximum (Main) Strain Direction along the axis

Let the axial direction be the main stretching direction, thus $\lambda_l > \lambda$ and $\lambda_l > 1$. The optimal configuration characterized by an angle φ falls into three possible cases: $\varphi = 0$ or $\varphi = \frac{\pi}{2}$ are the trivial ones, while, if it exists, an oblique configuration φ^* is the solution of [23]:

$$\cos^2(\varphi^*) = \frac{1}{2} + \frac{k_{44} - k_{66}}{k_{44} + k_{66} - 2k_{46} - k_{88}} \left(\frac{1}{2} - \frac{\lambda_l^2 - 1}{\lambda_l^2 - \lambda^2} \right). \tag{3.28}$$

Their stability depends, in general, on the material coefficients of $\mathbb{K}$. Notice that $\cos^2(\varphi)$ is in a linear relationship with the parameter:

$$\Lambda := \frac{\lambda_l^2 - 1}{\lambda_l^2 - \lambda^2}, \tag{3.29}$$

where the slope of the line is given by

$$\alpha = \frac{k_{44} + k_{66} - 2k_{46} - k_{88}}{k_{44} - k_{66}}. \tag{3.30}$$

We highlight the fact that $\Lambda = 1$ corresponds to maintaining the circumferential stretch $\lambda = 1$ fixed, while $\Lambda > 1$ corresponds to stretching in the circumferential direction while still maintaining $\lambda < \lambda_l$.

In this section, we analyze how the optimal configuration changes concerning a controlled deformed radius r, working directly with the circumferential stretch $\lambda = \frac{r}{R}$. The reorientation behavior will depend on the sign of $\lambda - 1$, as we will work with either $\Lambda < 1$ or $\Lambda > 1$ cases. To underline the dependence of Λ on the deformed radius r, we observe that:

$$\Lambda = \frac{\lambda_l^2 - 1}{\lambda_l^2 - \lambda^2} = \frac{R^2(\lambda_l^2 - 1)}{R^2\lambda_l^2 - r^2}, \tag{3.31}$$

where R is the undeformed radius in the reference configuration. Clearly, as the deformed radius r increases until it reaches the limit value $\lambda_l R$, the parameter Λ increases.

Figure 3.9 describes the angle φ against the deformed radius r for different values of $\alpha \in \{0.4, 0.6, 0.8, 1.2, 1.5, 2\}$. The computation is done by maintaining the axial stretch $\lambda_l = 1.3$ fixed and with an undeformed radius $R = 10mm$. Clearly, as the deformed radius increases, the angle tends to orient orthogonally to the axis of the cylinder. For smaller radii, however, the optimal angle shifts towards a stable oblique configuration. The parameter α, which only depends on the material coefficients, shifts the range of stability of the oblique configuration as it increases, while also increasing the optimal configuration angle for small deformed radii r.

This behavior is similar to what is observed for cells on curved substrata, where increasing the radius (and thus decreasing the curvature of the cylinder) results in configurations more aligned toward the circumferential direction, as highlighted in Chapter 1. However, this model does not account for any trade-off between curvature and contractility effects, as described in Chapter 2, since the orientation depends only on the material parameters of the tube. Indeed, this model does not consider cell-level interactions, as evidenced by the fact that reorientation is primarily characterized by the circumferential stretch λ, which omits information regarding the magnitudes of the undeformed and deformed radii R and r. To address this feature, it is necessary to introduce these effects in an alternative manner, as we will do in Chapter 4.

Main Strain Direction along the circumference

Contrary to the previous part, let the circumferential direction be the main stretching direction, thus $\lambda > \lambda_l$. Again, the optimal configuration is described by an angle φ, which

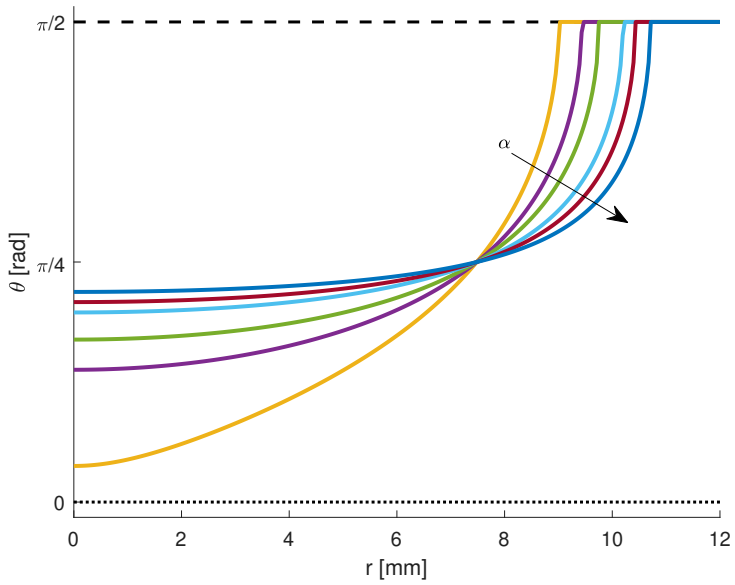

Figure 3.9. Bifurcation diagram of equilibrium angle in terms of deformed radius r for different $\alpha \in \{0.4, 0.6, 0.8, 1.2, 1.5, 2\}$. The values of the axial stretch and undeformed radius are set to $\lambda_l = 1.3$ and $R = 10$ mm, respectively. The solid lines describe stable configurations, while the dashed lines describe unstable configurations.

now describes the angle between the circumferential direction and the fiber direction $\mathbf{N}$. Hence, if it exists, the oblique configuration φ^* satisfies [23]:

$$\cos^2(\varphi^*) = \frac{1}{2} + \frac{k_{44} - k_{66}}{k_{44} + k_{66} - 2k_{46} - k_{88}} \left(\frac{1}{2} - \frac{\lambda^2 - 1}{\lambda^2 - \lambda_l^2} \right). \tag{3.32}$$

Their stability depends, in general, on the material coefficients of $\mathbb{K}$. The same considerations as above follow, except that now the angle φ is with respect to the azimuthal axis and the main stretch is such that the deformed radius must satisfy $r > R\lambda_l$.

To underline the dependence of Λ on the deformed radius r, we observe that:

$$\Lambda = \frac{\lambda^2 - 1}{\lambda^2 - \lambda_l^2} = \frac{r^2 - R^2}{r^2 - R^2\lambda_l^2}, \tag{3.33}$$

where R is the undeformed radius in the reference configuration. The parameter Λ is very large for radii r approaching the boundary value $R\lambda_l$, while it approaches 1 for very large undeformed radii.

Figure 3.10 describes the angle φ against the deformed radius r for different values of $\alpha \in \{0.8, 1.2, 1.5, 2, 3\}$. The computation is done by maintaining the axial stretch $\lambda_l = 0.8$ fixed and an undeformed radius $R = 10mm$. The figure shows that as the deformed radius increases, the optimal configuration angle φ shifts towards the direction of the cylinder

axis. Notice that, for values $\alpha < 1$ (yellow line), the orthogonal configuration becomes stable for sufficiently high radii, while it is reached only in the limit for small radii. The situation is opposite if $\lambda_l > 1$, as shown in Figure 3.10b, where $\lambda_l = 1.3$. In this case, for values $\alpha < 1$, the stable configuration is always the orthogonal one, hence the axial direction. This changes for values of $\alpha > 1$, where the optimal angle stabilizes on an oblique configuration that shifts very slowly towards 45° with respect to the circumferential direction. Notice that the deformed radius is limited below by the condition $\lambda > \lambda_l$. Therefore, we are unable to understand the behavior for smaller radii, and consequently, for very high curvature. Nonetheless, Figure 3.10a does not explain the reorientation observed in experiments, contrary to the case where the main direction was axial. As discussed earlier, we expect that as the radius increases—i.e., as curvature decreases—the optimal configuration angle should shift toward the circumferential direction, as observed in numerous experiments cited in Chapter 1 [14, 16].

3.4.2 Optimal Configurations for Different Values of Internal Pressure P

Although qualitatively understanding the reorientation process may be useful, the experimentally controlled setup does not fully describe the coupled deformation process described by (3.19) for a given internal pressure P. The internal pressure P controls the principal stretches λ and λ_l through the nonlinear system of equations (3.5). Therefore, for fixed values of P, the elastic energy reduces to a function of the configuration angle φ only, allowing us to analyze the minimal energy configuration through numerical solutions over the range of angle $\varphi \in [0, \frac{\pi}{2}]$. In the following, we will show solutions for different types of constitutive strain-energy choices.

Consider the setup with two families of symmetrically arranged fibers studied by Holzapfel et al. [2]—i.e., the balanced angle-ply setup described by the strain-energy function (3.24). Figure 3.11(a) shows the normalized strain energy function against the geometrical angle θ for different values of internal pressure P. Notice that below a certain threshold value of P, there exists an unstable oblique configuration while both parallel and orthogonal configurations are locally stable, as depicted by the blue and red solid lines. As the pressure increases, the oblique configuration disappears, and the only stable configuration is given by $\theta = 0$, hence parallel to the circumferential direction. Nonetheless, as observed before, the geometrical constraint between the two families of fibers highly influences the response of the tube. Indeed, the behavior for different angles for the strain-energy function (3.25) is depicted in Figure 3.11(b). Contrary to the angle-ply setup, we observe a remarkably unstable oblique configuration, while both the parallel and orthogonal configurations are stable.

Finally, it is worth noting that the introduction of additional energy contributions, as described generally by (3.26), might completely change the optimal configuration. Figure 3.12 shows that the stable configuration changes completely for different values of the material coefficient k_{46}. Indeed, Figure 3.12(a) depicts only two equilibrium configurations, $\theta = 0$ stable and $\theta = \frac{\pi}{2}$ unstable. On the other hand, Figure 3.12(b) shows that for higher values of k_{46}, the parallel configuration $\theta = 0$ becomes unstable, while a stable oblique configuration $\theta = 30° - 40°$ emerges.

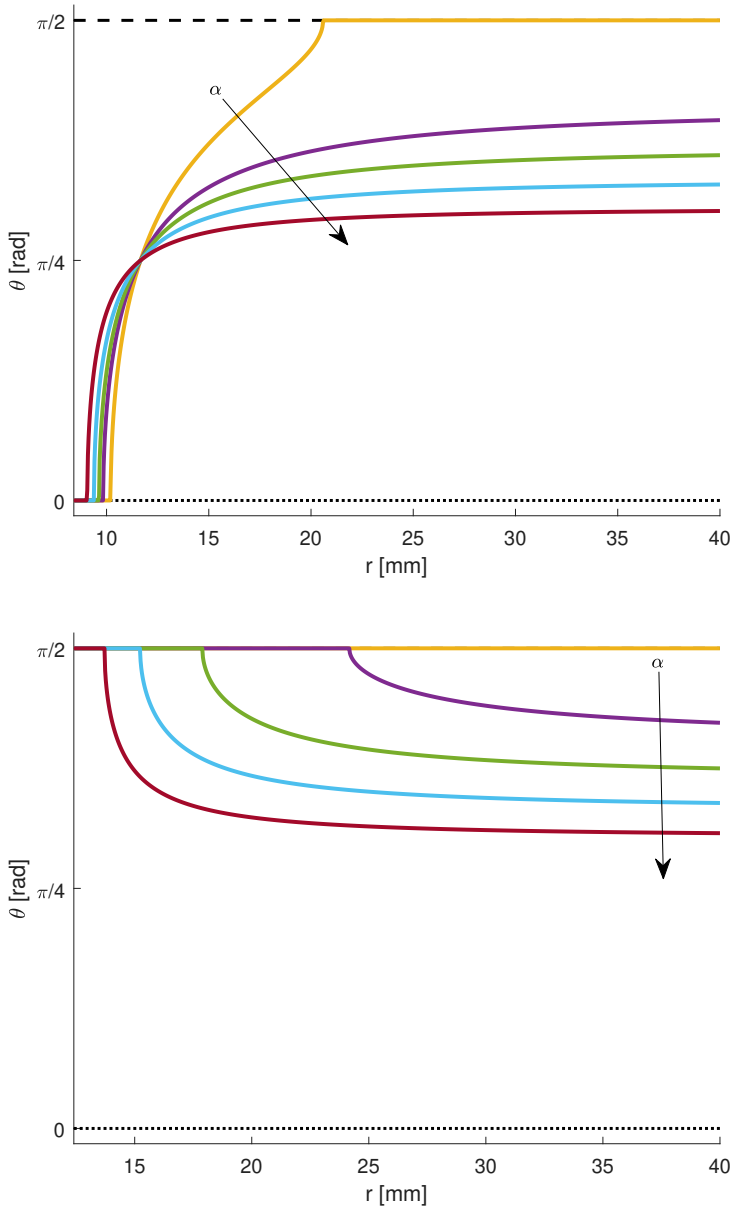

Figure 3.10. Bifurcation diagram of equilibrium angle in terms of deformed radius r for different $\alpha \in \{0.8, 1.2, 1.5, 2, 3\}$ and undeformed radius $R = 10$ mm. Solid lines describe stable configurations, while dashed lines describe unstable configurations. The axial stretches are set to (a) $\lambda_l = 0.8$ and (b) $\lambda_l = 1.2$.

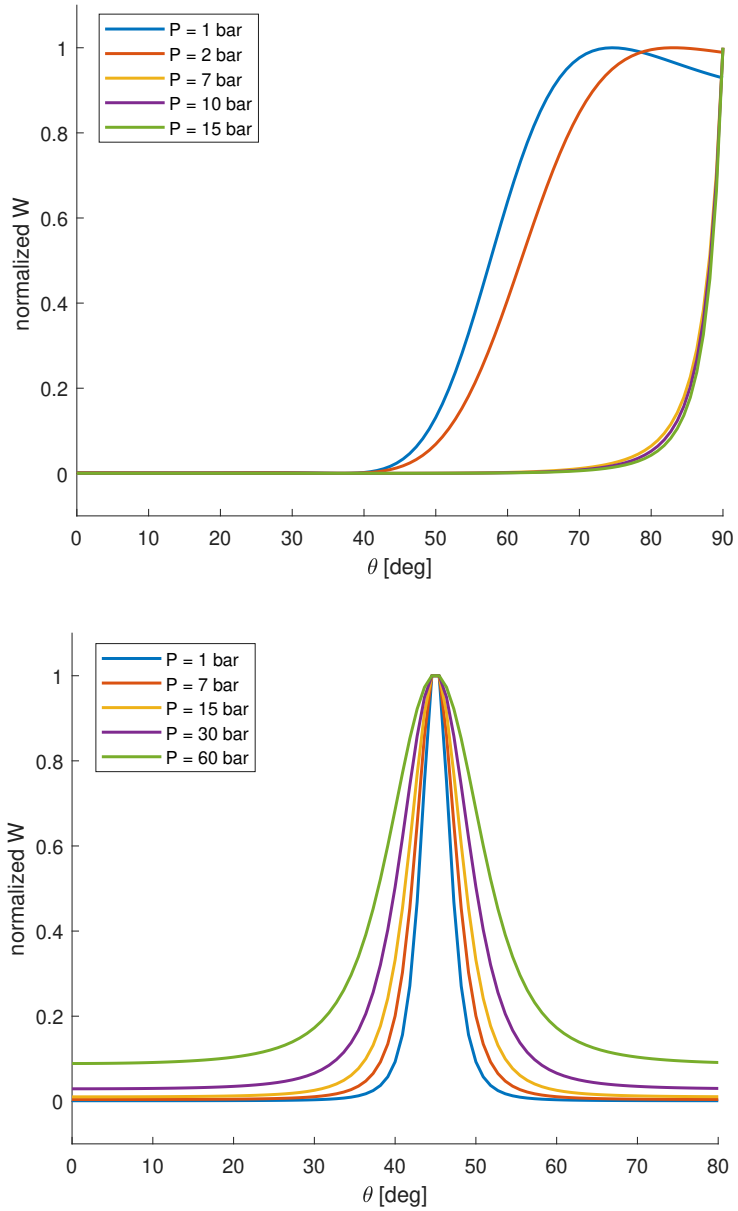

Figure 3.11. Normalized strain-energy function W against the angle θ for different values of internal pressure P. The material parameter used are $\mu = 260KPa$, $\alpha_1 = \alpha_2 = 23 \cdot 10^3 KPa$ for (a) balanced angle-ply (3.24) (b) orthogonal (3.25).

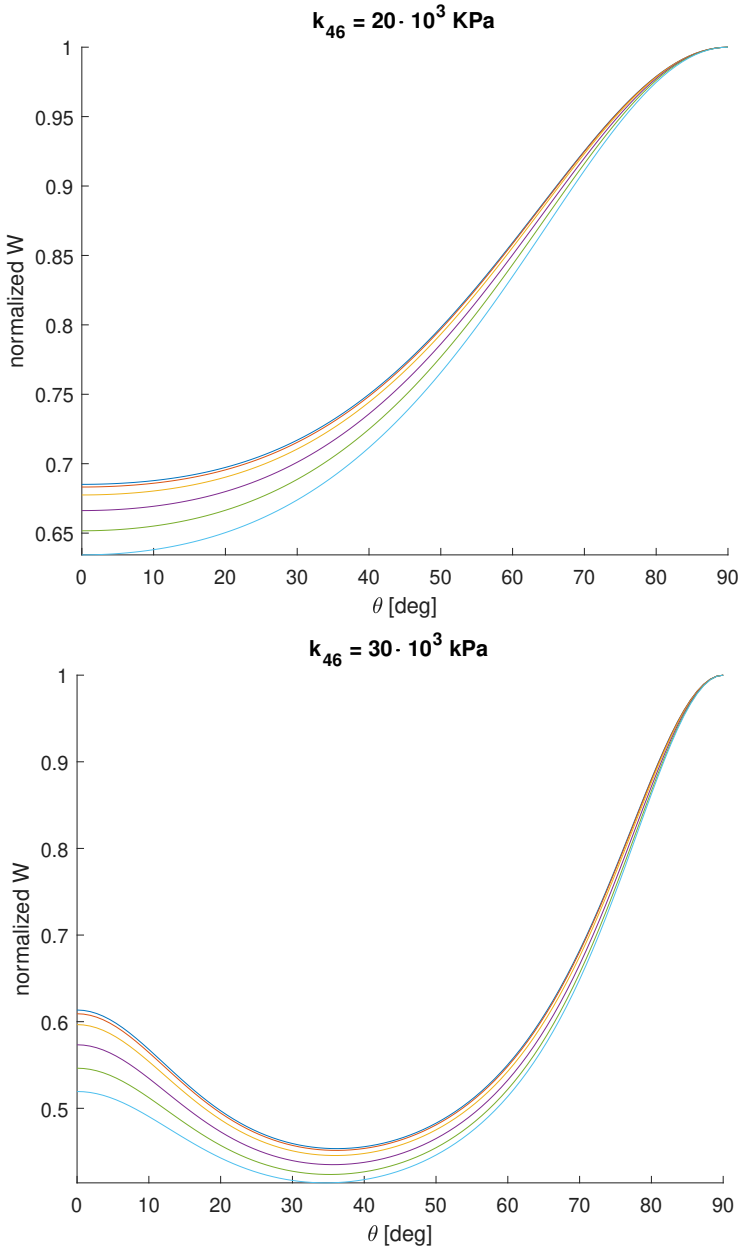

Figure 3.12. Normalized energy against θ for different values of internal pressure P. The energy is decribed by (3.26) with material parameters $\mu = 26 \cdot 10^3 kPa$, $k_{44} = 23 \cdot 10^3 kPa$, $k_{66} = 13 \cdot 10^3 kPa$ and (a) $k_{46} = 20 \cdot 10^3 kPa$, (b) $= k_{46} = 30 \cdot 10^3 kPa$.

Chapter 4

Reorientation in initially stressed materials

Initially stressed materials are a class of materials that possess pre-existing stress distributions before any external loads are applied. The nature of such pre-stresses relies on internal forces that develop within a material due to a wide range of factors, such as the manufacturing process, thermal effects, mechanical treatments, and, in the case of biological tissue, growth or remodeling.

A peculiar example is observed directly from biology. When an artery is dissected from the body, it contracts in length, reaching an *unloaded* configuration. However, the artery remains stressed throughout its volume. A radial cut along the artery partially releases the internal stress, relaxing the ring to form an open sector, as discussed in [40]. This phenomenon cannot occur if the unloaded configuration were unstressed, as there would be no change after the radial cut. In general, even the opened ring configuration is not stress-free since the opening angle of different layers is not the same.

The theory of residual stressed bodies has been widely investigated since the 1990s. From a mathematical perspective, some fundamental aspects of the influence of residual stress on the constitutive laws have been extensively studied by Hoger and co-workers [43–45]. This remains an intriguing research topic, attracting continued interest from researchers, such as Gower and co-workers [46–48]. Nonetheless, there are still questions regarding the validity of some relevant results, as detailed in [49].

Although residual stress is usually developed by inelastic processes, as highlighted above, there are cases where initial stress is produced by elastic deformation. For instance, turning a spherical cap upside down may result in residual stress, or when a body is elastically deformed from a stress-free configuration, and the deformed state is considered the unloaded one. A theoretical framework to treat elastically pre-stressed material was first developed by Johnson and Hoger [45] and has been used and improved in recent years [50].

The aim of this Chapter is to analyze the effect caused by substrate curvature discussed in Chapter 2, within the wider context of tube inflation. The idea is that the elastic pre-stress due to the substrate curvature of a single cell might alter the bifurcation analysis of a

monolayer of cells on an inflated cylinder. This aims to fully understand the reorganization of the cell structure to include the present model in the simulation of the cell part of the arterial wall. In particular, Section 1 sets up the theoretical framework of the pre-stress theory, focusing on the orthotropic material and its consequences on the strain energy function. Section 2 discusses the properties that residual stress must satisfy in the special case of cylinder inflation. Lastly, Section 3 introduces residual strain based on the considerations from Chapter 2 and analyzes the effects of residual strain on the possible configurations.

4.1 Hyperelastic Theory of Residual Stress

Let us assume that the reference configuration $\mathscr{B}_r$ is not stress-free. Let $\mathbb{T}^{(r)}$ be the residual Cauchy stress field in the reference configuration $\mathscr{B}_r$. In general, the residual stress field cannot be computed directly by exploiting the strain-energy, as one can infer from the causes mentioned above. Nonetheless, it might be included inside a constitutive theory by means of the multiplicative decomposition theory, as we will discuss later.

Therefore, if there is a residual stress in the reference configuration, the equations of equilibrium impose that

$$\text{div } \mathbb{T}^{(r)} = \mathbf{0} \quad \text{in } \mathscr{B}_r \quad \text{B.C.} \quad \mathbb{T}^{(r)T}\mathbf{n} = \mathbf{0} \quad \text{on } \partial\mathscr{B}_r, \tag{4.1}$$

where the boundary is load-free and $\hat{\mathbf{n}}$ is a unit vector field orthogonal to the boundary $\partial\mathscr{B}_r$. One should note that there is no distinction between the Piola tensor field relative to the residual stress $\mathbb{S}^{(r)}$ and the Cauchy stress $\mathbb{T}^{(r)}$ in the reference configuration $\mathscr{B}_r$. It follows, upon application of the divergence theorem, that

$$\int_{\partial\mathscr{B}_r} \mathbb{S}^{(r)}\, dS = \mathbf{0}. \tag{4.2}$$

Thus, the residual stress cannot be uniform. In other words, the residual stress distribution across the domain is *necessarily inhomogeneous* and, therefore, geometry-dependent [1, 43]. Consequently, the constitutive law will necessarily be dependent on the geometry since it will inherit this dependence directly from the residual stress. In general, the process to develop a constitutive theory that includes initial stress follows these steps [43]:

- The strain-energy function W is written as a function of the new set of invariants referring to the deformation and the initial stress.
- The constitutive law of the stress - the response function - is derived directly from the derivative of the strain-energy.
- Other properties of the body, such as the shape and the material symmetries, may be integrated to simplify the final expression.

In general, the residual stress places restrictions on the material symmetry in the considered material body, thus it may vary from point to point. The constitutive laws

resulting from this restriction might be very complex, so we will not consider this issue here. Nonetheless, we will make some observations on the restrictions imposed on the residual stress $\mathbb{S}^{(r)}$ by the material symmetry.

4.1.1 Preliminary Considerations

Let $\mathbb{F}_e$ be the deformation gradient associated with the deformation map $\phi_e(\mathbf{X}) = \mathbf{x}$, i.e., $\mathbb{F}_e = \frac{\partial \phi_e}{\partial \mathbf{X}}$. Given a constitutive elastic energy W, if we assume that the deformation is *purely elastic*, the constitutive law for the Cauchy stress field $\mathbb{T}$ may be written in terms of a response function $\hat{T}$ such that $\mathbb{T}(\mathbf{X}) = \hat{T}(\mathbb{F}_e(\mathbf{X}), \mathbf{X})$ relative to the unloaded configuration $\mathscr{B}_r$. The objectivity constitutive axiom imposes the condition on the response function

$$\hat{T}(\mathbb{Q}\mathbb{F}_e) = \mathbb{Q}\hat{T}(\mathbb{F}_e)\mathbb{Q}^T \quad \forall \mathbb{F}_e \in \text{Lin}, \mathbb{Q} \in \text{Orth}. \tag{4.3}$$

In terms of the Piola-Kirchhoff tensor field $\mathbb{S} = \det(\mathbb{F}_e)\,\mathbb{T}\,\mathbb{F}_e^{-T} =: \hat{S}(\mathbb{F}_e)$, the objectivity implies that

$$\hat{S}(\mathbb{Q}\mathbb{F}_e) = \mathbb{Q}\hat{S}(\mathbb{F}_e) \quad \forall \mathbb{F}_e \in \text{Lin}, \mathbb{Q} \in \text{Orth}. \tag{4.4}$$

Moreover, if $\mathscr{G}_{\mathbf{X}}$ denotes the symmetry group of the material at the material point $\mathbf{X}$, then

$$\hat{T}(\mathbb{F}_e(\mathbf{X})\mathbb{Q}, \mathbf{X}) = \hat{T}(\mathbb{F}_e(\mathbf{X}), \mathbf{X}) \quad \forall \mathbb{Q} \in \mathscr{G}_{\mathbf{X}}. \tag{4.5}$$

Therefore, the combination of objectivity and material symmetry implies that

$$\hat{T}(\mathbb{Q}\mathbb{F}_e\mathbb{Q}^T) = \mathbb{Q}\hat{T}(\mathbb{F}_e)\mathbb{Q}^T, \quad \hat{S}(\mathbb{Q}\mathbb{F}_e\mathbb{Q}^T) = \mathbb{Q}\hat{S}(\mathbb{F}_e)\mathbb{Q}^T \quad \forall \mathbb{Q} \in \mathscr{G}_{\mathbf{X}}. \tag{4.6}$$

This implies that, evaluating equation (4.6) for $\mathbb{F}_e = \mathbb{I}$, given that $\mathbb{T}^{(r)} = \hat{T}(\mathbb{I})$,

$$\mathbb{Q}\mathbb{T}^{(r)} = \mathbb{T}^{(r)}\mathbb{Q} \quad \forall \mathbb{Q} \in \mathscr{G}_{\mathbf{X}}, \tag{4.7}$$

thus, the initial stress field $\mathbb{T}^{(r)}$ necessarily commutes with every element of the material symmetry group $\mathscr{G}_{\mathbf{X}}$ at the material point $\mathbf{X}$. Equation (4.7) places a restriction on the expression of the material stress that may be very limiting. For example, if the material is isotropic, i.e., the symmetry group is the set of orthogonal transformations $\mathscr{G}_{\mathbf{X}} = \text{Orth}$, then it can be proven that

$$\mathbb{T}^{(r)}(\mathbf{X}) = \alpha(\mathbf{X})\mathbb{I}. \tag{4.8}$$

Therefore, the equilibrium equations and the load-free boundary conditions imply that the scalar field $\alpha(\mathbf{X}) = 0$ within the material body $\mathscr{B}_r$ [44]. We conclude that an isotropic body cannot sustain any residual stress $\mathbb{T}^{(r)}$.

4.1.2 Residually Stressed Orthotropic Material

A material with three mutually perpendicular planes of symmetry is called orthotropic. Mathematically, the symmetry group consist of rotation through π about each $\mathbf{k}_i$, together with the reversal of each $\mathbf{k}_i$, where $\mathbf{k}_1, \mathbf{k}_2$, and $\mathbf{k}_3$ are three mutually orthogonal vector fields (in the sense that they are functions of the material point) that define the three

planes of symmetry. The restriction (4.7) implies that the residual stress $\mathbb{T}^{(r)}$ must have the form

$$\mathbb{T}^{(r)} = t_1(\mathbf{X})\mathbf{k}_1(\mathbf{X}) \otimes \mathbf{k}_1(\mathbf{X}) + t_2(\mathbf{X})\mathbf{k}_2(\mathbf{X}) \otimes \mathbf{k}_2(\mathbf{X}) + t_3(\mathbf{X})\mathbf{k}_3(\mathbf{X}) \otimes \mathbf{k}_3(\mathbf{X}) \tag{4.9}$$

where t_1, t_2, and t_3 are scalar fields, and $\mathbf{k}_1, \mathbf{k}_2$, and $\mathbf{k}_3$ are vector fields that depend on the material position in $\mathscr{B}_r$. Notice that, due to the orthogonality, this expression is equivalent to

$$\mathbb{T}^{(r)} = \hat{t}_1(\mathbf{X})\mathbb{I} + \hat{t}_2(\mathbf{X})\mathbf{k}_2(\mathbf{X}) \otimes \mathbf{k}_2(\mathbf{X}) + \hat{t}_3(\mathbf{X})\mathbf{k}_3(\mathbf{X}) \otimes \mathbf{k}_3(\mathbf{X}) \tag{4.10}$$

To write the equilibrium equations, observe that, for a general scalar field α and vector field $\mathbf{k}$, it holds

$$\begin{aligned} \mathrm{Div}(\alpha(x)\mathbf{k}(x) \otimes \mathbf{k}(x))_j &= k_j k_i \frac{\partial \alpha}{\partial x_i} + \alpha \frac{\partial k_j}{\partial x_i} k_i + \alpha \frac{\partial k_i}{\partial x_i} k_j = \\ &= [\mathbf{k}(x) \otimes \mathbf{k}(x)]\nabla\alpha(x) + \alpha(x)[(\nabla\mathbf{k})\mathbf{k}(x) + (\nabla \cdot \mathbf{k})\mathbf{k}(x)]_j \end{aligned} \tag{4.11}$$

where Einstein notation is used for the index i - i.e., it sums over $i = 1, 2, 3$. Hence,

$$\mathrm{Div}(\alpha(x)\mathbf{k}(x) \otimes \mathbf{k}(x)) = [\mathbf{k}(x) \otimes \mathbf{k}(x)]\nabla\alpha(x) + \alpha(x)[(\nabla\mathbf{k})\mathbf{k}(x) + (\nabla \cdot \mathbf{k})\mathbf{k}(x)]. \tag{4.12}$$

Therefore, the equilibrium equation for the residual stress in the form (4.9) reads as

$$[\mathbf{k}_i(X) \otimes \mathbf{k}_i(X)]\nabla t_i(x) + t_i(X)[(\nabla\mathbf{k}_i)\mathbf{k}_i(x) + (\nabla \cdot \mathbf{k}_i)\mathbf{k}_i(X)] = \mathbf{0} \tag{4.13}$$

and the boundary condition becomes

$$t_i(\mathbf{k}_i \cdot \mathbf{n})\mathbf{k}_i = \mathbf{0}. \tag{4.14}$$

The dependence of the residual stress tensor field $\mathbb{T}^{(r)}$ on the position may significantly simplify the complexity of the problem. In particular, our goal is to study the deformation of an inflated tube, which we will analyze in detail later.

4.1.3 Strain Energy Function

An original approach [45–47] consists in taking advantage of the existence of a virtual stress-free state described by the configuration $\mathscr{B}_0$. Let $\mathscr{B}_0$ be a *virtual stress-free* configuration, while $\mathscr{B}_r$ and $\mathscr{B}$ are the *unloaded* and *current* configurations, respectively. The idea is to prescribe a constitutive law in the reference configuration $\mathscr{B}_r$ with an initial stress field $\mathbb{T}^{(r)}$ starting from a hyperelastic strain-energy function defined in the stress-free configuration. Let us assume that the material is orthotropic in $\mathscr{B}_0$, described by the two families of fibers $\mathbf{N}$ and $\mathbf{N}^{\perp}$, and thus, the elastic energy function will depend on the set of invariants:

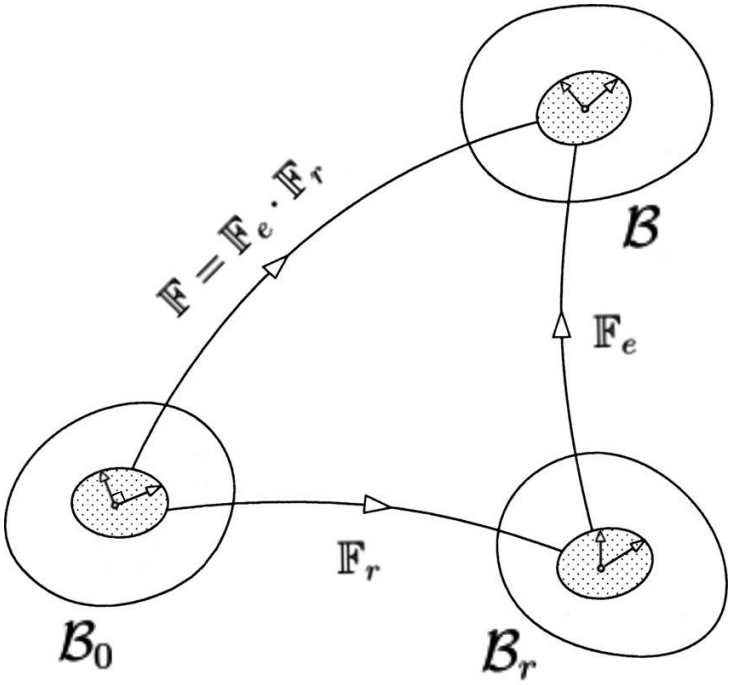

Figure 4.1. Visualization of the multiplicative decomposition technique. For more details, see [51].

$$\begin{aligned} I_1 = \mathrm{tr}\mathbb{C}, \quad I_2 = \frac{1}{2}(\mathrm{tr}(\mathbb{C}^2) - (\mathrm{tr}(\mathbb{C}))^2), \quad I_3 = \det \mathbb{C}, \\ I_4 = \mathbb{C} : \mathbb{A}, \quad I_5 = \mathbb{C}^2 : \mathbb{A}, \\ I_6 = \mathbb{C} : \mathbb{A}^\perp, \quad I_7 = \mathbb{C}^2 : \mathbb{A}^\perp, \\ I_8 = \mathbf{N}^\perp \cdot (\mathbb{C}\mathbf{N}) \end{aligned} \tag{4.15}$$

where $\mathbb{A} = \mathbf{N} \otimes \mathbf{N}$, $\mathbb{A}^\perp = \mathbf{N}^\perp \otimes \mathbf{N}^\perp$ are the structural tensors associated with the two families of fibers, and : denotes the double contraction operation. There are several possible choices of elastic strain energy; for our purposes, we will choose an energy strain function for incompressible material of the form [23]:

$$W(\mathbb{C}, \mathbb{A}, \mathbb{A}^\perp) = \frac{1}{2}\mathbf{I} \cdot \mathbb{K}\mathbf{I} + \mathscr{V}(I_1) \tag{4.16}$$

where $\mathbf{I} = (\hat{I}_4, \hat{I}_5, \hat{I}_6, \hat{I}_7, I_8)$, with $\hat{I}_j = I_j - 1$. If we neglect the dependence on $\mathbb{C}^2$ terms, i.e., on I_5 and I_7, for the same reasons highlighted in Chapter 3, Section 4, the strain energy function expanded may be written as:

$$
\begin{aligned}
W(\mathbb{C},\mathbb{A},\mathbb{A}^{\perp}) =& \frac{\mu}{2}(I_1-3) \\
&+ \frac{k_{44}}{2}(I_4-1)^2 + \frac{k_{66}}{2}(I_6-1)^2 \\
&+ k_{46}(I_4-1)(I_6-1) + \frac{k_{88}}{2}I_8^2
\end{aligned}
\tag{4.17}
$$

Now, let us describe the total deformation gradient $\mathbb{F}$ by means of the multiplicative decomposition $\mathbb{F}=\mathbb{F}_e\mathbb{F}_r$, where, in particular, $\mathbb{F}_r$ describes an elastic deformation from the virtual configuration $\mathscr{B}_0$ to the *locally* unloaded reference configuration $\mathscr{B}_r$ which, therefore, generates an elastic residual stress in that configuration, while $\mathbb{F}_e$ describes a deformation from the unloaded configuration $\mathscr{B}_r$ to the current configuration $\mathscr{B}$, as depicted in Figure 4.1. The physical meaning is that the total deformation $\mathbb{F}$ is decomposed into deformations $\mathbb{F}_e$ and $\mathbb{F}_r$, where we imagine first applying the deformation described by $\mathbb{F}_r$ and then deforming the body in the unloaded configuration with $\mathbb{F}_e$. Therefore, by plugging in $\mathbb{F}=\mathbb{F}_e\mathbb{F}_r$ inside the hyperelastic energy, we have:

$$
\begin{aligned}
W(\mathbb{F}_r^T\mathbb{C}_e\mathbb{F}_r,\mathbb{A},\mathbb{A}^{\perp}) =& \frac{\mu}{2}(\mathbb{B}_r:\mathbb{C}_e-3) \\
&+ \frac{k_{44}}{2}(\mathbb{C}_e:\mathbb{A}_r-1)^2 + \frac{k_{66}}{2}(\mathbb{C}_e:\mathbb{A}_r^{\perp}-1)^2 \\
&+ k_{46}(\mathbb{C}_e:\mathbb{A}_r-1)(\mathbb{C}_e:\mathbb{A}_r^{\perp}-1) + \frac{k_{88}}{2}(\mathbf{N}_r^{\perp}\cdot(\mathbb{C}_r\mathbf{N}_r))^2
\end{aligned}
\tag{4.18}
$$

where we defined $\mathbb{A}_r=\mathbb{F}_r\mathbb{A}\mathbb{F}_r^T$ and $\mathbb{A}_r^{\perp}=\mathbb{F}_r\mathbb{A}^{\perp}\mathbb{F}_r^T$, $\mathbf{N}_r=\mathbb{F}_r\mathbf{N}$, $\mathbf{N}_r^{\perp}=\mathbb{F}_r\mathbf{N}^{\perp}$ and the trivial ones $\mathbb{C}_e=\mathbb{F}_e^T\mathbb{F}_e$ and $\mathbb{B}_r=\mathbb{F}_r\mathbb{F}_r^T$.

The Cauchy stress may be computed directly from the constitutive elastic energy as:

$$
\sigma = 2\mathbb{F}\frac{\partial W}{\partial \mathbb{C}}\mathbb{F}^T - p\mathbb{I} \tag{4.19}
$$

where p is the Lagrange multiplier associated with the non-compressible constraint. Therefore, the differentiation of the elastic energy (4.17) gives:

$$
\begin{aligned}
\sigma = \mu\mathbb{B} - p\mathbb{I} &+ 2[k_{44}(\mathbb{C}:\mathbb{A}-1)+k_{46}(\mathbb{C}:\mathbb{A}^{\perp}-1)]\mathbb{F}\mathbb{A}\mathbb{F}^T \\
&+ 2[k_{66}(\mathbb{C}:\mathbb{A}^{\perp}-1)+k_{46}(\mathbb{C}:\mathbb{A}-1)]\mathbb{F}\mathbb{A}^{\perp}\mathbb{F}^T + k_{88}(\mathbf{N}^{\perp}\cdot(\mathbb{C}\mathbf{N}))\mathbb{F}\mathbb{D}\mathbb{F}^T
\end{aligned}
\tag{4.20}
$$

where we defined $\mathbb{D}=\frac{1}{2}(\mathbf{N}\otimes\mathbf{N}^{\perp}+\mathbf{N}^{\perp}\otimes\mathbf{N})$.

The goal is to write the elastic energy in the reference configuration $\mathscr{B}_r$ in a manner that does not depend on the initial elastic deformation $\mathbb{F}_r$ as in (4.17), but rather as a function of the residual stress $\mathbb{T}^{(r)}$ resulting from such deformation. Firstly, note that changing

reference configurations alters the expression of the strain energy as follows [49, 52]:

$$\tilde{W}(\mathbb{F}_e;\mathbb{F}_r) = J_r^{-1} W(\mathbb{F}\mathbb{F}_r) \quad \forall \mathbb{F}_e, \mathbb{F}_r \in \mathrm{Lin}, \tag{4.21}$$

where $J_r = \det(\mathbb{F}_r)$. In the context of incompressibility, $J_r = 1$, allowing us to drop the $\tilde{\cdot}$ notation from here on. Additionally, we can express terms that depend on the initial deformation as a function of the residual stress $\mathbb{T}^{(r)}$ using the *compatibility condition* of the Cauchy stress in the reference configuration $\mathscr{B}_r$. This condition states that the residual stress generated by the deformation gradient $\mathbb{F}_r$ must equal the response function (4.20) for $\mathbb{F} = \mathbb{F}_r$. Thus, by setting $\mathbb{F} = \mathbb{F}_e\mathbb{F}_r = \mathbb{F}_r$, for $\mathbb{F}_e = \mathbb{I}$ it holds that $\sigma = \mathbb{T}^{(r)}$, thus:

$$\begin{aligned}\mathbb{T}^{(r)} = \mu\mathbb{B}_r - p_r\mathbb{I} + [2k_{44}(\mathbb{I}:\mathbb{A}_r - 1) + k_{46}(\mathbb{I}:\mathbb{A}_r^{\perp} - 1)]\mathbb{A}_r \\ + 2[k_{66}(\mathbb{I}:\mathbb{A}_r^{\perp} - 1) + k_{46}(\mathbb{I}:\mathbb{A}_r - 1)]\mathbb{A}_r^{\perp} + k_{88}(\mathbb{I}:\mathbb{D}_r)\mathbb{D}_r.\end{aligned} \tag{4.22}$$

Notice that, in order to write the strain energy (4.17) for a given set of material parameters $\mu, k_{44}, k_{66}, k_{46}, k_{88}$ and the two structural tensors $\mathbb{A}_r$ and $\mathbb{A}_r^{\perp}$, we must explicitly write the invariant $I_{r_1} = \mathbb{B}_r\mathbb{C}_e$ and the pressure $p_r = p(\mathbb{F}_r)$ as functions of the initial stress field. By multiplying (4.22) by $\mathbb{C}_e$ on the right and taking the trace, we have:

$$\begin{aligned}\mathbb{T}^{(r)}:\mathbb{C}_e = \mu\mathbb{B}_r:\mathbb{C}_e + 2[k_{44}(\mathbb{I}:\mathbb{A}_r - 1) + k_{46}(\mathbb{I}:\mathbb{A}_r^{\perp} - 1)]\mathbb{C}_e:\mathbb{A}_r \\ + 2[k_{66}(\mathbb{I}:\mathbb{A}_r^{\perp} - 1) + k_{46}(\mathbb{I}:\mathbb{A}_r - 1)]\mathbb{C}_e:\mathbb{A}_r^{\perp} + k_{88}(\mathbb{I}:\mathbb{D}_r)(\mathbb{C}_e:\mathbb{D}_r) - p_r\,\mathrm{tr}\,\mathbb{C}_e\end{aligned} \tag{4.23}$$

which allows us to write the invariant $I_{1_r} = \mathrm{tr}(\mathbb{F}_r\mathbb{C}_e\mathbb{F}_e^T)$ as a function of the other terms defined in the reference configuration $\mathscr{B}_r$. Finally, it remains to compute the Lagrange multiplier associated with the elastic deformation $\mathbb{F}_r$. Since the material is not compressible in the virtual stress-free configuration $\mathscr{B}_0$, we can exploit the fact that $\det(\mathbb{F}_r) = 1$, leading to, by taking the determinant of (4.22),

$$\det(\mathbb{T}^{(r)} + p_r\mathbb{I}) = \det(\mathbb{F}_r)\det(\mu\mathbb{I} + \mathbb{S}_r)\det(\mathbb{F}_r) \tag{4.24}$$

where the tensor $\mathbb{S}_r$ is defined as:

$$\mathbb{S}_r = [2k_{44}(\mathbb{I}:\mathbb{A}_r - 1) + k_{46}(\mathbb{I}:\mathbb{A}_r^{\perp} - 1)]\mathbb{A} + [2k_{66}(\mathbb{I}:\mathbb{A}_r^{\perp} - 1) + k_{46}(\mathbb{I}:\mathbb{A}_r - 1)]\mathbb{A}^{\perp} + 2k_{88}(\mathbb{I}:\mathbb{D}_r)\mathbb{D}. \tag{4.25}$$

Therefore, by plugging in these results, the elastic energy is written as

$$\begin{aligned} W(\mathbb{C}_e, \mathbb{T}^{(r)}) =& \frac{1}{2}(\mathbb{T}^{(r)} : \mathbb{C}_e + p_r \operatorname{tr}(\mathbb{C}_e) - 3\mu) \\ &+ \frac{k_{44}}{2}(\mathbb{C}_e : \mathbb{A}_r - 1)^2 - \frac{2k_{44}(\operatorname{tr}\mathbb{A}_r - 1) + k_{46}(\operatorname{tr}\mathbb{A}_r^{\perp} - 1)}{2}\mathbb{C}_e : \mathbb{A}_r \\ &+ \frac{k_{66}}{2}(\mathbb{C}_e : \mathbb{A}_r^{\perp} - 1)^2 - \frac{2k_{66}(\operatorname{tr}\mathbb{A}_r^{\perp} - 1) + k_{46}(\operatorname{tr}\mathbb{A}_r - 1)}{2}\mathbb{C}_e : \mathbb{A}_r^{\perp} \\ &+ k_{46}(\mathbb{C}_e : \mathbb{A}_r - 1)(\mathbb{C}_e : \mathbb{A}_r^{\perp} - 1) \\ &+ \frac{k_{88}}{2}(\mathbf{N}_r^{\perp} \cdot (\mathbb{C}_e \mathbf{N}_r))^2 - k_{88}(\mathbb{I} : \mathbb{D}_r)(\mathbb{C}_e : \mathbb{D}_r) \end{aligned} \tag{4.26}$$

where p_r is the positive root of

$$p_r^3 + I_{T_1^{(r)}} p_r^2 + I_{T_2^{(r)}} p_r + I_{T_3^{(r)}} = \mu^3 + I_{\mathbb{S}_1}\mu^2 + I_{\mathbb{S}_2}\mu + I_{\mathbb{S}_3} = 0 \tag{4.27}$$

where $I_{\mathbb{T}_j^{(r)}}$,$I_{\mathbb{S}_j}$ denote the first three invariants of the tensors $\mathbb{T}^{(r)}$ and $\mathbb{S}$, respectively. Notice that, if there is no residual stress $\mathbb{T}^{(r)} \equiv \mathbf{0}$, i.e. the elastic deformation tensor $\mathbb{F}_r = \mathbb{I}$, the solution of (4.27) reduces to $p_r = \mu$ and, moreover, $\operatorname{tr}\mathbb{A}_r = \operatorname{tr}\mathbb{A} = 1$ and $\operatorname{tr}\mathbb{A}_r^{\perp} = \operatorname{tr}\mathbb{A}^{\perp} = 1$, the strain energy W returns in the initial form (4.17), as expected.

After a bit of algebraic manipulation, the strain energy function may be written as:

$$\begin{aligned} W(\mathbb{C}_e, \mathbb{T}^{(r)}) =& \frac{1}{2}(\mathbb{T}^{(r)} : \mathbb{C}_e + p_r \operatorname{tr}(\mathbb{C}_e) - 3\mu) \\ &+ \frac{k_{44}}{2}((\mathbb{C}_e - \mathbb{I}) : \mathbb{A}_r)^2 \\ &+ \frac{k_{66}}{2}((\mathbb{C}_e - \mathbb{I}) : \mathbb{A}_r^{\perp})^2 \\ &+ k_{46}((\mathbb{C}_e - \mathbb{I}) : \mathbb{A}_r)((\mathbb{C}_e - \mathbb{I}) : \mathbb{A}_r^{\perp}) \\ &+ \frac{k_{88}}{2}(\mathbf{N}_r^{\perp} \cdot (\mathbb{C}_e \mathbf{N}_r))^2 - k_{88}(\mathbb{I} : \mathbb{D}_r)(\mathbb{C}_e : \mathbb{D}_r) \\ &- \frac{1}{2}(k_{44} \operatorname{tr}(\mathbb{A}_r)^2 + k_{46}\operatorname{tr}(\mathbb{A}_r) \operatorname{tr}(\mathbb{A}_r^{\perp}) + k_{66}\operatorname{tr}(\mathbb{A}_r^{\perp})^2). \end{aligned} \tag{4.28}$$

This form allows us to distinguish the energy contribution given by the initial stress since, for $\mathbb{C}_e = \mathbb{I}$ most of the contributions disappear leading to

$$\begin{aligned} W(\mathbb{I}, \mathbb{T}^{(r)}) =& \frac{1}{2}(\operatorname{tr}\mathbb{T}^{(r)} + 3(p_r - \mu)) \\ &- \frac{1}{2}(k_{44}\operatorname{tr}(\mathbb{A}_r)^2 + k_{46}\operatorname{tr}(\mathbb{A}_r)\operatorname{tr}(\mathbb{A}_r^{\perp}) + k_{66}\operatorname{tr}(\mathbb{A}_r^{\perp})^2). \end{aligned} \tag{4.29}$$

4.2 Residual Stress in Cylinder Inflation

The kinematics of deformation of the tube is the same as defined in Chapter 2, Section 1. Specifically, we assume an elastic deformation that maintains cylindrical symmetry, meaning the deformation fields depend only on the radial coordinate R of the material point $\mathbf{X} = (R, \Theta, Z)$ in the unloaded configuration $\mathscr{B}_r$. This geometric choice allows us to make further observations on the residual stress field $\mathbb{T}^{(r)}$ within the body. For clarity, we report the equilibrium equation (4.1) in cylindrical coordinates:

$$\begin{aligned} \frac{\partial T^{(r)}_{RR}}{\partial R} + \frac{1}{R}\frac{\partial T^{(r)}_{R\Theta}}{\partial \Theta} + \frac{\partial T^{(r)}_{RZ}}{\partial Z} + \frac{1}{R}(T^{(r)}_{RR} - T^{(r)}_{\Theta\Theta}) = 0, \\ \frac{\partial T^{(r)}_{R\Theta}}{\partial R} + \frac{1}{R}\frac{\partial T^{(r)}_{\Theta\Theta}}{\partial \Theta} + \frac{\partial T^{(r)}_{\Theta Z}}{\partial Z} + \frac{2}{R}T^{(r)}_{R\Theta} = 0, \\ \frac{\partial T^{(r)}_{RZ}}{\partial R} + \frac{1}{R}\frac{\partial T^{(r)}_{\Theta Z}}{\partial \Theta} + \frac{\partial T^{(r)}_{ZZ}}{\partial Z} + \frac{1}{R}T^{(r)}_{RZ} = 0. \end{aligned} \tag{4.30}$$

These equations are simplified if we make some assumptions about the form of the residual stress $\mathbb{T}^{(r)}$ in (4.10). For instance, let $\mathbf{k}_3$ be independent of the position. Therefore, the equilibrium equation of the residual stress $\mathbb{T}^{(r)}$ implies that t_3 is independent of the scalar coordinate associated with the vector $\mathbf{k}_3$. If, in addition, we identify the direction $\mathbf{k}_3$ with the axis of the cylinder, applying the boundary conditions on the ends of the tube implies that $t_3 = 0$ [1]. Thus, the residual stress $\mathbb{T}^{(r)}$ does not depend on the direction $\mathbf{k}_3$. In polar coordinates, the remaining equations read as [53]:

$$\begin{aligned} \frac{\partial}{\partial R}(R^2 T^{(r)}_{\Theta R}) + R\frac{\partial T^{(r)}_{\Theta\Theta}}{\partial \Theta} = 0, \\ \frac{\partial}{\partial R}(R T^{(r)}_{RR}) + \frac{\partial T^{(r)}_{R\Theta}}{\partial \Theta} - T^{(r)}_{\Theta\Theta} = 0, \end{aligned} \tag{4.31}$$

where $T^{(r)}_{RR}, T^{(r)}_{R\Theta}$, and $T^{(r)}_{\Theta\Theta}$ are the components of $\mathbb{T}^{(r)}$. Moreover, if the field does not depend on Θ by assumption, the boundary condition (4.14) on the cylindrical surface implies that $T^{(r)}_{R\Theta} \equiv 0$. Therefore, we have $T^{(r)}_{RR} = t_1$ and $T^{(r)}_{\Theta\Theta} = t_2$. Thus, the system of equations (4.31) collapses into a single differential equation:

$$\frac{dt_1}{dR} + \frac{t_1 - t_2}{R} = 0, \tag{4.32}$$

coupled with the pair of equations (3.5) and the boundary condition on the surface of the tube:

$$t_1 = 0 \quad \text{on } R = A, B. \tag{4.33}$$

Even though this is just a simple case, it is clear how much the geometry and material symmetry influence the shape of the residual stress $\mathbb{T}^{(r)}$.

In general, the system of equations (4.31) coupled with the boundary condition may

be solved using an Airy potential $\psi = \psi(R, \Theta)$ [53], i.e., defining the residual stress as:

$$\begin{aligned} T^{(r)}_{RR} &= \frac{1}{R}\frac{\partial \psi}{\partial R} + \frac{1}{R^2}\frac{\partial^2 \psi}{\partial \Theta^2}, \\ T^{(r)}_{R\Theta} &= \frac{1}{R^2}\frac{\partial \psi}{\partial \Theta} - \frac{1}{R}\frac{\partial^2 \psi}{\partial R \partial \Theta}, \\ T^{(r)}_{\Theta\Theta} &= \frac{\partial^2 \psi}{\partial R^2}. \end{aligned} \tag{4.34}$$

By exploiting the Airy potential ψ, this set of equations allows us to easily define the initial stress field $\mathbb{T}^{(r)}$ by only prescribing the function $\psi(R, \Theta)$. Notice that, when we assume there is no dependence on Θ as previously done, the residual stress component $T^{(r)}_{R\Theta} \equiv 0$, thus the initial stress will be diagonal with components:

$$T^{(r)}_{RR} = t_1 = \frac{1}{R} f(R), \quad T^{(r)}_{\Theta\Theta} = t_2 = f'(R), \tag{4.35}$$

where $f(R) = \psi'(R)$ with $f(A) = f(B) = 0$. Therefore, if we allow the system to be independent of the material coordinate Θ, the analysis is simplified and the residual stress may be defined by the introduction of a function $f(R)$, regarded as a *stress potential* [53].

However, this reasoning holds under the assumption that $\mathbf{k}_3$ is parallel to the axis of the cylinder. In general, we want to describe a body with two families of fibers mutually orthogonal on the plane (Θ, Z) to model the anisotropic response of the cell given by the stress fibers network. Let us assume that the two structural tensors $\mathbb{A} = \mathbf{N} \otimes \mathbf{N}$ and $\mathbb{A}^{\perp} = \mathbf{N}^{\perp} \otimes \mathbf{N}^{\perp}$ are given by:

$$\mathbb{A} = \begin{bmatrix} 0 & 0 & 0 \\ 0 & \cos^2(\varphi) & \frac{\sin(2\varphi)}{2} \\ 0 & \frac{\sin(2\varphi)}{2} & \sin^2(\varphi) \end{bmatrix}, \quad \mathbb{A}^{\perp} = \begin{bmatrix} 0 & 0 & 0 \\ 0 & \sin^2(\varphi) & -\frac{\sin(2\varphi)}{2} \\ 0 & -\frac{\sin(2\varphi)}{2} & \cos^2(\varphi) \end{bmatrix}, \tag{4.36}$$

where φ is the angle between the circumferential direction and the vector $\mathbf{N}$. In general, φ may depend on the position $\mathbf{X}$ if the directions $\mathbf{N}$ and $\mathbf{N}^{\perp}$ vary within the body. Here we assume that it is constant for simplicity. It follows from the general form of the residual stress (4.9) that $T^{(r)}_{R\Theta} = T^{(r)}_{RZ} = 0$ and $T^{(r)}_{RR} = t_1(\mathbf{X})$. Notice that we implicitly assumed that $\mathbf{k}_1$ coincides with the radial direction in the cylindrical coordinate system. If, moreover, we assume that the scalar fields t_j do not depend on the coordinates Θ and Z, the equilibrium equation system (4.30) collapses into the radial equilibrium:

$$\frac{\partial t_1}{\partial R} + \frac{1}{R}(t_1 - t_2 \cos^2(\varphi) - t_3 \sin^2(\varphi)) = 0, \tag{4.37}$$

with boundary conditions $t_1(A) = t_2(B) = 0$ on the inner $(R = A)$ and outer $(R = B)$ cylindrical surfaces. The remaining components must satisfy the boundary conditions at the ends of the tube. As pointed out by Ogden [1] in the analysis of residual stress developed by the well-known opening angle method, the zero axial load condition is not generally compatible with the deformation from the virtual stress-free configuration $\mathscr{B}_0$

to the reference configuration $\mathscr{B}_r$. This problem also arises in our cases. In fact, if we assume free axial load at the ends of the tube, it must hold

$$\begin{aligned} 0 &= T^{(r)}_{\Theta Z} = (t_2(R) - t_3(R))\frac{\sin(2\varphi)}{2}, \\ 0 &= T^{(r)}_{ZZ} = t_2(R)\sin^2(\varphi) + t_3(R)\cos^2(\varphi). \end{aligned} \tag{4.38}$$

The trivial case $t_2 = t_3 \equiv 0$ is not considered since there would not be any residual stress supported. Similarly, if $t_2(R) = t_3(R)$, the boundary conditions would imply that $t_1 = t_2 = 0$, hence collapsing again into the trivial case. Finally, we observe that:

$$t_3(R) = -t_2(R)\tan^2(\varphi) \implies t_2\left(1 + \tan^2(\varphi)\right)\frac{\sin(2\varphi)}{2} = 0, \tag{4.39}$$

which, for a fixed $\varphi \neq 0, \pi/2$, holds if and only if $t_3 = t_2 = 0$. To resolve this issue, one may imagine that there is an axial load that controls the deformation. Thus, if W_0 is the strain energy function with respect to the stress-free configuration and λ_{z0} is the *fixed* uniform axial stretch, then the residual axial stretch may be computed from the equation in Chapter 3, Section 1 (3.5):

$$t_3 - t_1 = \lambda_{z0}\frac{\partial \hat{W}_0}{\partial \lambda_{z0}}, \tag{4.40}$$

where t_1 is computed by some other procedure. If the axial stretch λ_{z0} is not assumed uniform, the deformation becomes more complex, but we will not consider this problem. This framework is particularly useful because we can proceed by prescribing the form of $T^{(r)}_{RR}$ and $T^{(r)}_{\Theta\Theta}$ using some of the arguments described above, and then computing the axial residual stress $T^{(r)}_{ZZ}$ from the boundary condition for a fixed axial stretch, as done, for instance, in the recent paper by Mukherjee and colleagues [48].

4.2.1 Bifurcation analysis

The stationary configuration angles φ are given by setting to zero the derivative of (4.26) with respect to φ. Thus,

$$\begin{aligned} \frac{\partial W}{\partial \varphi} = {} & \frac{1}{2}\frac{\partial \mathbb{T}^{(r)}}{\partial \varphi} : \mathbb{C}_e + \frac{\partial p_r}{\partial \varphi}\operatorname{tr}(\mathbb{C}_e) + \\ & + k_{44}(\mathbb{C}_e : \mathbb{A}_r - 1)\mathbb{C}_e : \frac{\partial \mathbb{A}_r}{\partial \varphi} - \frac{\partial \hat{k}_{44}}{\partial \varphi}\mathbb{C}_e : \mathbb{A}_r - \hat{k}_{44}\mathbb{C}_e : \frac{\partial \mathbb{A}_r}{\partial \varphi} + \\ & + k_{66}(\mathbb{C}_e : \mathbb{A}_r^{\perp} - 1)\mathbb{C}_e : \frac{\partial \mathbb{A}_r^{\perp}}{\partial \varphi} - \frac{\partial \hat{k}_{66}}{\partial \varphi}\mathbb{C}_e : \mathbb{A}_r^{\perp} - \hat{k}_{66}\mathbb{C}_e : \frac{\partial \mathbb{A}_r^{\perp}}{\partial \varphi} + \\ & + k_{46}\big[(\mathbb{C}_e : \mathbb{A}_r - 1)\mathbb{C}_e : \frac{\partial \mathbb{A}_r^{\perp}}{\partial \varphi} + (\mathbb{C}_e : \mathbb{A}_r^{\perp} - 1)\mathbb{C}_e : \frac{\partial \mathbb{A}_r}{\partial \varphi}\big] + \\ & + \frac{k_{88}}{2}\frac{\partial[(\mathbf{N}_r^{\perp} \cdot (\mathbb{C}_e\mathbf{N}_r))^2]}{\partial \varphi} - k_{88}\frac{\partial[(\mathbb{I} : \mathbb{D}_r)(\mathbb{C}_e : \mathbb{D}_r)]}{\partial \varphi}, \end{aligned} \tag{4.41}$$

where

$$\begin{aligned}\hat{k}_{44} &= k_{44}(\operatorname{tr}\mathbb{A}_r - 1) + k_{46}(\operatorname{tr}\mathbb{A}_r^{\perp} - 1),\\ \hat{k}_{66} &= k_{66}(\operatorname{tr}, \mathbb{A}_r^{\perp} - 1) + k_{46}(\operatorname{tr}\mathbb{A}_r - 1).\end{aligned} \tag{4.42}$$

Then, by plugging in (4.42) and factorizing, we obtain:

$$\begin{aligned}\frac{\partial W}{\partial \varphi} &= \frac{1}{2}\frac{\partial \mathbb{T}^{(r)}}{\partial \varphi} : \mathbb{C}_e + \frac{\partial p_r}{\partial \varphi}\operatorname{tr}(\mathbb{C}_e) +\\ &+ \frac{1}{2}\Big[[2k_{44}(\operatorname{tr}(\mathbb{C}_e\mathbb{A}_r) - \operatorname{tr}(\mathbb{A}_r)) + k_{46}(\operatorname{tr}(\mathbb{C}_e\mathbb{A}_r^{\perp}) - \operatorname{tr}(\mathbb{A}_r^{\perp}))]\mathbb{C}_e\\ &- [2k_{44}\operatorname{tr}(\mathbb{C}_e\mathbb{A}_r) + k_{46}\operatorname{tr}(\mathbb{C}_e\mathbb{A}_r^{\perp})]\mathbb{I}\Big] : \frac{\partial \mathbb{A}_r}{\partial \varphi}\\ &+ \frac{1}{2}\Big[[2k_{66}(\operatorname{tr}(\mathbb{C}_e\mathbb{A}_r^{\perp}) - \operatorname{tr}(\mathbb{A}_r^{\perp})) + k_{46}(\operatorname{tr}(\mathbb{C}_e\mathbb{A}_r) - \operatorname{tr}(\mathbb{A}_r))]\mathbb{C}_e\\ &- [2k_{66}\operatorname{tr}(\mathbb{C}_e\mathbb{A}_r^{\perp}) + k_{46}\operatorname{tr}(\mathbb{C}_e\mathbb{A}_r)]\mathbb{I}\Big] : \frac{\partial \mathbb{A}_r^{\perp}}{\partial \varphi} +\\ &+ \frac{k_{88}}{2}\frac{\partial[(\mathbf{N}_r^{\perp}\cdot(\mathbb{C}_e\mathbf{N}_r))^2]}{\partial \varphi} - k_{88}\frac{\partial[(I : \mathbb{D}_r)(\mathbb{C}_e : \mathbb{D}_r)]}{\partial \varphi}.\end{aligned} \tag{4.43}$$

In order to proceed, let us assume that $\mathbb{C}_e$ is given by the deformation of a pure tube inflation, hence

$$\mathbb{C}_e = \operatorname{diag}(\lambda^{-2}\lambda_l^{-2}, \lambda^2, \lambda_l^2) \tag{4.44}$$

where the notation is coherent to Chapter 3, Section 1. Therefore, the tensors inside the parenthesis are diagonal. In order to simplify the computations, notice that if $\mathbb{B} = \operatorname{diag}(b_1, b_2, b_3)$ is a diagonal tensor, then the contraction with the derivative of the structural tensors (4.36) gives:

$$\mathbb{B} : \frac{\partial \mathbb{A}}{\partial \varphi} = (b_3 - b_2)\sin(2\varphi), \quad \mathbb{B} : \frac{\partial \mathbb{A}^{\perp}}{\partial \varphi} = (b_2 - b_3)\sin(2\varphi). \tag{4.45}$$

In the following we will assume that the initial deformation $\mathbb{F}_r$ does not change the direction of the fiber families, hence we will have $\mathbb{A}_r = \Lambda_1\mathbb{A}$ and $\mathbb{A}_r^{\perp} = \Lambda_2\mathbb{A}^{\perp}$, where Λ_1 and Λ_2 are measures of the extension along the stress fibers. This setup well describes an initial deformation that purely contracts the fibers along themselves, as in the case of the active contraction. Moreover, regarding the I_8 term, it follows that

$$\begin{aligned}\mathbf{N}_r \cdot \mathbf{N}_r^{\perp} &= 0,\\ \frac{\partial(\mathbf{N}_r^{\perp}\cdot(\mathbb{C}_e\mathbf{N}_r)^2)}{\partial \varphi} &= (\lambda_l^2 - \lambda^2)^2\Lambda_1\Lambda_2\frac{\sin(2\varphi)}{2}(2\cos^2(\varphi) - 1).\end{aligned} \tag{4.46}$$

Finally, after pluggin in the residual stress in the general form (4.14), it can be proven

that the strain-energy assumes the form

$$\frac{\partial W}{\partial \varphi}(\lambda,\lambda_l,t_1,t_2)=\frac{\sin(2\varphi)}{2}(\lambda^2-\lambda_l^2)\Big[(\lambda_l^2-\lambda^2)(\Lambda_1^2k_{44}+\Lambda_2^2k_{66}-2k_{46}\Lambda_2\Lambda_1-k_{88}\Lambda_1\Lambda_2)\cos^2(\varphi) + (k_{44}\Lambda_1^2-k_{46}\Lambda_1\Lambda_2)(\lambda_l^2-1)+(\Lambda_1\Lambda_2k_{46}-\Lambda_2^2k_{66})(\lambda^2-1) - \Lambda_1\Lambda_2\frac{k_{88}}{2}(\lambda_l^2-\lambda^2)+(\Lambda_2t_3-\Lambda_1t_2)\Big], \tag{4.47}$$

where we neglected the contribution of the term $\frac{\partial p_r}{\partial \varphi}$. Indeed, it can be proven that the invariants of $\mathbb{T}^{(r)}$ and $\mathbb{S}$ in (4.25) do not depend on the angle φ. Notice that the trivial configurations $\varphi=0$ and $\varphi=\frac{\pi}{2}$ are stationary points of the systems. Moreover, an additional oblique configuration φ^* satisfies

$$\cos^2(\varphi^*)=\frac{1}{2}+\frac{k_{44}\Lambda_1^2-k_{66}\Lambda_2^2}{k_{44}\Lambda_1^2+k_{66}\Lambda_2^2-2k_{46}\Lambda_1\Lambda_2-k_{88}\Lambda_1\Lambda_2}\Big(\frac{1}{2}-\frac{\lambda_l^2-1}{\lambda_l^2-\lambda^2} + \frac{1}{k_{44}\Lambda_1^2-k_{66}\Lambda_2^2}\frac{\Lambda_2t_3-\Lambda_1t_2}{\lambda_l^2-\lambda^2}\Big). \tag{4.48}$$

Notice that, upon redefining $\tilde{k}_{44}=\Lambda_1^2k_{44}$, $\tilde{k}_{66}=\Lambda_2^2k_{66}$, $\tilde{k}_{46}=\Lambda_1\Lambda_2k_{46}$, $\tilde{k}_{88}=\Lambda_1\Lambda_2k_{88}$, expression (4.48) assumes the more familiar form

$$\cos^2(\varphi^*)=\frac{1}{2}+\frac{\tilde{k}_{44}-\tilde{k}_{66}}{\tilde{k}_{44}+\tilde{k}_{66}-2\tilde{k}_{46}-\tilde{k}_{88}}\Big(\frac{1}{2}-\frac{\lambda_l^2-1}{\lambda_l^2-\lambda^2} + \frac{1}{\tilde{k}_{44}-\tilde{k}_{66}}\frac{\Lambda_2t_3-\Lambda_1t_2}{\lambda_l^2-\lambda^2}\Big) \tag{4.49}$$

which, besides the term associated with the residual stress dependent on t_3 and t_2, resembles the expression found by Lucci and Preziosi [23]. The stability of the stationary configurations depends on the sign of the second derivative of the energy with respect to φ. In particular, the analysis carries out the same way as Chapter 2 Section 3, it is straightforward to prove that:

- $\varphi=0$ stable if and only if

$$-\frac{\Lambda_1t_3-\Lambda_2t_2}{(\lambda_l^2-\lambda^2)(\tilde{k}_{44}-\tilde{k_{66}})}+\frac{\lambda_l^2-1}{\lambda_l^2-\lambda^2}>\frac{\tilde{\alpha}+1}{2}; \tag{4.50}$$

- $\varphi=\frac{\pi}{2}$ stable if and only if

$$-\frac{\Lambda_1t_3-\Lambda_2t_2}{(\lambda_l^2-\lambda^2)(\tilde{k}_{44}-\tilde{k_{66}})}+\frac{\lambda_l^2-1}{\lambda_l^2-\lambda^2}<\frac{\tilde{\alpha}-1}{2}; \tag{4.51}$$

- if there exists, $\varphi = \varphi^*$ stable if and only if

$$(\lambda^2 - \lambda_l^2)^2 \sin^2(2\varphi)(\tilde{k}_{44} + \tilde{k}_{66} - 2\tilde{k}_{46} - \tilde{k}_{88}) > 0. \tag{4.52}$$

4.3 Curvature and Active Contractility Effects Inserted by Prestrain

The purpose of this Section is to introduce the contributions of curvature and active contractility at the cellular level. To achieve this, it is necessary to introduce an appropriate gradient of deformation, $\mathbb{F}_r$, from the virtual stress-free configuration $\mathscr{B}_0$ to the reference configuration $\mathscr{B}_r$ in order to compute the optimal configuration directly from (4.18).

Based on the results obtained in Chapter 2, Section 2, and as observed above, active contractility shortens the fibers, maintaining their initial direction $\mathbf{N}$. Therefore, we propose the following gradient of deformation for the active contractility component:

$$\mathbb{F}_c = \mathbb{I} + C_1\mathbb{A} + C_2\mathbb{A}^\perp, \tag{4.53}$$

where $\mathbb{A}$ and $\mathbb{A}^\perp$ are the structure tensors of the material, and C_1 and C_2 are scalar fields measuring the compression due to contractility. Indeed, we observe that

$$\begin{aligned} \mathbb{F}_c\mathbf{N} &= \mathbf{N} + C_1\mathbb{A}\mathbf{N} + C_2\mathbb{A}^\perp\mathbf{N} = \\ &= \mathbf{N} + C_1(\mathbf{N}\cdot\mathbf{N})\mathbf{N} + C_2(\mathbf{N}^\perp\cdot\mathbf{N})\mathbf{N}^\perp = (1+C_1)\mathbf{N} \end{aligned} \tag{4.54}$$

and analogously,

$$\mathbb{F}_c\mathbf{N}^\perp = (1+C_2)\mathbf{N}^\perp. \tag{4.55}$$

Hence, since we are describing a compression, to ensure the invertibility of the deformation tensor $\mathbb{F}_c$, the scalar fields C_1 and C_2 must return values between $-1 < C_1, C_2 < 0$. Indeed, based on the considerations in Chapter 2, Section 2, these measures may be described by a linear function in the thickness of the tube, hence in the form:

$$C_1 = \alpha(R - R_a), \quad C_2 = \beta(R - R_a), \tag{4.56}$$

where R_a is the undeformed radius in the reference configuration $\mathscr{B}_r$, and $\alpha, \beta < 0$ describe the contraction measure, consistent with the analysis of cell bending. Since we assume the cell is polarized in the direction described by the angle φ, it is physically justified to assume that $|\alpha| > |\beta|$ since we expect most fibers to be oriented towards the polarized direction. The hypothesis that the fields C_1 and C_2 are linear functions in the thickness of the tube derives, as observed in Chapter 2, from the assumption that there is no deformation due to contractility at the basal surface. Therefore, the contractility deformation is described by:

$$\mathbb{F}_c = \mathbb{I} + \alpha(R - R_a)\mathbb{A} + \beta(R - R_a)\mathbb{A}^\perp. \tag{4.57}$$

Regarding the bending part, we observe that the fibers are compressed only along the maximum curvature direction, i.e., the circumferential direction $\mathbf{e}_\theta$. Hence, based on the

equation from Chapter 2, Section 1, we may assume the deformation gradient in the form:

$$\mathbb{F}_b = \begin{bmatrix} 1+B_1 & 0 & 0 \\ 0 & 1-k_1(R-\frac{R_b-R_a}{2}) & 0 \\ 0 & 0 & 1 \end{bmatrix} \tag{4.58}$$

where $k_1 = k_1(R) = -\frac{1}{R}$ is a scalar field that depends on the undeformed radius of the reference configuration $\mathscr{B}_r$. Notice that, as we did assume in Chapter 2, the curvature assumes only negative values. Indeed, as highlighted before, this assumption is necessary from a physics point of view, since the model proposed is not able to explain the behaviour for concave cylinder, as highlighted in the discussion of Section 2.3

The component in the radial direction depends on the other components by means of the limit of small thickness, as observed in Chapter 2. Indeed, observe that:

$$\mathbb{E}_b = \frac{1}{2}(\mathbb{C}_b - \mathbb{I}) \approx \begin{bmatrix} B_1 & 0 & 0 \\ 0 & -k_1(R-\frac{R_b-R_a}{2}) & 0 \\ 0 & 0 & 0 \end{bmatrix} \tag{4.59}$$

which coincides with Chapter 2 upon an orthogonal transformation of the axis. Notice that we neglected the terms of higher order in the thickness of the tube because of the small thickness hypothesis. Now we can compute the tensors $\mathbb{A}_r, \mathbb{A}_r^{\perp}, \mathbb{B}_r$ appearing inside equation (4.18), and then proceed with the bifurcation analysis. Keeping in mind that we neglect terms of higher order than linear in the thickness:

$$\begin{aligned} \mathbb{A}_r &= \mathbb{F}_b\mathbb{F}_c\mathbb{A}\mathbb{F}_c^T\mathbb{F}_b^T = \\ &= (1+2\alpha(R-R_a))\mathbb{F}_b\mathbb{A}\mathbb{F}_b \approx \\ &\approx (1+2\alpha(R-R_a))\mathbb{A} - 2k_1(R-\frac{R_b-R_a}{2}) \begin{bmatrix} 0 & 0 & 0 \\ 0 & \cos^2(\varphi) & \sin(2\varphi)/2 \\ 0 & \sin(2\varphi)/2 & 0 \end{bmatrix} \end{aligned} \tag{4.60}$$

and, with the same reasoning,

$$\mathbb{A}_r^{\perp} \approx (1+2\beta(R-R_a))\mathbb{A}^{\perp} - 2k_1(R-\frac{R_b-R_a}{2}) \begin{bmatrix} 0 & 0 & 0 \\ 0 & \sin^2(\varphi) & -\sin(2\varphi)/2 \\ 0 & -\sin(2\varphi)/2 & 0 \end{bmatrix}. \tag{4.61}$$

It remains to compute the tensor $\mathbb{B}_r$:

$$\begin{aligned} \mathbb{B}_r &= \mathbb{F}_b\mathbb{F}_c\mathbb{F}_c^T\mathbb{F}_b^T \approx \\ &\approx \mathbb{F}_b(\mathbb{I} + 2\alpha(R-R_a)\mathbb{A} + 2\beta(R-R_a)\mathbb{A}^{\perp})\mathbb{F}_b \\ &\approx \mathbb{F}_b\mathbb{F}_b^{\perp} + 2\alpha(R-R_a)\mathbb{A} + 2\beta(R-R_a)\mathbb{A}^{\perp}. \end{aligned} \tag{4.62}$$

Notice that the trace of the tensor $\mathbb{B}$ does not depend on the angle φ. Therefore, for $\mathbb{C}_e = \mathbb{I}$, there will not be any dependence on the reorientation angle given by the isotropic part.

The stationary configuration can be computed by setting the derivative of (4.18) with respect to the angle φ (which describes the direction of the fibers) to zero. This yields:

$$\begin{aligned}\frac{\partial W}{\partial \varphi}(\mathbb{C}_e) = \frac{\mu}{2}\frac{\partial \mathbb{B}_r}{\partial \varphi} : \mathbb{C}_e + \big[k_{44}(\mathbb{C}_e : \mathbb{A}_r - 1) + k_{46}(\mathbb{C}_e : \mathbb{A}_r^{\perp} - 1)\big]\mathbb{C}_e : \frac{\partial \mathbb{A}_r}{\partial \varphi} + \\ + \big[k_{66}(\mathbb{C}_e : \mathbb{A}_r^{\perp} - 1) + k_{46}(\mathbb{C}_e : \mathbb{A}_r - 1)\big]\mathbb{C}_e : \frac{\partial \mathbb{A}_r^{\perp}}{\partial \varphi} + \\ + k_{88}(\mathbf{N}_r^{\perp} \cdot (\mathbb{C}_e \mathbf{N}_r))\frac{\partial (\mathbf{N}_r^{\perp} \cdot (\mathbb{C}_e \mathbf{N}_r))}{\partial \varphi}\end{aligned} \tag{4.63}$$

The quantities involved can be computed directly using the forms of $\mathbb{A}_r$, $\mathbb{A}_r^{\perp}$, and $\mathbb{B}_r$ given in equations (4.60), (4.61), and (4.62) respectively. To keep the notation simple, let us define:

$$\tilde{\alpha} = \alpha(R - R_a), \quad \tilde{\beta} = \beta(R - R_a), \quad \tilde{k}_1 = k_1(R - \frac{R_b - R_a}{2}) \tag{4.64}$$

It is straightforward to show that:

$$\begin{aligned}\mathbb{C}_e : \frac{\partial \mathbb{A}_r}{\partial \varphi} &= [(1 + 2\tilde{\alpha})(\lambda_l^2 - \lambda^2) + 2\tilde{k}_1\lambda^2]\sin(2\varphi), \\ \mathbb{C}_e : \frac{\partial \mathbb{A}_r^{\perp}}{\partial \varphi} &= [(1 + 2\tilde{\beta})(\lambda^2 - \lambda_l^2) - 2\tilde{k}_1\lambda^2]\sin(2\varphi),\end{aligned} \tag{4.65}$$

and

$$\begin{aligned}\mathbb{C}_e : \mathbb{A}_r - 1 &= (1 + 2\tilde{\alpha})(\lambda^2\cos^2(\varphi) + \lambda_l^2\sin^2(\varphi)) - 2\tilde{k}_1\lambda^2\cos^2(\varphi) - 1 = \\ &= (1 + 2\tilde{\alpha})[(\lambda^2 - \lambda_l^2)\cos^2(\varphi) + \lambda_l^2] - 1 - 2\tilde{k}_1\lambda^2\cos^2(\varphi), \\ \mathbb{C}_e : \mathbb{A}_r^{\perp} - 1 &= (1 + 2\tilde{\beta})(\lambda^2\sin^2(\varphi) + \lambda_l^2\cos^2(\varphi)) - 2\tilde{k}_1\lambda^2\sin^2(\varphi) - 1 = \\ &= (1 + 2\tilde{\beta})[(\lambda_l^2 - \lambda^2)\cos^2(\varphi) + \lambda^2] - 1 - 2\tilde{k}_1\lambda^2\sin^2(\varphi).\end{aligned} \tag{4.66}$$

Finally, regarding the term proportional to k_{88}, we observe that:

$$\begin{aligned}\mathbf{N}_r^{\perp} \cdot (\mathbb{C}_e \mathbf{N}_r) &= \frac{\sin(2\varphi)}{2}[\lambda^2(1 + \tilde{\alpha} - \tilde{k}_1)(-(1 + \tilde{\beta} + \tilde{k}_1)) + \lambda_l^2(1 + \tilde{\alpha})(1 + \tilde{\beta})] \\ &= \frac{\sin(2\varphi)}{2}[(\lambda_l^2 - \lambda^2)(1 + \tilde{\alpha} + \tilde{\beta} + \tilde{\alpha}\tilde{\beta}) + \lambda^2\tilde{k}_1(2 + \tilde{\alpha} + \tilde{\beta} - \tilde{k}_1)].\end{aligned} \tag{4.67}$$

Hence,

$$k_{88}(\mathbf{N}_r^{\perp}\cdot(\mathbb{C}_e\mathbf{N}_r))\frac{\partial(\mathbf{N}_r^{\perp}\cdot(\mathbb{C}_e\mathbf{N}_r))}{\partial\varphi} = \frac{k_{88}}{2}\sin(2\varphi)\cos(2\varphi)\Big[(\lambda_l^2-\lambda^2)(1+\tilde{\alpha}+\tilde{\beta}+\tilde{\alpha}\tilde{\beta}) + \lambda^2\tilde{k}_1(2+\tilde{\alpha}+\tilde{\beta}-\tilde{k}_1)\Big]^2$$
$$\approx \frac{k_{88}}{2}\sin(2\varphi)(2\cos^2(\varphi)-1)\Big[(\lambda_l^2-\lambda^2)(1+\tilde{\alpha}+\tilde{\beta})^2 + 4\lambda^4\tilde{k}_1^2 + 2\lambda^2(\lambda_l^2-\lambda^2)\tilde{k}_1(2+3\tilde{\alpha}+3\tilde{\beta}-\tilde{k}_1)\Big], \tag{4.68}$$

where we neglected the terms of higher order than R^2. Notice that $\sin(2\varphi)$ can be factored from each component that appears inside the derivative of the elastic energy (4.63). Therefore, the configurations with angles $\varphi_0 = 0$ and $\varphi_1 = \frac{\pi}{2}$ are two trivial stationary points, consistent with theoretical results, as in Lucci and Preziosi [23]. Furthermore, the existence of a third oblique configuration generally depends on the material coefficients k_{ii} and, additionally due to the prestrain, on the coefficients $\tilde{\alpha}$, $\tilde{\beta}$, and particularly the curvature of the tube in the undeformed configuration $\tilde{k}_1$. Before analyzing the effects of these additional terms for a given $\mathbb{C}_e$ deformation in general, it is useful to examine the case $\mathbb{C}_e = \mathbb{I}$ to highlight the competition between curvature and active contractility effects.

4.3.1 Case $\mathbb{C}_e = \mathbb{I}$

Assuming that the tube is not deformed from the reference configuration $\mathscr{B}_r$, i.e., $\mathbb{C}_e = \mathbb{I}$, most of the components of equations (4.65)-(4.68) vanish. Therefore, the derivative of the strain energy function (4.63) can be written explicitly as:

$$\frac{\partial W}{\partial\varphi} = \sin 2\varphi\big[-\cos^2(\varphi)(k_{44}+k_{66}-2k_{46}-k_{88}) + 4\tilde{k}_1(\tilde{\alpha}(k_{44}-k_{46})+\tilde{\beta}(k_{46}-k_{66})) + 4\tilde{k}_1^2(k_{66}-k_{46}-\frac{k_{88}}{2})\big]. \tag{4.69}$$

Therefore, if an oblique stationary configuration φ^* exists, it satisfies:

$$\cos^2(\varphi^*) = \frac{\frac{\tilde{\alpha}}{\tilde{k}_1}(k_{44}-k_{46})+\frac{\tilde{\beta}}{\tilde{k}_1}(k_{46}-k_{66})+k_{66}-k_{46}-\frac{k_{88}}{2}}{k_{44}+k_{66}-2k_{46}-k_{88}} \tag{4.70}$$

Thus, similar to a cell bent over a cylinder, the oblique configuration φ^* here also depends on the ratios $\frac{\tilde{\alpha}}{\tilde{k}_1}$ and $\frac{\tilde{\beta}}{\tilde{k}_1}$, as well as the material coefficients. Plots of the oblique angle φ^* against the curvature k_1 are shown in Figures 4.2 and 4.3. Notice that the main feature observed in Chapter 2, Section 4, is maintained. Indeed, since φ is the angle between the direction $\mathbf{N}$ and the circumferential direction, Figure 4.2 shows that increasing

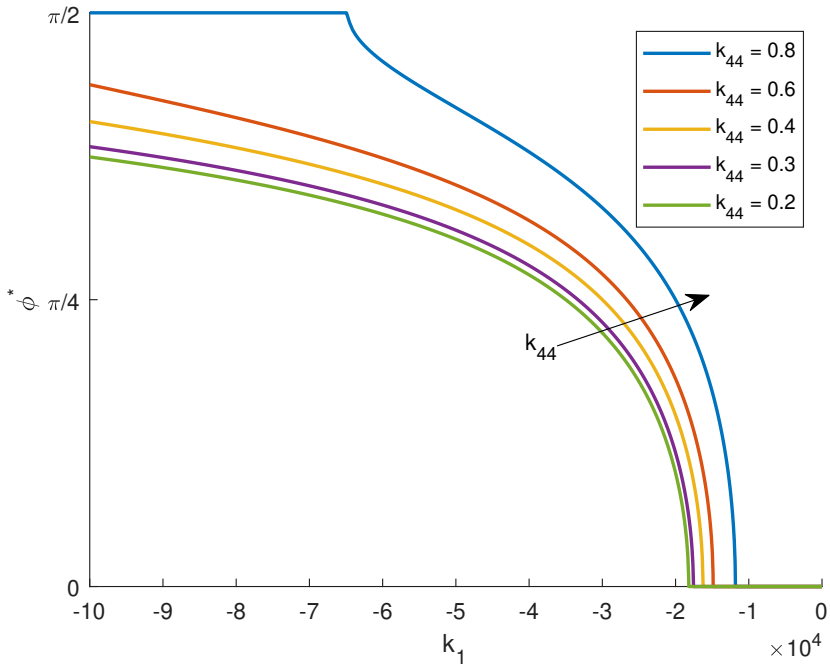

Figure 4.2. Oblique angle φ^* against the curvature k_1 for different k_{44}. The simulation parameter used are $k_{46} = k_{66} = 0.1$, $k_{88} = 0.0614$, $4\beta = \alpha = -2e4$

the stiffness of the fibers (i.e., k_{44}) results in an oblique angle φ^* that is more inclined towards the axial direction. On the other hand, increasing the strength of contractility shifts the stability range of the parallel configuration, thereby aligning the fibers towards the circumferential direction.

4.3.2 General Case

When the tube is inflated, the equilibrium expression will include all the terms present in equations (4.65) to (4.68). After some calculations, it can be shown that, if an oblique configuration exists, it takes the form:

$$\cos^2(\varphi^*) = \frac{k_{44} - k_{46} - \frac{k_{88}}{2} + A_2 - (k_{44} - k_{66} + B_2)\Lambda}{k_{44} + k_{66} - 2k_{46} - k_{88} + A_1} \tag{4.71}$$

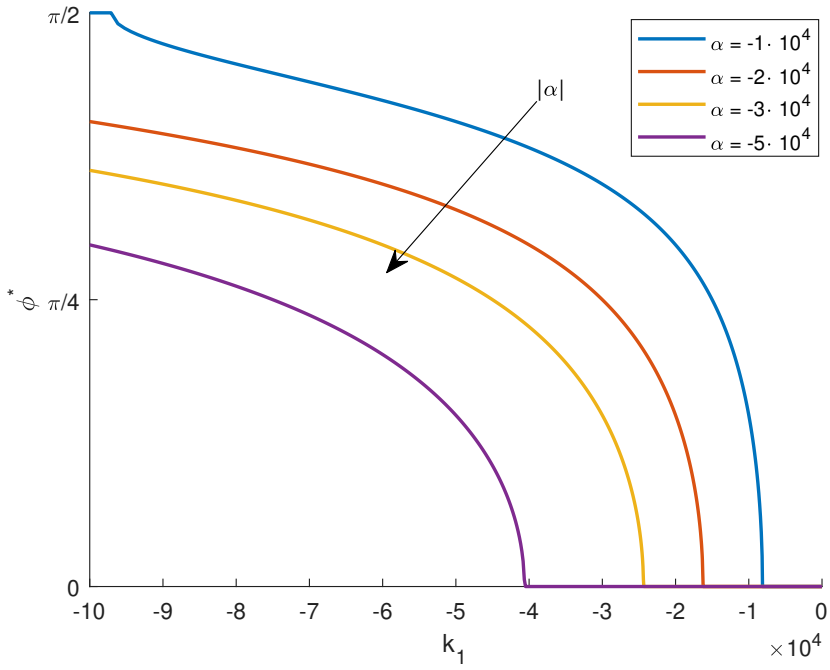

Figure 4.3. Oblique angle φ^* against the curvature k_1 for increasing contractility measure α. The simulation parameter used are $k_{44} = 0.4$, $k_{46} = k_{66} = 0.1$, $k_{88} = 0.0614$

where $\Lambda = \frac{\lambda_l^2 - 1}{\lambda_l^2 - \lambda^2}$, and A_1, A_2, and B_2 are scalar fields that depend on the deformation through λ^2 and λ_l^2. Specifically, they are given by:

$$\begin{aligned} A_1 &= 4\tilde{\alpha}(1 + \tilde{\alpha}k_{44}) + 4\tilde{\beta}(1 + \tilde{\beta}k_{66}) - 4(\tilde{\alpha} + \tilde{\beta} + \tilde{\alpha}\tilde{\beta}) \\ &\quad - k_{88}[(1 + \tilde{\alpha} + \tilde{\beta})^2 - 1] \\ &\quad - 2k_{46}\tilde{k}_1 \frac{\lambda^2}{\lambda^2 - \lambda_l^2} + 2k_{88}\tilde{k}_1 \frac{\lambda^2}{\lambda^2 - \lambda_l^2}(2 + 3\tilde{\alpha} + 3\tilde{\beta} - \tilde{k}_1) \\ &\quad + 4\tilde{k}_1^2 \left(\frac{\lambda}{\lambda^2 - \lambda_l^2} \right)^2 (k_{44} + k_{66} - 2k_{46} - k_{88}), \end{aligned} \tag{4.72}$$

$$
\begin{aligned}
A_2 =& 2(k_{46}-k_{66})\tilde{k}_1\frac{\lambda^2}{\lambda_l^2-\lambda^2}+2\tilde{\alpha}k_{44}-2\tilde{\beta}k_{46}\\
&-\frac{\alpha}{\lambda_l^2-\lambda^2}\left[2\tilde{k}_1\frac{\lambda^2}{\lambda_l^2-\lambda^2}(k_{44}-k_{46})+(1+2\tilde{\alpha})k_{44}-(1+2\tilde{\beta})k_{46}\right]\\
&+2\left(1-\frac{1}{\lambda_l^2-\lambda^2}\right)(2\tilde{\beta}-2\tilde{k}_1)\left[\tilde{k}_1\frac{\lambda^2}{\lambda_l^2-\lambda^2}+(1+2\tilde{\alpha})k_{46}-(1+2\tilde{\beta})k_{66}\right]\\
&-\frac{k_{88}}{2}\left[[(1+\tilde{\alpha}+\tilde{\beta})^2-1]+2\tilde{k}_1\frac{\lambda^2}{\lambda^2-\lambda_l^2}(2+3\tilde{\alpha}+3\tilde{\beta}-\tilde{k}_1)-4\tilde{k}_1^2(\frac{\lambda^2}{\lambda^2-\lambda_l^2})^2\right],
\end{aligned}
\tag{4.73}
$$

$$
\begin{aligned}
B_2 =& 2\tilde{k}_1\frac{\lambda^2}{\lambda_l^2-\lambda^2}(k_{44}-k_{66})+2\tilde{\alpha}(k_{44}+k_{46})-2\tilde{\beta}(k_{66}+k_{46})\\
&+2\tilde{\alpha}\left[2\tilde{k}_1\frac{\lambda^2}{\lambda_l^2-\lambda^2}(k_{44}-k_{46})+(1+2\tilde{\alpha})k_{44}-(1+2\tilde{\beta})k_{46}\right]\\
&+2(\tilde{\beta}-\tilde{k}_1)\left[2\tilde{k}_1\frac{\lambda^2}{\lambda_l^2-\lambda^2}(k_{46}-k_{66})+(1+2\tilde{\beta})k_{46}-(1+2\tilde{\alpha})k_{66}\right].
\end{aligned}
\tag{4.74}
$$

Each term inside A_1, A_2, and B_2 depends only on the coefficients $\tilde{\alpha}$, $\tilde{\beta}$, and $\tilde{k}_1$, all of which are proportional to the tube's thickness h. Therefore, these terms become significant only if the curvature k_1 and/or the contractility measures α and β are strong enough to overcome the small value of the thickness. Thus, if α and β are small enough, as expected at the cellular level, these additional terms become relevant only for sufficiently large curvatures k_1, corresponding to a very small undeformed radius R.

If this is not the case, we should observe the usual linear relationship between $\cos^2(\varphi^*)$ and the deformation measure Λ defined above. This is indeed observed in Figure 4.4, where it can be seen that higher curvature shifts the angle towards the orthogonal configuration $\varphi_1 = \frac{\pi}{2}$, i.e., towards the axial direction. The material parameters used in the simulation are $k_{44} = 0.4$, $k_{46} = k_{66} = 0.1$, $k_{88} = 0.0614$, while the contractility measures are chosen as $4\beta = \alpha = -10^2$. The thickness is chosen as $h = 0.1\,\text{mm}$, in accord with the simulation in Chapter 3. The contractility measure in the orthogonal direction, β, is chosen lower than α to account for the polarity of the cell, as we expect a large number of fibers in the principal direction, hence a large contraction. The material parameters are in accord with those adopted by Lucci and Preziosi [23], based on the experimental studies of Faust et al. [24] and Livne et al. [54]. The parameter Λ changes with the axial stretch λ_l. Notice that, in the large curvature limit ($k_1 = -10^4$, blue line), the oblique angle φ^* tends to always align towards the axial direction, as indicated by the low values of $\cos^2(\varphi)$. Additionally, the parameter Λ, which describes the inflation, does not significantly alter this behavior due to the high curvature. In contrast, a more significant dependence may be observed for lower curvature magnitudes, as the deformation effects become stronger.

A similar behavior is observed for a fixed $\lambda_l^2 = 1.2$ and varying λ^2, as shown in Figure 4.5. As before, the main stretching direction is the axial one, but this time the parameter

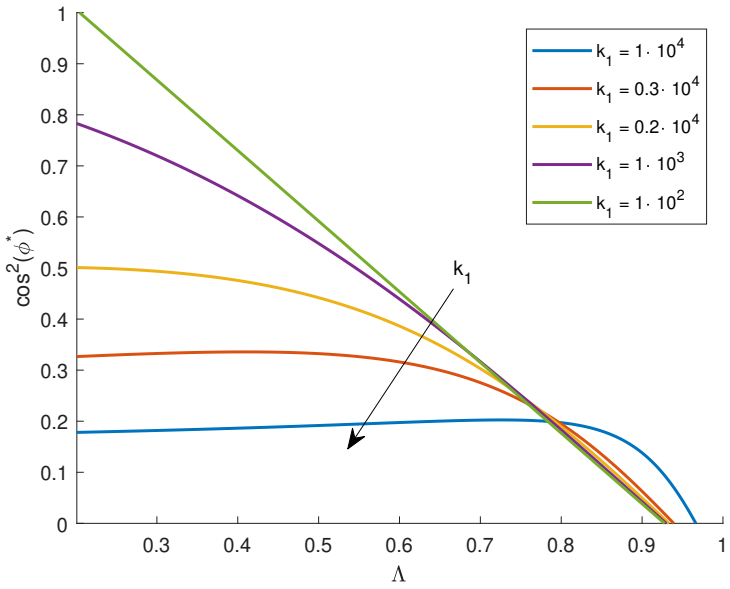

Figure 4.4. Plot of $\cos^2(\varphi)$ against Λ. The simulation is made by choosing $k_{44} = 0.4$, $k_{46} = k_{66} = 0.1$, $k_{88} = 0.0614$, and $4\beta = \alpha = -10^2$. The circumferential stretch is fixed $\lambda = 0.8$, while the axial one $\lambda_l > 1$.

Λ changes as λ varies, contrary to the previous case. Indeed, the results for sufficiently large curvature (green line) correspond to those observed for the inflation of a cylinder in Chapter 3, Section 4. However, the introduction of prestrain allows us to capture the competition between bending and contractility observed at the cellular scale for sufficiently large curvatures (as shown by the blue line). This behavior was not described by the simpler model in Chapter 3, since, as already highlighted in that chapter, the undeformed radius scale did not affect the final results, whereas this model succeeds in doing so.

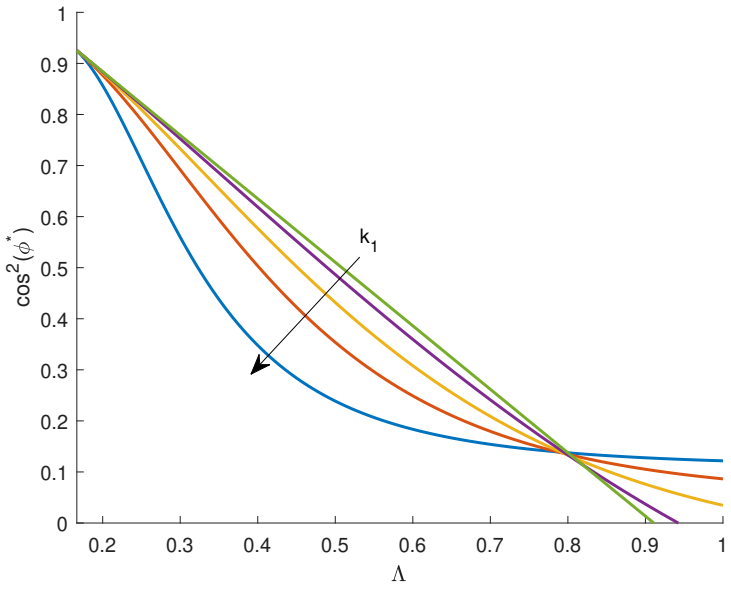

Figure 4.5. Plot of $\cos^2(\varphi)$ against Λ. The simulation is made by choosing $k_{44} = 0.4$, $k_{46} = k_{66} = 0.1$, $k_{88} = 0.0614$, and $4\beta = \alpha = -10^2$. The axial stretch is fixed $\lambda_l = 1.2$, while the axial one $\lambda < 1$.

Chapter 5

Conclusions

This thesis has delved into the responses of cells to mechanical and geometrical cues, with a particular emphasis on the influence of substrate curvature on cellular behavior. Building on the foundational work of Biton and Safran, this study has extended their theoretical model by integrating recent empirical findings to offer a more comprehensive understanding of the phenomenon.

The investigation into the mechanical response of cells on curved substrates has revealed that cells exhibit distinct reorientation behaviors compared to those on flat surfaces. Specifically, cells align their stress fibers (SFs) in response to the substrate curvature, with varying patterns observed among different cell types. For instance, at high curvatures, muscle cells tend to align with the direction of lesser curvature, while epithelial cells align with the direction of maximal curvature. This recent experimental finding underscores the significant impact of substrate geometry on cellular orientation.

A key component of this research involved the development of a structured mathematical model to elucidate the reorientation process using a Continuum Mechanics framework. Based on the experimental findings, the hypothesis that garnered more success states that there is a trade-off between the active contractility of the cell and bending due to substrate curvature, as assumed by Biton and Safran [15]. The stability analysis, conducted through bifurcation theory, identified critical configurations wherein cells undergo notable morphological changes. These changes are driven by the energy landscape shaped by the competing forces of bending and contractility, providing a deeper insight into the cellular behavior on curved substrates. The results achieved generalize those obtained by Biton and Safran, demonstrating that for a particular choice of parameters, their model's predictions are realized.

The study further explored the reorientation of cells on inflated cylindrical substrates, inspired by the biological example of blood vessels. The kinematics of cylinder inflation and its effect on cellular orientation demonstrated that the deformed radius plays a crucial role in influencing cell behavior. While the model accurately predicted a limited set of experimental results, it highlighted the necessity of considering cellular-level interactions for a more precise understanding of the observed phenomena. Therefore, the impact of residual stress on cellular orientation was examined by extending the analysis to materials with initial stress, employing hyperelastic theory to describe residual stresses in

orthotropic materials. The findings indicated that residual stress significantly affects cellular reorientation for sufficiently small radii while returning to the classical limit for larger radii, offering valuable insights into the mechanical environment that cells encounter.

The implications of these findings for biomedical applications are profound, particularly in the realms of tissue engineering and biomaterial design. A thorough understanding of how cells respond to mechanical and geometrical cues is essential for developing innovative materials. In tissue engineering, the design of scaffolds with appropriate curvature can guide cell growth and organization, thereby enhancing tissue regeneration and repair.

Looking ahead, this research opens several promising avenues for future investigation. One critical area is the development of a model that qualitatively explains the experimental findings for positive curvature values, such as those occurring on the internal surface of a blood vessel. As pointed out earlier, our model does not address positive curvature from a physical perspective. Hence, it may be necessary to consider other factors, such as the buckling of the stress fibers, which may reduce contractility strength, or include specific interactions between the SFs and the substrate shape. Moreover, from a mathematical point of view, the linear model of cell bending proposed here is based on a set of assumptions that do not hold in all contexts; therefore, the development of a non-linear theory should be pursued, for example, by adopting the Föppl-von Kármán plate equations or higher-order theories. Finally, the pre-stress framework allows us to account for additional factors that may influence cell reorientation, such as growth. Further investigation should explore the results of such pre-strain at the cellular level, and a comparison with well-established methods, such as the opening-angle method, may reveal interesting features.

Additionally, experimental validation of the theoretical models developed in this thesis is essential. Conducting more extensive experimental studies, particularly focusing on different cell types and substrate curvatures, will be crucial for confirming the accuracy of these models. Expanding the models to include detailed cellular-level interactions will provide a more comprehensive understanding of how individual cells contribute to the overall behavior observed on curved substrates.

In conclusion, this thesis has made contributions to our understanding of cellular responses to mechanical and geometrical cues. Through a combination of experimental observations and mathematical modeling, it has provided a detailed analysis of the mechanical principles governing cell behavior on curved substrates.

Bibliography

[1] R. W. Ogden, "Nonlinear elasticity, anisotropy, material stability and residual stresses in soft tissue," in *Biomechanics of soft tissue in cardiovascular systems*, pp. 65–108, Springer, 2003.

[2] G. A. Holzapfel and T. C. Gasser, "A viscoelastic model for fiber-reinforced composites at finite strains: Continuum basis, computational aspects and applications," *Computer methods in applied mechanics and engineering*, vol. 190, no. 34, pp. 4379–4403, 2001.

[3] R. C. Buck, "The longitudinal orientation of structures in the subendothelial space of rat aorta," *American Journal of Anatomy*, vol. 156, no. 1, pp. 1–13, 1979.

[4] R. C. Buck, "Reorientation response of cells to repeated stretch and recoil of the substratum," *Experimental cell research*, vol. 127, no. 2, pp. 470–474, 1980.

[5] K. Hayakawa, A. Hosokawa, K. Yabusaki, and T. Obinata, "Orientation of smooth muscle-derived a10 cells in culture by cyclic stretching: relationship between stress fiber rearrangement and cell reorientation," *Zoological science*, vol. 17, no. 5, pp. 617–624, 2000.

[6] M. Moretti, A. Prina-Mello, A. Reid, V. Barron, and P. Prendergast, "Endothelial cell alignment on cyclically-stretched silicone surfaces," *Journal of Materials Science: Materials in Medicine*, vol. 15, pp. 1159–1164, 2004.

[7] J. H.-C. Wang, P. Goldschmidt-Clermont, J. Wille, and F. C.-P. Yin, "Specificity of endothelial cell reorientation in response to cyclic mechanical stretching," *Journal of biomechanics*, vol. 34, no. 12, pp. 1563–1572, 2001.

[8] T. Matsumoto, P. Delafontaine, K. J. Schnetzer, B. C. Tong, and R. M. Nerem, "Effect of uniaxial, cyclic stretch on the morphology of monocytes/macrophages in culture," 1996.

[9] C. Giverso, N. Loy, G. Lucci, and L. Preziosi, "Cell orientation under stretch: A review of experimental findings and mathematical modelling," *Journal of Theoretical Biology*, p. 111564, 2023.

[10] G. E. White, M. A. Gimbrone Jr, and K. Fujiwara, "Factors influencing the expression of stress fibers in vascular endothelial cells in situ.," *The Journal of cell biology*, vol. 97, no. 2, pp. 416–424, 1983.

[11] A. J. Wong, T. D. Pollard, and I. M. Herman, "Actin filament stress fibers in vascular endothelial cells in vivo," *Science*, vol. 219, no. 4586, pp. 867–869, 1983.

[12] H. G. Yevick, G. Duclos, I. Bonnet, and P. Silberzan, "Architecture and migration of an epithelium on a cylindrical wire," *Proceedings of the National Academy of Sciences*, vol. 112, no. 19, pp. 5944–5949, 2015.

[13] S.-M. Yu, J. M. Oh, J. Lee, W. Lee-Kwon, W. Jung, F. Amblard, S. Granick, and Y.-K. Cho, "Substrate curvature affects the shape, orientation, and polarization of renal epithelial cells," *Acta biomaterialia*, vol. 77, pp. 311–321, 2018.

[14] P. Rougerie, L. Pieuchot, R. S. Dos Santos, J. Marteau, M. Bigerelle, P.-F. Chauvy, M. Farina, and K. Anselme, "Topographical curvature is sufficient to control epithelium elongation," *Scientific reports*, vol. 10, no. 1, p. 14784, 2020.

[15] Y. Biton and S. Safran, "The cellular response to curvature-induced stress," *Physical biology*, vol. 6, no. 4, p. 046010, 2009.

[16] N. D. Bade, R. D. Kamien, R. K. Assoian, and K. J. Stebe, "Curvature and rho activation differentially control the alignment of cells and stress fibers," *Science advances*, vol. 3, no. 9, p. e1700150, 2017.

[17] T. Mao, Y. He, Y. Gu, Y. Yang, Y. Yu, X. Wang, and J. Ding, "Critical frequency and critical stretching rate for reorientation of cells on a cyclically stretched polymer in a microfluidic chip," *ACS Applied Materials & Interfaces*, vol. 13, no. 12, pp. 13934–13948, 2021.

[18] C. Tamiello, A. B. Buskermolen, F. P. Baaijens, J. L. Broers, and C. V. Bouten, "Heading in the right direction: understanding cellular orientation responses to complex biophysical environments," *Cellular and molecular bioengineering*, vol. 9, pp. 12–37, 2016.

[19] K. Hayakawa, N. Sato, and T. Obinata, "Dynamic reorientation of cultured cells and stress fibers under mechanical stress from periodic stretching," *Experimental cell research*, vol. 268, no. 1, pp. 104–114, 2001.

[20] A. Roshanzadeh, T. T. Nguyen, K. D. Nguyen, D.-S. Kim, B.-K. Lee, D.-W. Lee, and E.-S. Kim, "Mechanoadaptive organization of stress fiber subtypes in epithelial cells under cyclic stretches and stretch release," *Scientific reports*, vol. 10, no. 1, p. 18684, 2020.

[21] J. W. Mason, D. J. Ramseth, D. O. Chanter, T. E. Moon, D. B. Goodman, and B. Mendzelevski, "Electrocardiographic reference ranges derived from 79,743 ambulatory subjects," *Journal of electrocardiology*, vol. 40, no. 3, pp. 228–234, 2007.

[22] S. Jungbauer, H. Gao, J. P. Spatz, and R. Kemkemer, "Two characteristic regimes in frequency-dependent dynamic reorientation of fibroblasts on cyclically stretched substrates," *Biophysical journal*, vol. 95, no. 7, pp. 3470–3478, 2008.

[23] G. Lucci, C. Giverso, and L. Preziosi, "Cell orientation under stretch: Stability of a linear viscoelastic model," *Mathematical Biosciences*, vol. 337, p. 108630, 2021.

[24] U. Faust, N. Hampe, W. Rubner, N. Kirchgessner, S. Safran, B. Hoffmann, and R. Merkel, "Cyclic stress at mhz frequencies aligns fibroblasts in direction of zero strain," *PloS one*, vol. 6, no. 12, p. e28963, 2011.

[25] A. Tondon, H.-J. Hsu, and R. Kaunas, "Dependence of cyclic stretch-induced stress fiber reorientation on stretch waveform," *Journal of biomechanics*, vol. 45, no. 5, pp. 728–735, 2012.

[26] B. Schamberger, R. Ziege, K. Anselme, M. Ben Amar, M. Bykowski, A. P. Castro, A. Cipitria, R. A. Coles, R. Dimova, M. Eder, *et al.*, "Curvature in biological systems: its quantification, emergence, and implications across the scales," *advanced materials*, vol. 35, no. 13, p. 2206110, 2023.

[27] S. J. Callens, R. J. Uyttendaele, L. E. Fratila-Apachitei, and A. A. Zadpoor, "Substrate curvature as a cue to guide spatiotemporal cell and tissue organization," *Biomaterials*, vol. 232, p. 119739, 2020.

[28] Y. Jin, L. Liu, P. Yu, F. Lin, X. Shi, J. Guo, B. Che, Y. Duan, J. Li, Y. Pan, *et al.*, "Emergent differential organization of airway smooth muscle cells on concave and convex tubular surface," *Frontiers in Molecular Biosciences*, vol. 8, p. 717771, 2021.

[29] N. D. Bade, T. Xu, R. D. Kamien, R. K. Assoian, and K. J. Stebe, "Gaussian curvature directs stress fiber orientation and cell migration," *Biophysical journal*, vol. 114, no. 6, pp. 1467–1476, 2018.

[30] M. Werner, N. A. Kurniawan, G. Korus, C. V. Bouten, and A. Petersen, "Mesoscale substrate curvature overrules nanoscale contact guidance to direct bone marrow stromal cell migration," *Journal of The Royal Society Interface*, vol. 15, no. 145, p. 20180162, 2018.

[31] J. A. Sanz-Herrera, P. Moreo, J. M. García-Aznar, and M. Doblaré, "On the effect of substrate curvature on cell mechanics," *Biomaterials*, vol. 30, no. 34, pp. 6674–6686, 2009.

[32] H. Le Dret and A. Raoult, "The nonlinear membrane model as variational limit of nonlinear three-dimensional elasticity," *Journal de mathématiques pures et appliquées*, vol. 74, no. 6, pp. 549–578, 1995.

[33] L. D. Landau, L. Pitaevskii, A. M. Kosevich, and E. M. Lifshitz, *Theory of elasticity: volume 7*, vol. 7. Elsevier, 2012.

[34] E. H. Mansfield, *The Bending and Stretching of Plates: International Series of Monographs on Aeronautics and Astronautics: Solid and Structural Mechanics, Vol. 6*, vol. 6. Elsevier, 2014.

[35] B. Audoly and Y. Pomeau, "Elasticity and geometry," in *Peyresq Lectures on Nonlinear Phenomena*, pp. 1–35, World Scientific, 2000.

[36] T. E. Kreis and W. Birchmeier, "Stress fiber sarcomeres of fibroblasts are contractile," *Cell*, vol. 22, no. 2, pp. 555–561, 1980.

[37] S. Tojkander, G. Gateva, and P. Lappalainen, "Actin stress fibers–assembly, dynamics and biological roles," *Journal of cell science*, vol. 125, no. 8, pp. 1855–1864, 2012.

[38] K. Burridge and M. Chrzanowska-Wodnicka, "Focal adhesions, contractility, and signaling," *Annual review of cell and developmental biology*, vol. 12, no. 1, pp. 463–519, 1996.

[39] I. L. Novak, B. M. Slepchenko, A. Mogilner, and L. M. Loew, "Cooperativity between cell contractility and adhesion," *Physical review letters*, vol. 93, no. 26, p. 268109, 2004.

[40] G. Sommer, "Mechanical properties of healthy and diseased human arteries," *TU Graz*, 2008.

[41] G. Sommer, P. Regitnig, L. Költringer, and G. A. Holzapfel, "Biaxial mechanical properties of intact and layer-dissected human carotid arteries at physiological and supraphysiological loadings," *Am J Physiol Heart Circ Physiol*, vol. 298, pp. H898–H912, 2010.

[42] J. Merodio and R. Ogden, "The influence of the invariant i8 on the stress–deformation and ellipticity characteristics of doubly fiber-reinforced non-linearly elastic solids," *International Journal of Non-Linear Mechanics*, vol. 41, no. 4, pp. 556–563, 2006.

[43] A. Hoger, "On the residual stress possible in an elastic body with material symmetry," *Archive for Rational Mechanics and Analysis*, vol. 88, pp. 271–289, 1985.

[44] A. Hoger, "The constitutive equation for finite deformations of a transversely isotropic hyperelastic material with residual stress," *Journal of elasticity*, vol. 33, no. 2, pp. 107–118, 1993.

[45] B. E. Johnson and A. Hoger, "The dependence of the elasticity tensor on residual stress," *Journal of Elasticity*, vol. 33, pp. 145–165, 1993.

[46] A. L. Gower, P. Ciarletta, and M. Destrade, "Initial stress symmetry and applications in elasticity," *arXiv preprint arXiv:1506.05038*, 2015.

[47] A. L. Gower, T. Shearer, and P. Ciarletta, "A new restriction for initially stressed elastic solids," *The Quarterly Journal of Mechanics and Applied Mathematics*, vol. 70, no. 4, pp. 455–478, 2017.

[48] S. Mukherjee, M. Destrade, and A. L. Gower, "Representing the stress and strain energy of elastic solids with initial stress and transverse texture anisotropy," *Proceedings of the Royal Society A*, vol. 478, no. 2266, p. 20220255, 2022.

[49] R. W. Ogden, "Change of reference configuration in nonlinear elasticity: Perpetuation of a basic error," *Mathematics and Mechanics of Solids*, vol. 28, no. 9, pp. 2132–2138, 2023.

[50] M. Shams, M. Destrade, and R. W. Ogden, "Initial stresses in elastic solids: constitutive laws and acoustoelasticity," *Wave Motion*, vol. 48, no. 7, pp. 552–567, 2011.

[51] V. Lubarda, "Constitutive theories based on the multiplicative decomposition of deformation gradient: Thermoelasticity, elastoplasticity, and biomechanics," *Applied Mechanics Reviews*, vol. 57, 03 2004.

[52] A. L. Gower, T. Shearer, P. Ciarletta, and M. Destrade, "The elastic stored energy of initially strained, or stressed, materials: restrictions and third-order expansions," *arXiv preprint arXiv:2403.09280*, 2024.

[53] P. Ciarletta, M. Destrade, A. L. Gower, and M. Taffetani, "Morphology of residually stressed tubular tissues: Beyond the elastic multiplicative decomposition," *Journal of the Mechanics and Physics of Solids*, vol. 90, pp. 242–253, 2016.

[54] A. Livne, E. Bouchbinder, and B. Geiger, "Cell reorientation under cyclic stretching," *Biophysical journal*, vol. 106, no. 2, p. 42a, 2014.

List of Figures

Acknowledgements

Desidero esprimere la mia profonda gratitudine ai miei relatori, il Prof. Luigi Preziosi, la Prof.ssa Chiara Giverso e il Dott. Giulio Lucci, per il loro costante supporto, guida e incoraggiamento durante lo sviluppo di questa Tesi. Le loro preziose indicazioni e la loro esperienza sono stati fondamentali per la realizzazione di questo lavoro. Grazie di cuore per il vostro tempo e dedizione.